DEPARTMENT OF PHYSICS
UNIVERSITY OF JYVÄSKYLÄ
RESEARCH REPORT No. 9/2003

TRANSPORT PHENOMENA AND DECOHERENCE IN SHORT JOSEPHSON JUNCTION ARRAYS

BY
JUSSI TOPPARI

Academic Dissertation
for the Degree of
Doctor of Philosophy

To be presented, by permission of the
Faculty of Mathematics and Science
of the University of Jyväskylä,
for public examination in Auditorium FYS-1 of the
University of Jyväskylä on December 3, 2003
at 14 o'clock

Jyväskylä, Finland
December 2003

ISBN 978-951-39-3147-6
URN:ISBN:978-951-39-3147-6

Preface

The work reviewed in this thesis has been carried out during the years 1998-2003 at the Department of Physics in the University of Jyväskylä. The major share of it has been done as a part of the European Union SQUBIT (Superconducting Qubits: Quantum Computing with Josephson Junctions; IST-10673) project.

First of all, I wish to thank my supervisor Academy Prof. Jukka Pekola for his valuable and persistent guidance during these years, and for introducing me to the fascinating world of nanostructures. I'm still amazed how the rules of quantum mechanics can be realised in practise using these tiny man-made devices. I'm also grateful to Dr. Antti Manninen for his excellent assistance in many practical issues at the beginning of my work and to Dr. Klavs Hansen for widening my viewpoint on many physical phenomena. Special mention is also deserved by Dr. Matias Aunola for fruitful collaboration and advices in many theoretical issues, and by Mr. Jani Kivioja for irreplaceable help in the measurements of the Cooper pair pump, as well as the whole PICO and NANO groups at the Low Temperature Laboratory of Helsinki University of Technology, where the experiments on the Cooper pair pump in article A.VI were performed. And of course big compliments to all former and present members of the SQUBIT group: Mr. Marko Savolainen, Mr. Lasse Taskinen, Dr. Sorin Paraoanu, and Mr. Ari Halvari for co-operation, and all the members of the SOFY group for very inspiring and pleasant atmosphere.

Financial support from the National Graduate School in Materials Physics, Academy of Finland, EU, and Finnish Academy of Science and Letters (Väisälän rahasto) are gratefully acknowledged.

Finally, I wish to thank my parents for support and encouraging me to study physics. And most of all I want to thank my wife Kristiina and son Aleks for their love and support.

Jyväskylä, September 2003

Jussi Toppari

Abstract

Toppari, Jussi
Transport phenomena and decoherence in short Josephson junction arrays
Jyväskylä: University of Jyväskylä, 2003, 96 p.
(Research report/Department of Physics, University of Jyväskylä,
ISSN 0075-465X; 9/2003)
ISBN 951-39-1631-6
diss.

In this thesis transport phenomena in the arrays consisting of two (SSET) or three (CPP) or more Josephson junctions are discussed. A quantitative theory of adiabatic Cooper pair transport in phase biased arrays is developed. The theory predicts that the quantum inaccuracy of the Cooper pair pumping in arrays with a small number of junctions is very large. The effects due to inhomogeneous arrays or nonideal gating sequences are also quantitatively treated. It is also shown explicitly how the pumped charge in the Cooper pair pump can be understood as a partial derivative of Berry's phase with respect to the phase difference φ across the array. This makes possible to obtain information about Berry's phase by measuring the pumped current in the CPP.

Also the decoherence time τ_φ, which is one of the central quantities in quantum computing, is quantitatively estimated in a dissipative electromagnetic environment of the circuit. This method allows comparison of the suitability of a system as a quantum bit. Also a direct measurement of τ_φ as a crossover between coherent and incoherent pumping in the single Cooper pair pump is suggested.

In experiments with Cooper pair pump it is demonstrated in practise how the CPP can be used as a turnstile with help of dissipation. Also a regular pumping experiment is performed. To explain the twofold behavior of the CPP, sometimes yielding e-periodicity while sometimes $2e$-periodicity, the energy-minimisation model is developed. It is shown also experimentally that Nb based junctions with high critical temperature ($T_\mathrm{c} \approx 8.5$ K) and Josephson coupling can be fabricated using the regular self-alignment technique. The measured Al/Nb/Al SSETs show a clear signature of resonant tunnelling of Cooper pairs combined with elastic cotunnelling of quasiparticles, q-MQT, through the barrier of Δ_Nb.

Keywords Tunnelling, Josephson effect, Cooper pair pump, decoherence, superconductivity, quantum computing

Author's address Jussi Toppari
Department of Physics
University of Jyväskylä
Finland

Supervisor Professor Jukka Pekola
Department of Physics
University of Jyväskylä
Finland

Present address:
Low Temperature Laboratory
Helsinki University of Technology
Finland

Reviewers Professor Frank Hekking
Universite Joseph Fourier
Laboratoire de Physique et Modélisation des Milieux Condensés
CNRS Grenoble
France

Professor Kalle-Antti Suominen
Department of Physics
University of Turku
Finland

Opponent Professor David Haviland
Nanostructure Physics
KTH Albanova
Stockholm
Sweden

List of Publications

The main results of this thesis have been reported in the following articles:

A.I FARHANGFAR, SH., TOPPARI, J.J., PASHKIN, YU.A., MANNINEN, A.J., AND PEKOLA, J.P., *Experiments on tunnelling in small normal-metal junctions influenced by dissipative environment: Critical comparison to the theories of quantum fluctuations*. Europhys. Lett.**43** (1) (1998) 59–64.

A.II PEKOLA, J.P., TOPPARI, J.J., AUNOLA, M., SAVOLAINEN, M.T., AND AVERIN, D.V., *Adiabatic transport of Cooper pairs in arrays of Josephson junctions*. Phys. Rev. B **60** (1999) R9931.

A.III AUNOLA, M., TOPPARI, J.J., AND PEKOLA, J.P., *Arrays of Josephson junctions in an environment with vanishing impedance*. Phys. Rev. B **62** (2000) 1296.

A.IV PEKOLA, J.P., AND TOPPARI, J.J., *Decoherence in circuits of small Josephson junctions*. *Phys. Rev. B **64** (2001) 172509*.

A.V AUNOLA, M., AND TOPPARI, J.J., *Connecting Berry's phase and the pumped charge in a Cooper pair pump*. Phys. Rev. B **68** (2003) 020502(R).

A.VI TOPPARI, J.J., KIVIOJA, J.M., PEKOLA, J.P., AND SAVOLAINEN, M.T., *Turnstile behaviour of the Cooper-pair pump*. cond-mat/0311135, submitted for publication.

A.VII TOPPARI, J.J., PARAOANU, G.S., HALVARI, A.M., AND PEKOLA, J.P., *Low-bias transport phenomena in Al/Nb/Al SETs: Combined resonant tunnelling of Cooper pairs and q-MQT*. cond-mat/0311148, submitted for publication.

Author's contribution

The author of this thesis has written the papers A.VI (except for chapter IV.A in it) and A.VII, partly the papers A.IV and A.V, and participated in writing of A.I, A.II and A.III. In A.I the author carried out part of the sample fabrication, measurements,

analysing of the data and main part of the numerical calculations, and contributed significantly to the theoretical derivations using the phase-correlation theory. The author took part in the development of the main theoretical result in A.II and made all the numerical calculations in it. In A.III author's responsibility was part of the numerical analysis. The author did part of the theoretical analysis in A.IV and contributed to almost all the derivations. In A.V the author determined how to get a measure of Berry's phase in a real experiment of Cooper pair pump and derived the result for coherence amplitudes. All the measurements in papers A.VI and A.VII were done by the author of this thesis together with the second author in these papers. The author also was responsible of all the analysis of the measured data in A.VI and the main part of the analysis in A.VII, and derived the theoretical models in A.VI. In addition, the author has produced almost all the graphics in every article, except in A.III.

Contents

1 Introduction

1.1 Significance of size

During the past couple of decades the steady progress in microelectronics and the tendency to build smaller and smaller devices have pushed industry to the point where the limit of classical technologies lies no more in the remote future. Some modern commercial apparatuses are already now operating in the conditions where classical behaviour is perturbed due to the effects arising from the small size. These effects are getting more pronounced when the size is going to be further reduced and structures are entering the regime where one has to take into account the effects of quantum mechanics. In the extreme limit there exists the smallest structures of the nature; particles like quarks, electrons, atoms built of them etc., which have been proven to strictly obey the laws of quantum mechanics. This leaves an interesting gap between the classical behaviour of the macroscopic objects and the quantum behaviour of the microscopic ones.

Modern fabrication methods have made it possible to build *mesoscopic* electronic devices laying in this intermediate regime, concretely showing the effects of quantum mechanics and still being much larger than the usual microscopic objects and thus partly operating as classical systems. The operation of these devices is often based on the quantum mechanical tunnelling phenomenon and especially on the possibility of an electron to tunnel through a very thin insulation layer. This situation can be arranged in practise by two metallic electrodes with an artificial thin insulation layer separating them. This kind of setup is called a *tunnel junction* and it can be characterised by the capacitance C due to its classical properties and construction, and the tunnelling resistance $R_{\mathrm{T}} = R_{\mathrm{K}}/(4\pi N\mathcal{T})$ originating from the current due to electron tunnelling. Here $\mathcal{T}$ is the barrier transmission coefficient, N is the number of independent electron channels through the barrier and $R_{\mathrm{K}} = h/e^2 \simeq 25.8\ \mathrm{k}\Omega$ is the resistance quantum. [17]

In standard electronics a single electron does not play any major role due to a huge number of them involved in current flow and the ability of them to continuously move in the ionic background [40]. The possibility to see the effects produced by single electrons arises from the small size and thus the small capacitance C of the tunnel junction, which considerably increases the electrostatic energy $E_{\mathrm{C}} = e^2/2C$ needed to charge the junction with one electron. By combining this fact

with the modern cooling methods, e.g., dilution refrigeration, capable of producing subkelvin temperatures T, it is possible in practise to reach the necessary limit

$$E_{\mathrm{C}} \gg k_{\mathrm{B}}T, \tag{1.1}$$

where the charging effects of invidual electrons are not anymore smeared by the thermal fluctuations.

1.2 Basic normal-metal single electron devices

1.2.1 Single electron box

To observe the charging effects of single electrons to its full extent it is not enough to satisfy the relation Eq. (1.1). In addition, it is necessary to have a metallic island galvanically separated from other metallic regions so that the charge on the island can change only by electron tunnelling via tunnel junction or junctions. Also the tunnelling resistance of the junction has to be larger than the resistance quantum, $R_{\mathrm{T}} \gg R_{\mathrm{K}}$, to have the wave function of an electron to be localised on the island.

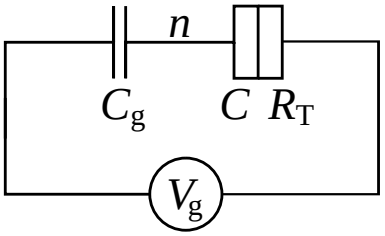

FIGURE 1.1 Single electron box consisting of one tunnel junction in series with a gate capacitance C_{g} and a voltage source V_{g}. The number of excess electrons on the island is n.

The simplest structure fulfilling these requirements is a so-called single electron box (SEB) consisting of one tunnel junction in series with a gate capacitance C_{g} and a voltage source V_{g} as shown in Fig. 1.1. The total charge of the island is now quantised and characterised by the number of excess electrons n on the island, associated with a charging energy $E_{\mathrm{C}} = e^2/2(C + C_{\mathrm{g}})$. The effect of the voltage V_{g} is to change the polarisation charge in the gate capacitance and thus the effective charge of the junction becomes $Q = V_{\mathrm{g}}C_{\mathrm{g}} - ne$. The charging energy of the whole circuit can be calculated by treating the junction as a regular capacitance after the last tunnelling, and it obtains a form

$$E_{\mathrm{Ch}} = \frac{(V_{\mathrm{g}}C_{\mathrm{g}} - ne)^2}{2(C_{\mathrm{g}} + C)}. \tag{1.2}$$

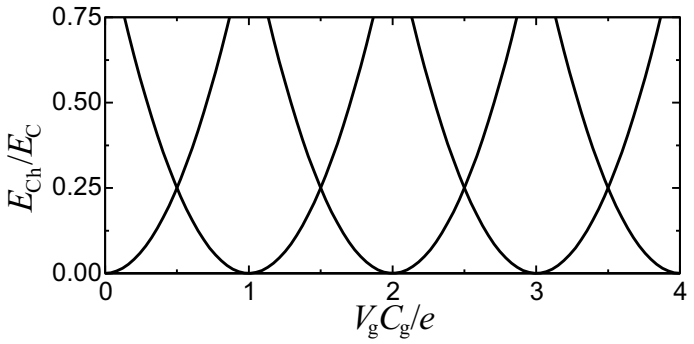

FIGURE 1.2 Charging energy of the single electron box consisting of a set of parabolas each corresponding to a certain value of n given by the x coordinate at the minimum. $E_C = e^2/2(C + C_g)$ is the charging energy of the SEB.

This represents a set of parabolas as a function of V_g, each one corresponding to a certain value of n. These parabolas are separated by C_g/e in x direction as depicted in Fig. 1.2. From the figure one can immediately see that the number of electrons n is stable, yielding the minimum energy if the voltage is between $e(n - 1/2) < V_gC_g < e(n+1/2)$. As soon as V_g reaches the value $e(n+1/2)/C_g$, an electron tunnels into the island and n is increased by one, i.e., one electron has been 'added to the box'. Thus, it is possible to control the number of electrons on the island one by one by the voltage V_g. At zero temperature this control is accurate but at finite temperatures the sharp changes in n are smeared by Boltzmann distribution. This quantisation of the island charge and controlling it by the gate voltage was first demonstrated experimentally in [90].

1.2.2 Single electron transistor

Another simple device with only one island is a single electron transistor (SET). It is composed of two tunnel junctions in series with bias voltage V. In addition, a gate voltage V_g is capacitively coupled to the island through C_g. The schematic view of a SET is shown in Fig. 1.3. The major difference compared to the SEB is that now an electron can tunnel onto the island trough one junction and discharge the island by tunnelling out via another one, thus inducing a net current through the device.

The total charging energy is of the same form as in the case of SEB except that one has to include the work done by the voltage source V in carrying a charge through the device:

$$E_{Ch} = E_C \left(u^2 + 2CV/e\right) - peV, \tag{1.3}$$

where $E_C = e^2/2C_\Sigma$ is the charging energy, $C_\Sigma = 2C + C_g$ is the total capacitance of the island and $u = V_gC_g/e - n$. Integer number p is the number of electrons tunnelled through the system, sometimes called a *flow index*. Figure 1.2 represents also the energy of the SET but only in case of $V = 0$ and with $E_C = e^2/2C_\Sigma$. If the

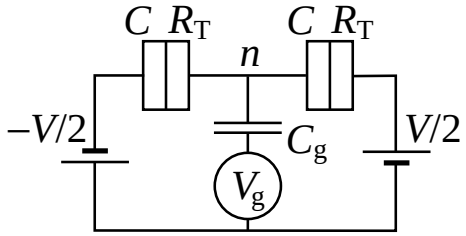

FIGURE 1.3 Schematic view of a single electron transistor. The system is assumed to be symmetric with both junctions having the same capacitance C and tunnelling resistance R_{T}. The gate voltage V_{g} is connected to the island through capacitance C_{g} and the system is biased with voltage V.

gate voltage is zero, $V_{\mathrm{g}} = 0$, the energy of $E_{\mathrm{C}} - eV/2$ is needed to charge the island by one electron. At zero temperature this energy has to be provided by the bias voltage, and therefore the current cannot flow, if $|V|$ is smaller than e/C_{Σ}. At voltages above that the current is linear, i.e., ohmic with an offset $\pm e/C_{\Sigma}$ and a slope determined by the tunnelling resistance, $I = V/R_{\mathrm{T}} \pm e/C_{\Sigma}$. This phenomenon of suppression of the current at small voltages is called *Coulomb blockade* and it makes it possible to have a well fixed number of electrons n on the island.

As in the case of SEB the gate voltage can be used to change the effective charge of the island as seen in Eq. 1.3. This makes the threshold voltage of Coulomb blockade depend on the gate charge. By electrostatic considerations one finds that n is stable inside the regions

$$e\left(n - \tfrac{1}{2}\right) < \tfrac{1}{2}C_{\Sigma}V + C_{\mathrm{g}}V_{\mathrm{g}} < e\left(n + \tfrac{1}{2}\right). \tag{1.4}$$

This represents rhombic shaped regions in (V, V_{g}) plane and inside each region a certain n is stable and no current is flowing. This also makes possible to control the current by the gate voltage V_{g} at a suitably fixed bias voltage V [77]. That is why the device is called single electron transistor and it was first demonstrated experimentally already in 1987 [60].

Since at certain voltages near the Coulomb threshold the current is very sensitive to the gate voltage, it is possible to use the SET as an ultrasensitive electrometer [41, 87, 113] by connecting the system under study capacitively to the island. Due to this property the SET is also suggested to be used as a read-out device of a quantum bit consisting of the superconducting SEB ("squbit") [96, 116].

1.2.3 Devices with several islands

By increasing the number of islands and the complexity of the circuit it is possible to construct more sophisticated and versatile devices. However, usually the SEB and SET are still used as basic building blocks.

The simplest two island device is the single electron trap, i.e., an irreversible

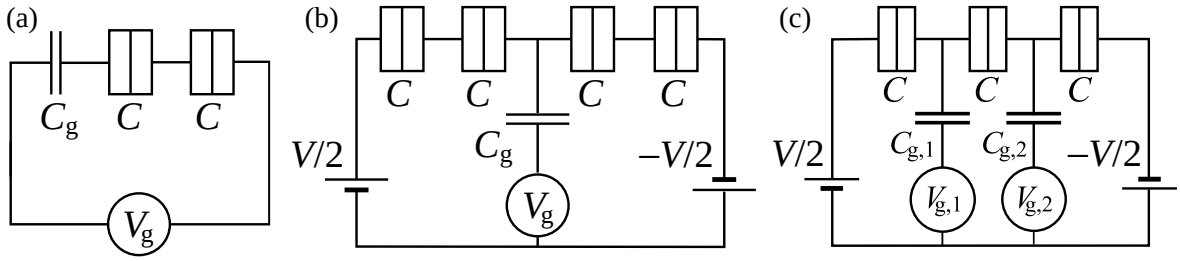

FIGURE 1.4 A schematic view of a (a) single electron trap, (b) turnstile and (c) pump.

single electron box. It is constructed by introducing a second junction in series with the one already included in a SEB as shown in Fig. 1.4(a). The behaviour of the single electron trap is very much similar to the box, except that it is hysteretic. This means that during the increase of gate voltage the threshold to move an electron onto the island is different from the value one has to reduce the voltage to, to get it out. (see, e.g., [51])

A different type of device is formed when connecting two traps together sharing the middle island with a gate voltage coupled to it. This device is called a single electron turnstile and it is depicted in Fig. 1.4(b). The principle of the device is to make use of the hysteretic behaviour of the trap and controllable transfer current through the array. The middle island can now be charged and discharged by tuning the gate voltage with suitable amplitude. The applied bias voltage V makes the trap structures hysteretic thus ensuring that the island is charged always from one direction and discharged into another. Hence it is possible to induce a DC-current through the device by applying a small bias voltage and an AC-drive of frequency f to the gate. The obtained current is $I = nef$, where n is an integer which depends on the amplitude of the AC-voltage. Turnstiles have been experimentally shown to operate well both in the normal metal state and also in superconducting state [9,62].

An interesting device can be formed by extending a SET to include three junctions in series with gate voltages capacitively coupled to the two islands. This device is called a single electron pump and its superconducting counterpart Cooper pair pump is the main topic of this thesis. With pump it is possible to induce a DC-current (*pumped current*) without any bias voltage by varying the gate voltages, e.g., by applying two sinusoidal AC-voltages with 90° phase difference to the two gates. The current is again of the form $I = nef$ in the normal metal pump and $I = 2nef$ in the Cooper pair pump. Here f is the frequency of the applied AC-signal. The device is depicted in Fig. 1.4(c) and the operating principles are discussed in more detail in the following chapters.

2 Josephson tunnelling

2.1 Superconductivity

Superconductivity was observed for the first time in 1911 by Kamerlingh Onnes in Leiden [105, 106, 107], when he noted the resistance of mercury to completely disappear below the temperature of liquefied helium. Since that, this same phenomenon of vanishing of resistance in a small temperature range at a so-called critical temperature T_c has been observed in many metals and compounds. The critical temperature is a characteristic of the material and the *perfect conductivity* at temperatures below it has been proven by the current flowing in the superconducting ring over a year without any attenuation. The measured decay constant of this *supercurrent* was not less than 100,000 years [56].

Another important property of a superconductor is the *perfect diamagnetism* [98], i.e., any magnetic field inside the metal is expelled as the metal is turned into the superconducting state. This is called *Meissner effect* and it predicts the superconductivity to be destroyed in magnetic fields higher than the so-called *critical field* H_c. This has been experimentally verified and temperature dependence of the critical field has been empirically found to obey the formula $H_\mathrm{c}(T) \approx H_\mathrm{c}(0)\left[1-(T/T_\mathrm{c})^2\right]$ in type I superconductors. In type II superconductors vortices are formed at magnetic fields between the two critical fields $H_{\mathrm{c},1}$ and $H_{\mathrm{c},2}$. The vortices existing in this *mixed state* of superconductor, are normal in their center, thus enabling a flux quantum $\Phi_0 = h/(2e)$ to penetrate though the superconductor inside each of them. At second critical field the maximum density of vortices is reached and the material becomes normal.

There exists two main theories about the classical superconductivity. The BCS theory by Bardeen, Cooper and Schrieffer [23] is based on the microscopic properties of the Fermi-sea of electrons. It shows that even a very weak attractive interaction between electrons, e.g., the second order interaction via lattice phonons, causes electrons to form pairs, so-called *Cooper pairs* at low enough temperatures. These pairs are formed by electrons with opposite momentum and spin, and as a consequence of this pairing an *energy gap* Δ is opened around the Fermi surface in the density of quasiparticle states. The spatial extension of Cooper pairs is of the order of the coherence length $\xi_0 = 2\hbar v_\mathrm{F}/\pi\Delta$, where v_F is the Fermi velocity. The zero resistivity can be qualitatively explained by the Cooper pairs having a total spin of one and

thus acting like bosons, which condense to Fermi surface at low temperatures. These condensated 'bosons' do not interact with each other so they can conduct electricity without any attenuation. The most important prediction of the theory is the minimum energy $2\Delta(T)$ needed to break the pair, which induces a gap in the density of quasiparticle states. This gap increases from the zero at T_c to the maximum value of $2\Delta(0) = 3.528 k_\mathrm{B} T_\mathrm{c}$. Theory also yields the correct value for the jump in specific heat at T_c and the Meissner effect [98] can be derived from it. The principles of the BCS theory have also been successfully applied to explain superfluids [99, 130].

The other theory, Ginzburg-Landau (GL) theory [65] is more phenomenological and introduces a complex pseudowavefunction ψ as an order parameter in Landau's general theory of second order phase transitions. It is based on the variational principle and on the expansion of the free energy in powers of ψ and $\nabla\psi$. GL theory also includes coherence length defined as $\xi(T) = \hbar|2m^*\alpha(T)|^{-1/2}$, which characterises the distance over which $\psi(\vec{r})$ can vary without undue energy increase. Here m^* is the mass of the superconducting charge carriers ($\sim 2m_\mathrm{electron}$) and $\alpha(T)$ is the temperature dependent constant determined by the GL equation [65].

2.1.1 AC and DC Josephson effects

When two large superconductors with phases φ_1 and φ_2 of the (GL) order parameter $\psi(\vec{r}) = |\psi(\vec{r})|e^{i\varphi(\vec{r})}$, describing the collective state of the (BCS) Cooper pairs, are weakly connected to each other through the so-called *Josephson junction* [79], the supercurrent of the form

$$I_\mathrm{s} = I_\mathrm{c} \sin(\varphi_2 - \varphi_1) \tag{2.1}$$

is induced between these superconductors. In principle Josephson junction can be any kind of a weak link, but in this work it consists of a regular tunnel junction, described earlier in Ch. 1, with both electrodes made of a superconductor. The supercurrent I_s arises due to the overlap of the two wavefunctions across the junction and their interference with each other. The *critical current* I_c is the maximum current that the junction can support.

This same line of reasoning leads also to another important result: if voltage is applied across the Josephson junction the phase difference $\delta\varphi = \varphi_1 - \varphi_2$ will evolve according to

$$\frac{d\delta\varphi}{dt} = \frac{2eV}{\hbar}. \tag{2.2}$$

The two effects determined by Eqs. (2.1) and (2.2) are called the *DC* and *AC Josephson effects* and they were experimentally verified shortly after Josephson's prediction in [79]. The modern Josephson voltage standard used in many institutes of metrology, is based on these effects.

From (2.1) and (2.2) one can also derive the electrical work done by the current source and thus the energy stored in the junction while the $\delta\varphi$ is changing. This can

be obtained by integrating $\int I_s V dt = \int I_s \hbar/(2e) d(\delta\varphi)$, which yields

$$E = -E_J \cos \delta\varphi, \tag{2.3}$$

where $E_J \equiv \hbar I_c/2e$ is the *Josephson coupling energy*.

2.1.2 Ambegaokar-Baratoff formula

From the GL theory [65] one can derive the critical current I_c for the general weak link, 'bridge' in this case, of length $L \ll \xi$ and with the cross-sectional area of $\mathbf{A}$:

$$I_c = (2e\hbar\psi_\infty^2/m^*)(\mathbf{A}/L), \tag{2.4}$$

where ψ_∞ is the absolute value of the order parameter in both superconductors. By applying a similar reasoning to the case of tunnel junction, Ambegaokar and Baratoff worked out the expression for the critical current and thus for E_J in a Josephson tunnel junction [8]. The general expression with the two electrodes having energy gaps Δ_1 and Δ_2 can be obtained in the limit $k_B T \ll \Delta_1, \Delta_2$ [44]

$$E_J = \frac{2R_Q}{\pi R_T} \frac{\Delta_1 \Delta_2}{\Delta_1 + \Delta_2} \mathcal{K}\left(\frac{|\Delta_1 - \Delta_2|}{\Delta_1 + \Delta_2}\right). \tag{2.5}$$

Here $R_Q = h/(2e)^2 \approx 6.5$ kΩ is the resistance quantum for the Cooper pairs and $\mathcal{K}(x)$ is the complete elliptic integral of the first kind. In the case of identical superconductors, $\Delta_1 = \Delta_2 \equiv \Delta$, one obtains a general expression at any T

$$E_J = \frac{\Delta}{2} \frac{R_Q}{R_T} \tanh\left(\frac{\Delta}{2k_B T}\right). \tag{2.6}$$

2.2 Experimental techniques

Since the following sections treating the properties of the superconducting single charge, i.e., single Cooper pair devices involves also experimental data, it is useful to discuss the particular experimental principles at this point.

2.2.1 Sample fabrication

All the samples used in the experiments of this thesis were fabricated using electron beam lithography and self-aligning shadow evaporation techniques [43], which is the most commonly used combination of methods in fabrication of tunnel junctions. The basic shadow evaporation technique, in which two different evaporation angles are used with a stencil mask to form a tunnel junction between the tiny overlapping areas of the evaporated wires, is illustrated in Fig. 2.1.

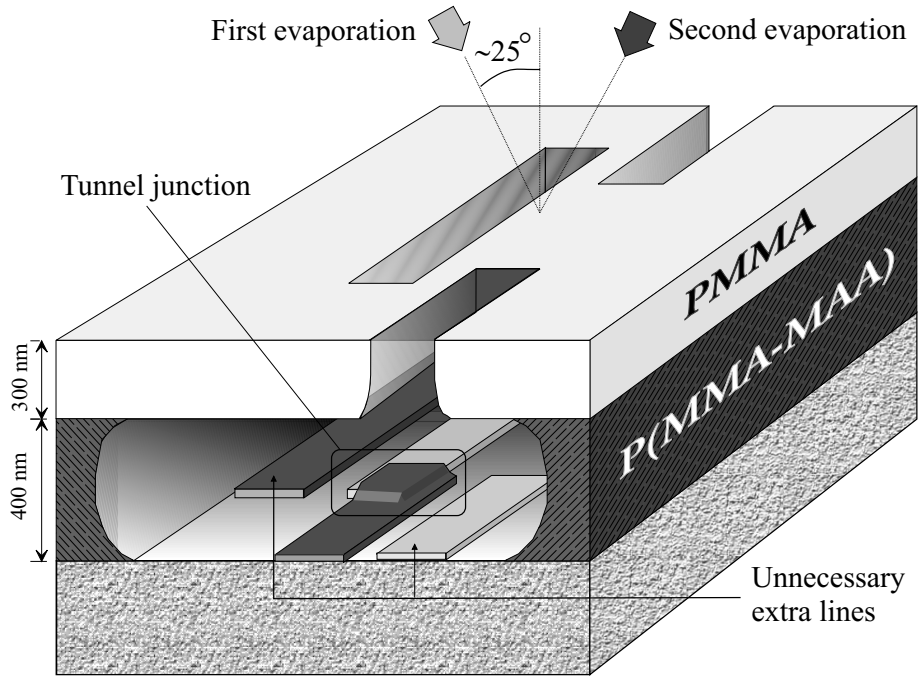

FIGURE 2.1 Principle of the self-aligning shadow evaporation technique. The tunnel junction is formed between the two metallic layers (usually Al) evaporated at different angles so that they overlap slightly. The tunnelling barrier is formed by oxidising the first layer before evaporating the second one. As a side effect of the technique there will be some extra lines, which are not used in measurements.

In fabrication of the aluminium samples the procedure was following: First, for the e-beam lithography a double layer resist of *poly(methyl methacrylate)* (PMMA) and copolymer (P(MMA-MAA)) containing PMMA and *methacrylic acid* (MAA), with thicknesses of 300 nm and 400 nm, respectively, was spun on an oxidized silicon substrate (see Fig. 2.1). The resists were baked at 160°C for 45 min (the bottom layer) and for 60 min (the upper layer). The patterns were drawn using a scanning electron microscope (SEM; JEOL JSM 840A) after which the sample was immersed in a mixed (1:2) solution of methyl-*iso*-butylketon (MIBK) and isopropylic alcohol for ∼30 s to develop the upper layer of the PMMA resist. The lower layer, P(MMA-MAA), was developed in a mixture of (1:2) methyl glycol and methanol for ∼8 s to produce the *undercut profile* shown in Fig. 2.1. Before evaporation the uncovered SiO_2 surfaces were cleaned in a reactive ion etcher (AXIC BenchMark) for 30 s at 30 mTorr pressure with 50 sccm flow of oxygen and 48 W RF-power.

The evaporation was done in an ultrahigh vacuum (UHV) chamber equipped with a cryopump (Cryo-Torr High vacuum pump, CTI-Cryogenics) and a liquid-nitrogen trap, the pressure being 10^{-8} - 10^{-9} mbar during the evaporation. The evaporation rate for the Al was ∼0.5 nm/s and layer thicknesses were 40 nm and and 60 nm. The tunnelling barrier was formed *in situ* by oxidising the surface of the first layer of Al under a steady flow of oxygen with pressure being usually ∼16 mbar for

three minutes. This produces a 1 - 2 nm thick layer of insulating AlOx, which acts as a tunnelling barrier. The oxidation parameters were slightly varied from sample to sample to obtain desired resistances. The process was completed by the *lift-off*, in which the sample was immersed in a warmed acetone to remove all the resists and the extra metal at the top of it, and final cleaning by reactive ion etching, with same parameters as before, to remove all the remnants of the resist.

In fabrication of the Cooper pair pump measured in Ref. [6] and briefly reviewed in chapter 6 the extra *ex situ* process was included to first pattern the larger structures; the contact pads, grounded shielding planes and gate lines for RF-signals. These structures were fabricated using the same method as described above except that only one angle was needed in evaporation and the material was chosen to be gold to prevent any possible problems with large superconducting planes and to ensure good electrical contact to the small Al structures. Also a thin layer of titanium was evaporated under the gold to improve adhesion. After that the sample itself was fabricated on top of this structure using the regular shadow evaporation processing with an extra aligning process step.

The self-aligning shadow evaporation method has been successfully applied for soft metals like Cu, Pb and Al, the last one being the most common material in single electron devices since it can be operated both in the normal and in the superconducting state, and especially because it easily forms a relatively stable tunnel barrier. However, recent developments in the field of superconducting devices have raised a new demand for a more suitable material with larger energy gap, Δ. One candidate for this is niobium (Nb) since its critical temperature is as high as 9.3 K yielding $\sim$1.5 meV for the gap, which is much higher than the 0.2 meV gap of aluminium. Yet, it is known to be difficult to apply self alignment technique for refractory metals like Nb due to a poor film quality usually obtained using it.

This deterioration of the Nb film is manifested as critical temperature T_c and thus the energy gap Δ being far below the bulk value [45, 72, 83]. One problem is the contamination of the Nb film by outgassing from the resists during the evaporation [45, 83]. To overcome this the authors of Refs. [45] and [44] used trilayer resist with bottom layer made of thermostable phenylen-ether-sulfone (PES) polymer, which has a glass temperature and decomposition temperature much higher than those of PMMA resist. By fabricating Nb wires with this process they reached T_c of 8.2 K. However, the process itself is more complicated than the conventional PMMA process. Even more complicated method was developed by authors of Ref. [109] where they used spin-on glass planarisation technique and several *ex situ* process steps to form wiring between vertical Nb/Al/AlOx/Nb-junctions fabricated *in situ*. Advantage of this process is the reliability of the insulating layer and the high quality of the superconducting Nb electrodes. Yet using this process it is difficult to reduce the size of the junction from (300×300) μm^2 and thus to increase the charging energy E_C, which is essential for single charge devices.

Almost all the earlier reports on the fabrication of superconducting single electron devices using niobium have come to a conclusion that it is not possible to make high quality Nb-based devices using conventional shadow evaporation technique with PMMA as a resist. Nevertheless, the Al/Nb/Al SETs used in the experiments in Ref. [7] and in chapter 3, were fabricated with regular shadow evaporation technique but along a slightly more sophisticated process compared to the samples made of aluminium. The modifications in fabrication process included slightly thicker bottom layer of the resist and thicker SiO_2 layer at the substrate, to provide larger undercut, which is essential for the fabrication ensuring the removal of remnants of the resist and therefore, reducing the outgassing during the evaporation. The outgassing was even more reduced by using a long distance ($\gtrsim$40 cm) between the Nb source and the sample during the evaporation thus reducing temperature of the evaporated Nb hitting the sample. To be on the safe side couple of extra steps were also performed, but the effectiveness of them is not very clear. After the etching and just before the evaporation, the mask was baked below 90° for 30 min to get rid of the possible moisture and to glaze the mask to endure the excessive heating by the niobium at the evaporation. The aluminum leads were evaporated first to enable the forming of the tunnelling barrier by oxidation and to provide an extra protective layer at the top of the resist, while evaporating the niobium. To ensure the stability and hardness of the evaporated Al layer it was let to cool down for at least 5 minutes before evaporating Nb.

2.2.2 Measurement setups

All the measurements included in this thesis were done at temperatures below 10 K using two different dilution refrigerators with different measurement setups. The measurements included in this chapter and in chapter 3 [7] were carried out in a small dilution refrigerator (Nanoway, PDR50) with the base temperature slightly below 100 mK. The temperature was usually measured using a resistance bridge (Picowatt AVS-47) and a carbon resistor, calibrated against the primary Coulomb blockade thermometer (Nanoway CBT). In measurements of chapter 3, we used a commercial calibrated Cernox resistor with good thermal anchoring in the very vicinity of the sample. Current and voltage measurements were done using the battery powered DL-Instrument's 1211 current preamplifier and the 1201 low-noise preamplifier, respectively.

The fridge was placed inside an electrically shielded room (Euroshield) which provided low external noise level for the measurements. The preamplified signals were conducted out of the shielded room through the highly efficient low pass filters (Euroshield) mounted in the wall and fed to the data acquisition card in a computer (NI PCI-6035E DAQ card). All the measuring wires in the cryostat contained commercial π-filters at room temperature and at 4.2 K. To reduce a heat leak, resistive

manganin wires were used between the filters. These wires were placed inside a CuNi tube for electric shielding. In addition, so-called strip filters were mounted into the lines at the sample stage and in measurements of chapter 3 also at the 1 kelvin plate. These filters were commercial stress gauges (KYOWA KFG-2-350-D1-23 and KFG-2-120-D1-23) squeezed between two ground planes forming continuous RC strip line filters [129]. The mounting of the sample was done using ultrasonic bonding with aluminium wires.

The measurements of the Cooper pair pump were carried out in an S.H.E. Corporation DRI-420 dilution refrigerator whose minimum temperature is $\sim$10 mK. Temperature was measured using directly the primary CBT thermometer or the carbon resistor calibrated by it. No shielded room was used, but the lower parts of the cryostat were surrounded by lead over the vacuum jacket in the helium bath for extra magnetic shielding. Due to the more sensitive measurements and the lack of shielded room an extra attention was paid to the filtering involved in the wiring.

The fridge has 14 highly filtered lines for DC-signals (Fig. 2.2 (a)). These lines include low pass filtering at three different temperatures. At room temperature we used again commercial low pass π-filters (Tusonix 4101, -55 dB at 100 MHz) which were connected directly at the top of the cryostat. From room temperature down to 600 mK all DC-signals are fed through coaxial cables with Nb as an inner conductor and stainless steel as the outer one. Between 600 mK and 60 mK plate we have 1.5 m long pieces of Thermocoax cable which also form the next filtering stage (-200 dB at 20 GHz) [134]. At both ends of Thermocoax cables there are 1 kΩ resistors in series to improve filtering at low frequencies (100 kHz $\lesssim f < 1$ GHz). The last filtering stage is at the sample stage at the base temperature. As before, these filters were continuous RC strip line filters made of commercial stress gauges (KYOWA KFG-2-350-D1-23). Short wires at the sample stage were made of Cu and were soldered to a printed circuit board (PCB). This again was ultrasonically bonded to the DC electrode of the sample with aluminium wires.

DRI-420 refrigerator has also four lines for RF-signals (Fig. 2.2 (a)). At room temperature we used 400 MHz low pass filters (Mini-circuits SBLP-400) and -6 dB fixed attenuators (Inmet). These were directly connected to the top of the cryostat and all other room temperature connections were made by using flexible SUHNER Sucoflex 104P cables with SMA connectors. From room temperature down to 4.2 K RF-signals are fed through Cu coaxial cables. At low temperatures we use BeCu coaxial cables, except that between 600 mK and the sample stage we use semirigid stainless steel coaxial cables for better thermal isolation. As a whole the RF lines have -33 dB attenuation at low temperatures: -20 dB at 4.2 K, -10 dB at 600 mK and -3 dB at the sample stage temperature (Inmet fixed attenuators). At the sample stage MCX connectors are used and all other connectors are of SMA type. The sample is directly ultrasonically bonded by Al bonding wire to a co-planar transmission line mounted on the sample stage. When all these lines are connected to the coldest parts

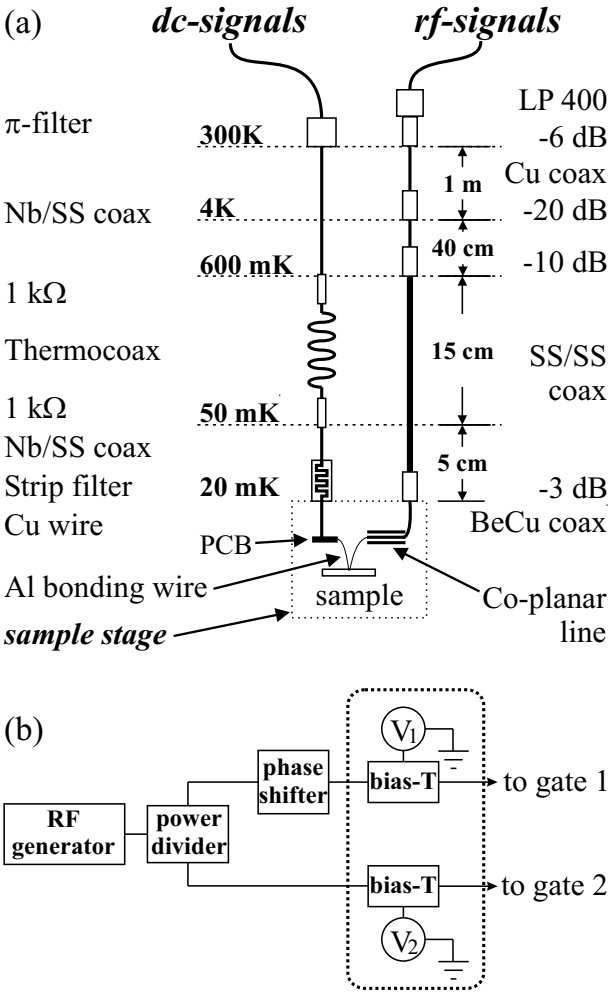

FIGURE 2.2 (a) Measurement wiring of the S.H.E. DRI-420 dilution refrigerator. (b) Schematics of the room temperature RF-signal connections. The dotted line shows the part included in the integrated domestic circuit. The compensation circuit was not needed in the measurements due to the low crosscoupling in the sample.

of the refrigerator, the base temperature is lifted up to ∼20 mK, as compared to the ∼10 mK base temperature without these lines.

Measurement of current was again done using the DL-Instrument's 1211 preamplifier but all DC-voltage measurements were done by using HMS Electronics model 568 low-noise preamlifiers. Both amplifiers were powered by battery sources only. Between preamplifier and data acquisition (NI PCI-6036E DAQ card) a domestic battery powered analog optoisolation was used to avoid ground loops and digital noise in the measurements.

In Fig. 2.2(b) we show schematics of the gating signal connections used in the experiment of the Cooper pair pump. For gating we used a HP8656B signal generator and divided the RF-signal by using an INMET 6014-2 power divider. One of these signals was fed through a phase shifter while the other went directly into the

custom made circuit [1] schematically consisting of two bias-Ts and a possibility to add negative crosscoupling between the two signals to compensate for the undesirable capacitive coupling between the gates in the CPP. The circuit also contained a high quality RF-circuit-board and optoisolated linking to the computer, which could be used to program all the gains used in bias-Ts, DC-offsets, compensation and as a main amplification. The control program[2] also included a possibility to automate the measurements.

2.3 Superconducting single island devices

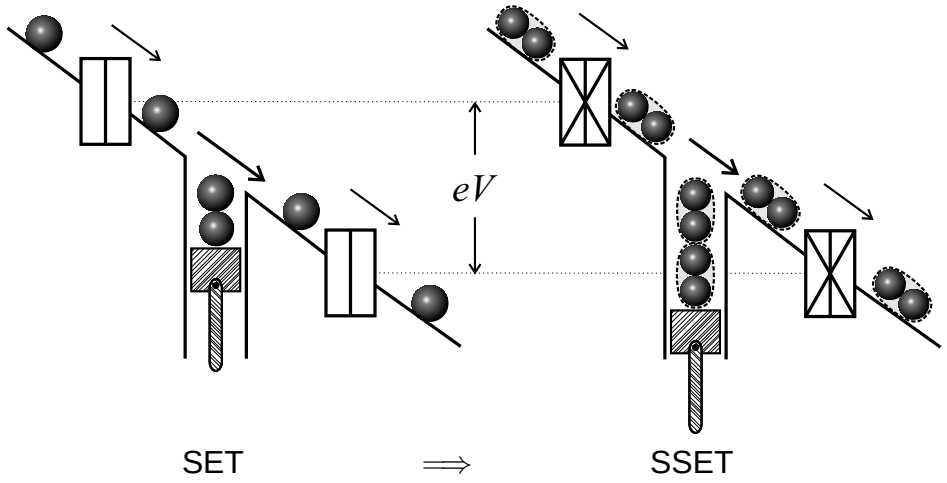

2.3.1 Parity effect in a superconducting SET

When all the metallic parts of the single electron transistor are superconducting the tunnel junctions become Josephson junctions and a new energy scale, Josepson coupling energy, E_{J}, starts to interplay with the charging energy. However, a more pronounced effects emerge due to the energy gap Δ, opened in superconductor, which is also the minimum excitation energy of the quasiparticles at zero temperature. If the number of excess electrons on the island n is odd there is one electron which cannot be paired and remains as a quasiparticle excitation, which raises the total energy of the system by Δ. If n is even all electrons can be paired and condensed into Cooper pairs. Otherwise the Coulomb energy, E_{C}, has the same form as in the normal state (1.3). This situation is illustrated in Fig. 2.3, where the charging energy is plotted as a function of gate charge q_{g} and with several different n, taking also the extra energy of Δ into account.

[1] Designed and constructed by Kari Loberg, at the Department of Physics, University of Jyväskylä.
[2] Made with LabView by Sampo Tuukkanen in his master thesis.

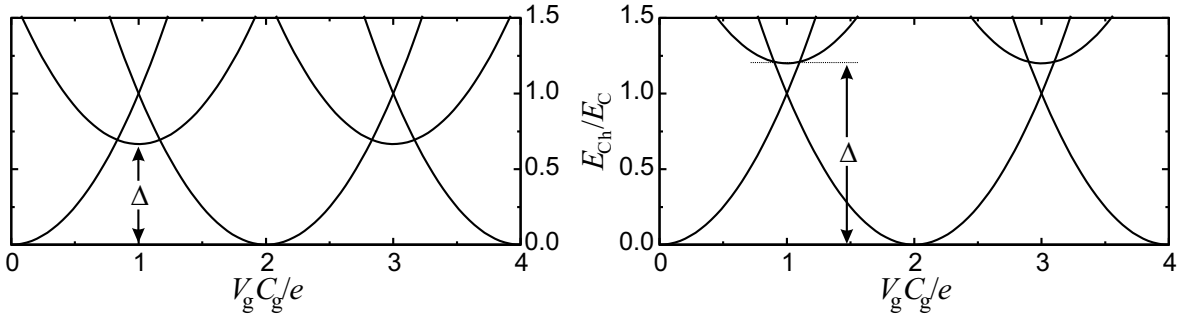

FIGURE 2.3 LEFT: Charging energy of the superconducting single electron transistor at $V = 0$, consisting of a set of parabolas each corresponding to a certain value of n given by the value of the x coordinate at the minimum. The states with odd n are lifted due to the minimum excitation energy Δ of the superconductor. RIGHT: The same plot in the case $\Delta > E_C$, which yields always the even n as a ground state. $E_C = e^2/2C_\Sigma$ is the charging energy of the SET.

On the left hand side of Fig. 2.3 Δ is smaller than E_C and it only changes the points where different parabolas cross each other and thus the ranges with odd n as a ground state are narrowing and those with even n are widening. If $\Delta > E_C$ as on the right hand side of the figure, the ground state is always given by even n. This also affects the Coulomb blockade oscillations in the current through the SET [17, 123], so that it becomes $2e$-periodic in V_gC_g. This so-called *parity effect* has been predicted in [22] and is artistically depicted in figure above. Experimentally it was verified for the first time in [126], where also a more general condition to observe $2e$-periodicity at any temperature, T, was derived. The minimum free energy of the quasiparticle excitation at finite temperature is

$$D(t) = \Delta(T = 0) - k_B T \ln N_{dg}, \tag{2.7}$$

where N_{dg} is the order of the degeneracy of the ground state with odd n and one non-paired electron, i.e., the number of different possibilities to choose the non-paired electron.

Usually the experimental observation of the $2e$-periodicity is not so easy as it sounds. First, it should be observed only in the supercurrent at zero bias or very small bias voltages $V \ll \Delta$. Nevertheless, it is not seen every time it theoretically should be. This discrepancy has been thought to be due to a high frequency noise and non-equilibrium quasiparticles at the sample from higher temparatures via measuring lines. The high frequency noise, which could break Cooper pairs and induce quasiparticle excitations inside the sample can be avoided by effective filtering at different temperatures along the measuring lines (see previous section). The non-equilibrium quasiparticles are more difficult to prevent and several methods have been suggested to reduce their appearance or effects due to them.

One trick is to embed normal metal parts to the biasing lines near the sample

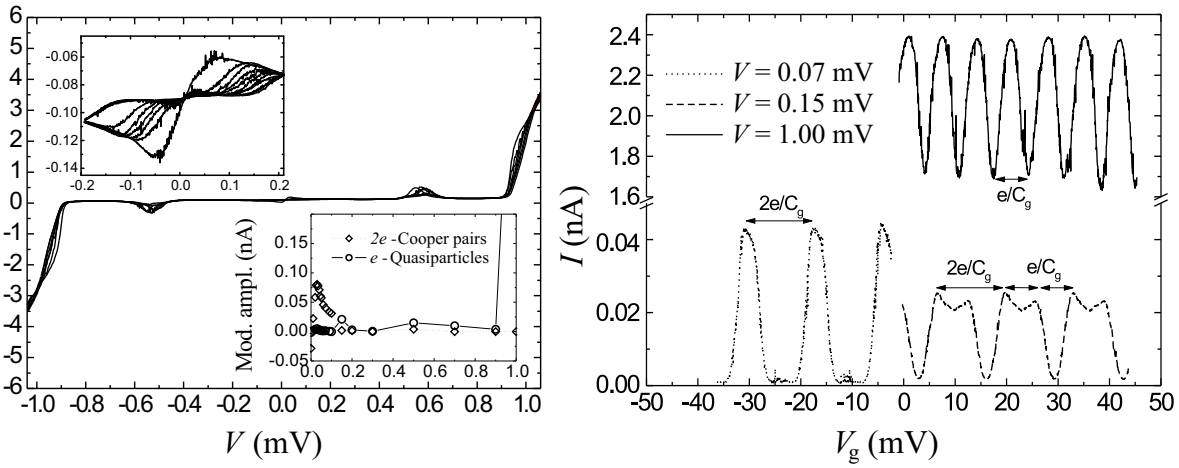

FIGURE 2.4 LEFT: I-V characteristics of a superconducting SET (SSET) measured at several different gate voltages $V_{\rm g}$. The upper left inset is the blow up from the small bias voltages showing the supercurrent and the lower right inset shows the amplitudes of the $2e$-periodic and e-periodic contributions to the Coulomb blockade modulation at several different bias voltages. Parity effect is seen only at small voltages and the large current at high voltages $V > 4\Delta \approx 0.9$ mV is due to the sequential tunnelling of electrons. RIGHT: Modulation curves measured at three different bias voltages showing a clear e-periodicity ($V = 1$ mV $> 4\Delta/e$), $2e$-periodicity ($V = 70$ μV), and combination of these two ($V = 0.15$ mV).

(At the distance $\lesssim 5$ μm) [80,89]. These would act as localised Fermi seas with plenty of free single electron states below the gap level Δ. Non-equilibrium quasiparticles can now 'drop' to these states from the top of the gap and get stuck on these so-called *quasiparticle traps*. The authors of [11] suggest another method and claim that $2e$-periodicity should be seen more reliably if the gap of the island is higher than in the two electrodes, $\Delta_{\rm Island} > \Delta_{\rm Electrode}$. This appears as an extra potential barrier to the quasiparticles and prevents them from entering the island. An extreme example of this behaviour was noted already in [48] where the authors observed clear $2e$-periodicity in normal-metal/superconductor/normal-metal -structures.

We have measured several superconducting SETs (SSET) to test whether the quasiparticle traps help to observe the parity effect or not. Statistical analysis was not done but the result was clear: parity effect was observed at small voltages in all of the measured samples with embedded traps and not observed in almost any of the samples without the traps. The total number of samples measured was over ten. I-V characteristics measured with several gate voltages $V_{\rm g}$ are shown on the left in Fig. 2.4. The upper left inset is the blow up from the small bias regime showing the supercurrent and its modulation by the gate. The lower right inset shows the amplitudes of the $2e$-periodic and e-periodic contributions to the Coulomb blockade modulation of the current at the different bias voltages. This clearly shows that the parity effect is seen at very small voltages, where the current is carried by Cooper pairs, i.e., by supercurrent. Since the tunnelling of Cooper pairs is elastic (if not

considering the effect of the electromagnetic environment, which is usually small, see chapter 4.2.1), it is forbidden at the bias voltages significantly different from zero. This is seen as a flat region with almost vanishing current in the I-V curves. The symmetric peaks at $V \simeq \pm 2\Delta/e$ are due to so-called Josephson quasiparticle cycle (JQP), where a Cooper pair tunnels through one junction and two quasiparticles through the other. At voltages higher than $4\Delta/e$ sequential tunnelling of electrons becomes possible. This is seen as a steep increase in the current at $V = \pm 4\Delta/e$ and the e-periodic modulation at voltages higher than that proves the current to be carried by electrons. On the right side of the figure we show the modulation curves measured at three different bias voltages exhibiting a clear e-periodicity ($V = 1$ mV $> 4\Delta/e$), $2e$-periodicity ($V = 70$ μV), and a combination of these ($V = 0.15$ mV).

The simplest Hamiltonian describing the SSET with Josephson coupling reads

$$H = H_{\rm ch} + H_{\rm J}. \tag{2.8}$$

The charging energy part of the Hamiltonian is of the form $\langle m|H_{\rm Ch}|m\rangle = E_{\rm Ch}(n = 2m)$, where $E_{\rm Ch}(n)$ is given by Eq. (1.3), and the Josephson part is obtained from Eq. (2.3), $H_{\rm J} = -\sum_{i=1,2} E_{{\rm J},i} \cos\delta\varphi_i$. The charge states $|m\rangle$, are the eigenstates of the $H_{\rm Ch}$ and $m = n/2$ means the number of the Cooper pairs on the island. The effect of the Josephson coupling is to remove the degeneracy at the crossing points of the even n parabolas of the charging energy $E_{\rm Ch}$ by opening an energy gap proportional to $E_{\rm J}$ as in the case of Bloch states. This is illustrated in Fig. 2.5(a) where the energy of the system is plotted as a function of normalised gate charge with several different values of the ratio $E_{\rm J}/E_{\rm C}$. The new eigenstates are superpositions of the charge states $|m\rangle$. This is illustrated in Fig. 2.5(b) for the two charge states $|m = 0\rangle$ and $|m = 1\rangle$. The eigenstates are now given by the superpositions $|\Psi_\pm\rangle = \alpha|0\rangle \mp \beta|1\rangle$, ($\alpha$ and β real) where $-$ and $+$ correspond to the ground state and the excited state and $\alpha^2 + \beta^2 = 1$.

If the gate voltage is now adiabatically changed from zero to $V_{\rm g} = 2e/C_{\rm g}$ the probabilities α and β are continuously changing so that one Cooper pair is coherently transferred through the junction in the direction depending whether the system is in its ground state or in the first excited state:

$$\left.\begin{array}{l} |\Psi_{-,i}\rangle \approx |0\rangle \\ |\Psi_{+,i}\rangle \approx |1\rangle \end{array}\right\} \Rightarrow \left\{\begin{array}{l} |\Psi_{-,f}\rangle \approx |1\rangle \\ |\Psi_{+,f}\rangle \approx |0\rangle \end{array}\right. \tag{2.9}$$

Coherent tunnelling of a Cooper pair is obtained if the operation is done adiabatically, i.e., the probability of band crossing, the so-called Landau-Zener (LZ) tunnelling is negligible [133]. This probability can be written as [38, 94]

$$P_{\rm LZ} = \exp\left(-\frac{\pi E_{\rm J}^2}{8\hbar E_{\rm C}\dot{q}}\right) \equiv \exp\left(-f_{\rm LZ}/f\right), \tag{2.10}$$

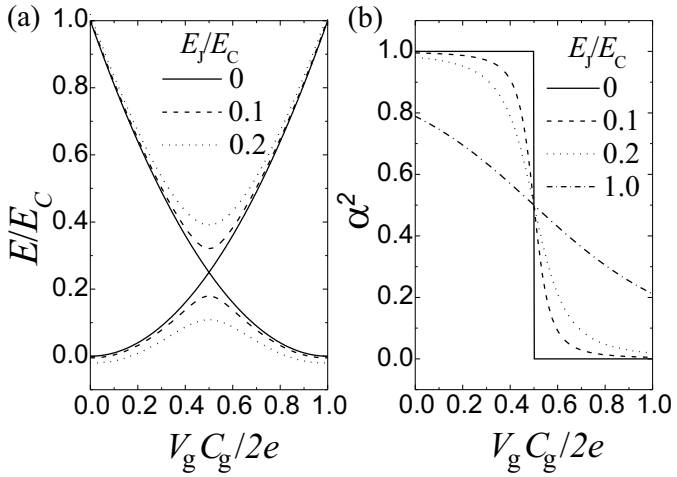

FIGURE 2.5 (a) The eigenenergy of the superconducting SET as a function of normalised gate charge with several different values of the ratio E_J/E_C in the ground state and in the first excited state. Two charge states, $|0\rangle$ and $|1\rangle$, are included in the calculation. (b) The eigenstates of the system are given by the superpositions $|\Psi_\pm\rangle = \alpha|0\rangle \pm \beta|1\rangle$, where $\alpha^2 + \beta^2 = 1$. α^2 is plotted as a function of the normalised gate charge.

where $q = V_g C_g/2e$ is the normalised gate charge, f_{LZ} is the Landau-Zener frequency determined from the equation above and $f \propto \dot{q}$ is the operating frequency.

2.3.2 Cooper pair box

The same parity effect applies also to the single Cooper pair box (SCB), i.e., a superconducting single electron box, so that the number of electrons on the island, n, is always changed by two as the gate voltage is varied. Thus, it is reasonable to talk about the number of Cooper pairs on the island, m_{SCB}, instead. This effect can be experimentally observed using a SET as an electrometer, (see Ch. 1.2.2), to measure the charge of the SCB island $u_{\mathrm{SCB}} \equiv m_{\mathrm{SCB}} - q_{\mathrm{SCB}}$. Here $q_{\mathrm{SCB}} \equiv C_{\mathrm{g,SCB}} V_{\mathrm{g,SCB}}/(2e)$ is the normalised gate charge. Since current in the SET, I_{SET}, is a function of the charge of the SCB island one expects to see a sawtooth like structure, when $V_{\mathrm{g,SCB}}$ is varied: value of u_{SCB} is changed along q_{SCB} until one Cooper pair tunnels onto or out of the island. This changes u_{SCB} back to the minimum value and the cycle starts over again, resulting in a sawtooth like behaviour as seen in Fig. 2.6, which shows the measurement of the SCB using the SSET as an electrometer.

A schematic picture and an SEM image of the measured sample is shown in Fig. 2.7. The sample consisted of a SCB and a SSET fabricated on the same silicon chip with islands capacitively coupled. Also the SCB was fabricated in the shape of an SET. This enabled the characterisation of the circuit by using it as a SSET. When the biasing lines are shorted, as during the measurement, the circuit forms a SCB. From the measured sample parameters one can determine that the periodicity of the sawtooth shown in Fig. 2.6 is $2e$-periodic.

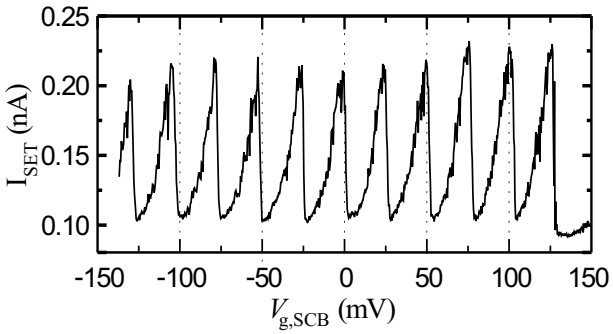

FIGURE 2.6 Charge (potential) of the SCB island as a function of gate voltage applied. The measurement was done using a SSET as an electrometer.

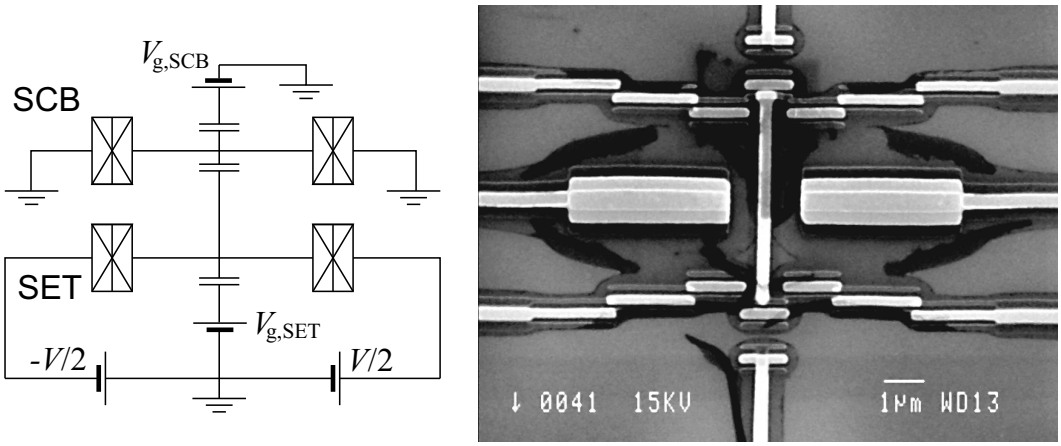

FIGURE 2.7 LEFT: A schematic view of the sample consisting of the single Cooper pair box with the island capacitively connected to the island of the SSET used as an electrometer. RIGHT: An SEM image of the sample measured. Large metallic planes at both sides between the SCB and SSET are ground planes, which reduce the direct crosscoupling of the $V_{g,SCB}$ to the island of the SSET. Three angle shadow evaporation was used to fabricate also the quasiparticle traps on the biasing lines *in situ*. The traps were made of copper, which is seen as slightly brighter areas, as compared to aluminium. Also an extra *ex situ* process step was necessary to fabricate the vertical line extending under the both islands and coupling them capacitively. The line has an electrical contact to the island of SSET but is galvanically separated from the SCB island by the evaporated layer of Al_2O_3.

3 Superconducting Al/Nb/Al SET

3.1 Benefits of using niobium

In most of the cases the undisturbed manipulation of the Cooper pairs is mandatory for the device to operate properly. Therefore, it is important to have a high suppression of quasiparticles. This can be obtained by the parity effect, as discussed in the previous chapter. However, the parity effect furthermore sets the upper limit for the charging energy (2.7), which usually also needs to be high. This can be a problem in the case of aluminium and certainly limits the range of useful sample parameters. The larger superconducting gap of niobium would push this limit higher and also provide a better suppression of the quasiparticle tunnelling, since the condition (2.7) is well fulfilled and tolerates better any additional sources of energy, e.g., high frequency noise.

The larger gap also produces a larger Josephson coupling energy E_{J} in ultrasmall junctions (2.5), which makes it possible to have both the high charging energy and the Josephson energy, and still have the high enough normal state resistance of the junctions R_{T}.

3.2 Measurements

The measured samples were superconducting SETs (SSET) with Nb island and Al electrodes consisting of two Nb/AlOx/Al junctions. Also the single Nb/AlOx/Al and Al/AlOx/Al junctions as well as all-aluminium SETs were measured as a comparison. The samples were fabricated along the recipes explained in Ch. 2.2.1 and all the measurements were carried out in a small dilution refrigerator (Nanoway, PDR50) with the base temperature below 100 mK. The measurement setup is explained in detail in Ch. 2.2.2. The schematics of the measurement and the SEM image of one of the measured SETs is shown in Fig. 3.1.

3.2.1 Characterisation of the samples

The charging energies, $E_{\mathrm{C}} = e^2/(2C_{\Sigma})$, where $C_{\Sigma} = 2C+C_{\mathrm{g}}$, of the SETs were derived from the normal state conductance curve measured at 4.2 K with magnetic field of $B \sim 5$ T [54]. Obtained charging energies varied between $E_{\mathrm{C}} \approx 34 - 78$ μeV. The

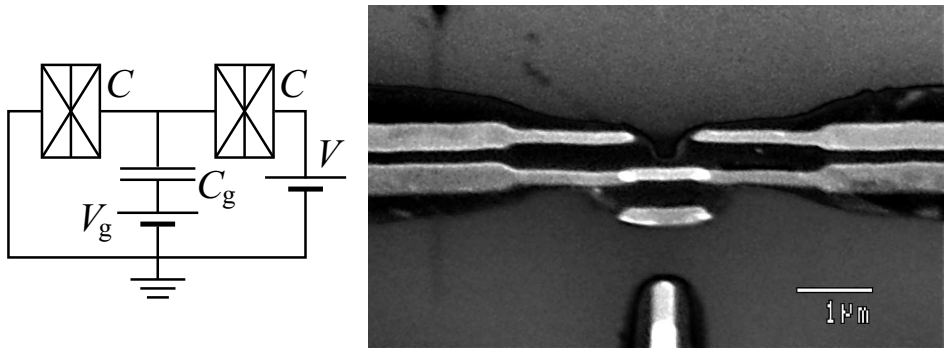

FIGURE 3.1 LEFT: The schematics of the measurement. RIGHT: SEM image of one of the measured samples. Brighter lines are niobium and darker aluminium.

Josephson coupling energy was obtained from Eq. (2.5) which yielded $E_J \approx 41-123$ μeV. Thus, the ratio E_J/E_C varied between 0.53 and 3.62.

The critical temperature T_c^{Nb} as well as the second critical field of niobium $H_{c,2}^{Nb}$ were determined from the zero bias conductance of the sample as a function of temperature or magnetic field, respectively. An example of determining T_c^{Nb} is shown in Fig. 3.2, where the sudden transition from the strong temperature dependence determined by the reduction of $\Delta_{Nb}(T)$, to the weaker dependence of Coulomb blockade [54], is clearly visible at the critical temperature. The critical temperatures obtained were 7.8, 8.1 and 8.5 K in the three best samples and above 7.5 K in all others. This is already very close to $T_c^{Nb} = 9.3$ K in bulk Nb and higher than in the earlier measurements of [44], [45] and [72]. The obtained critical fields were of the order of $H_{c,2}^{Nb} \approx 2.5 - 4.5$ T.

In Fig. 3.3 I-V characteristics and a dI/dV-curve are shown from one of the samples with $E_C \sim 35$ μeV and $E_J \approx 92$ μeV at temperature below 100 mK. The gap of width $4(\Delta_{Al} + \Delta_{Nb})/e$ is clearly visible and the maximums in the dI/dV-curve yield $\Delta_{Nb} \approx 1.45$ meV. Here we have assumed $\Delta_{Al} \approx 0.2$ meV [33, 61, 72, 126]. The oscillations seen in the dI/dV-curve near the supercurrent at $V = 0$ are explained in the next section.

An interesting observation is also that in every sample the steep raise of quasiparticle current at the gap voltage $|V| = 2(\Delta_{Nb} + \Delta_{Al})$ was very smeared, which can be seen also in Fig. 3.3. This smearing is quite common problem in Nb junctions and there is no recipe that would produce Nb junctions with very steep rise of quasiparticle current at the gap bias voltage. This feature has been typically associated with the difficulties in the fabrication of small junctions out off refractory metals that would degrade the quality of the junction and the material itself. In general, it looks as if the leak currents associated with the presence of subgap excitations are a constant feature of small Nb junctions. Below we sketch another possible explanation, which stems from more fundamental issues.

The Pippard coherence length of Al is $\xi_0^{Al} \approx 1.6$ μm, which is almost an order of magnitude larger than that of Nb, $\xi_0^{Nb} \approx 0.2$ μm. For pure metals, the Ginzburg-

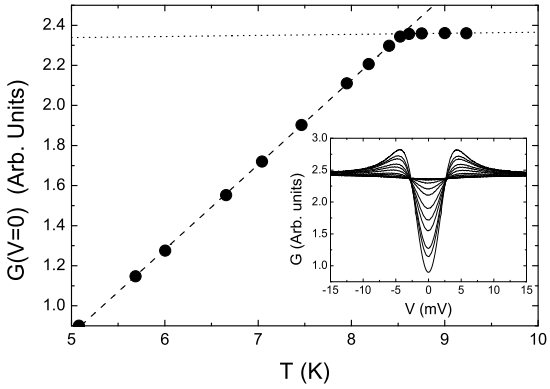

FIGURE 3.2 An example of determining the critical temperature, T_c, in one of the SSETs. Circles are the measured zero bias conductances obtained from the experimental dI/dV-curves shown in the inset. The dashed and the dotted lines are linear fits to the data below and above T_c, respectively.

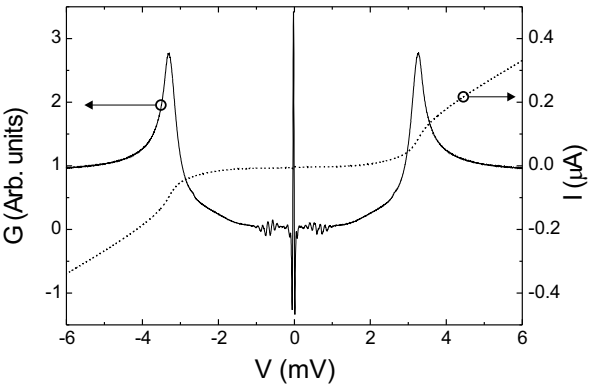

FIGURE 3.3 The I-V characteristics (solid) and dI/dV-curve (dotted) measured from one of the SSETs with $E_C \sim 35$ μeV and $E_J \approx 92$ μeV.

Landau coherence length $\xi(T) = 0.74\xi_0(1 - T/T_0)^{-1/2}$ will be then very different for Al and Nb at any temperature. In the case of thin films ($d \approx 30 - 40$ nm) we can assume that the mean free path ℓ is limited by surface scattering, therefore $\ell \approx d$. The Ginzburg-Landau coherence length for dirty films, e.g., thin films, $\xi(T) = 0.855\sqrt{\xi_0 \ell}(1 - T/T_0)^{-1/2}$ will then be still much larger in the case of Al. Furthermore, in real Nb films ℓ is often significantly shorter than the film thickness, $\ell \sim 3$ nm [83].

Although the GL equation is strictly valid only close to the critical temperature, in many situations it gives a good qualitative insight about what happens at low temperatures too. In our case, at T = 0 K we can see that the GL coherence length for Nb would be of about 21 nm, which is less than the film thickness, while for Al it is larger by a factor of ∼10. If one analyses the GL equation in the absence of magnetic fields [123], with $f = \psi/\psi_\infty$ as the reduced order parameter, $\xi^2(T)\Delta f + f - f^3 = 0$, we see that for samples with GL coherence length much larger than the thickness of the sample $\xi(T) \gg d$ the order parameter is constant. This means that for Al films, the superconducting order parameter is almost constant in a transversal section. In contrast, in Nb films this constraint does not hold. Therefore, the order parameter can vary across the sample and still satisfy the GL equation. Hence, there could be regions in the Nb electrode with a depressed or smeared gap. The current corresponding to tunnelling from/into these regions will appear at a smaller value of the bias voltage than $\Delta_{Al} + \Delta_{Nb}$ in one Al/AlOx/Nb junction.

The smearing could also be induced by the so-called *depairing* effect. This effect, due to a finite lifetime of quasiparticles near the energy gap Δ, smears the fea-

tures in the density of states and so also the I-V curves [46]. Niobium is a strong coupling superconductor, which usually have a high depairing effect and also thin Nb films are granular which emphasises the effect [47].

3.2.2 Resonant tunnelling of Cooper pairs

In three of the measured samples there exists clear oscillations in the dI/dV-curve near the supercurrent as seen in Fig. 3.3. These oscillations are due to gate dependent peaks as seen in the zoomed I-V curves plotted as a function of both the bias voltage V and the gate voltage $V_{\rm g}$ in the left hand side of Fig. 3.4. The pattern visible at the bias voltages below $V \lesssim 0.9$ mV has equal spacing in both V and $V_{\rm g}$, and appears at the onset of the superconductivity on the aluminium leads, while decreasing the magnetic field. Furthermore, it was verified that the position of the peaks does not depend on the value of the gap of the aluminum electrodes, which was tested by applying an external magnetic field.

The pattern is similar to the one observed usually in the case of so-called Josephson quasiparticle (JQP) cycles, where a Cooper pair tunnels through one junction and two quasiparticles through another [61], and thus the authors of [44], where similar pattern was observed, claim it to be due to that. However, the pattern is not due to JQP cycles since the features of it appear only at much higher voltages, $\Delta_{\rm Nb}+\Delta_{\rm Al}+E_{\rm C} \leq eV \leq \Delta_{\rm Nb}+\Delta_{\rm Al}+3E_{\rm C}$, which, e.g., for the sample of Fig. 3.3, yields 1.72 mV $\lesssim V \lesssim$ 1.87 mV [33, 101]. To rule out the possibility that these resonances would be due to the coupling of the Josephson oscillations to the electromagnetic environment of the sample, we have fabricated Al-only single junctions and SSET's with the same design and measured them in the same dilution refrigerator using the same set-up. The subgap conductances of these samples can be regarded as a spectral analysis of the environment, as seen by the sample. The obtained results showed that mild resonances do exist but only below 0.15 meV. Above this value (and up to the quasiparticle threshold voltage) the I-V's and the conductances were exactly flat, for all the samples measured. The strong gate dependency in the position of the peaks, as seen in Fig. 3.4, also proves them not to appear due to resonances in the electromagnetic environment.

The phenomena explaining these peaks is resonant tunnelling of Cooper pairs. If we consider the simplest and the most probable resonant tunnelling event where one Cooper pair tunnels onto or off the island through left or right junction in Fig. 3.1, we obtain the constraint

$$\tfrac{1}{2}C_{\Sigma}V \pm C_{\rm g}V_{\rm g} \pm Q_0 - e = 0 \tag{3.1}$$

for the necessary resonant condition in a symmetric SSET [76]. Here $-$ sign corresponds to tunnelling through the left junction and $+$ through the right one, Q_0 is the charge on the island before the tunnelling event, i.e., Q_0 is $n \times 2e$ or $n \times 2e + e$ de-

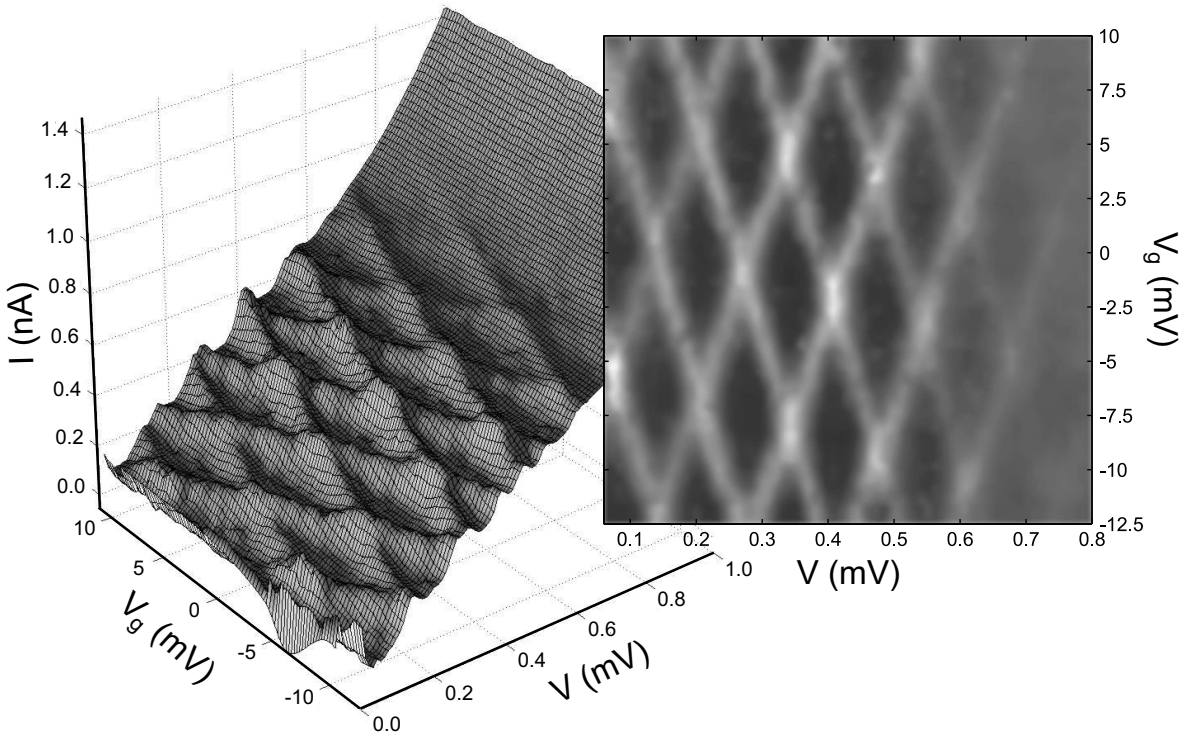

FIGURE 3.4 LEFT: The peaks appearing due to the resonant tunnelling of Cooper pairs as a function of both V and V_g. The data is measured from the sample with $E_\mathrm{C} \sim 37$ μeV and $E_\mathrm{J} \approx 89$ μeV while a small magnetic field $H \approx 23$ mT $\lesssim H_\mathrm{c}^\mathrm{Al}$ was applied. RIGHT: The same data as a contour plot with background subtracted, showing a clear diamond shaped pattern.

pending on the parity condition, and n is an integer. This equation yields a diamond shaped pattern in (V, V_g) plane for the resonances. The resonance tunnelling itself is not enough to carry a current since it only charges the island with $2e$. This excess charge has to be carried out by another process in the circuit before a next resonant tunnelling event can take place. This again requires inelastic tunnelling of quasiparticles, whose rate depends strongly on the electromagnetic environment [76,77].

If we take a closer look at the resonance peaks appearing in the measured data at $V \lesssim 0.9$ meV and plot them as a contour plot with the background subtracted, it explicitly demonstrates the diamond shaped pattern of the resonant tunnelling of Cooper pairs as seen in the right hand side of Fig. 3.4. If we let Q_0 in Eq. (3.1) be either e or $2e$, i.e., assume e-periodicity of the structure, the spacing of the measured pattern in the direction of V yields $E_\mathrm{C} \approx 34$ μeV, which agrees with the value $E_\mathrm{C} \sim 37$ μeV estimated earlier for that sample. The e-periodicity of the pattern indicates the presence of the non-equilibrium quasiparticles in our system.

3.2.3 q-MQT in superconducting SET

There exists also another interesting feature in the I-V curves; a smooth broader step in the baseline at around the same bias voltages as the resonance peaks. The position and the height of this step depend on the applied magnetic field as shown in Fig. 3.5(a), where the baselines of the I-V curves are plotted in various magnetic fields ranging from $H = 0$ to $H \gtrsim H_{\mathrm{c}}^{\mathrm{Al}}$. The baseline was obtained by simple averaging of the current over all the V_{g} values at certain bias voltage and over the bias range comparable to the spacing of resonance peaks. Thus the supercurrent is also unrealistically smeared in the figure. Figure 3.5(b) shows a more critical comparison between the position of this baseline step (peak in the conductance) in various samples and the gap of aluminium obtained by measuring the magnetic field dependence of a single Al/AlOx/Al junction. In Fig. 3.5(c) the same comparison is done for the height of the step obtained from the difference between the measured current and the current obtained with the highest magnetic field (Al in normal state; $\Delta_{\mathrm{Al}} = 0$) at the bias voltage in the middle of the plateau (minimum in the conductance). The figures clearly demonstrate that the step position and the height both follow the voltage determined by $V = 2\Delta_{\mathrm{Al}}/e$. Due to variations in the fabrication process (film thickness and purity) and in the measuring conditions, especially in the position of the sample inside the magnet, the critical field (in fact, the current in the magnet to obtain $H_{\mathrm{c}}^{\mathrm{Al}}$) varied from sample to sample. To overcome these deviations we scaled the current applied to the magnet by the current yielding $H_{\mathrm{c}}^{\mathrm{Al}}$ in that particular sample.

Since the feature of the baseline follows the voltage determined by $V = 2\Delta_{\mathrm{Al}}/e$, there has to be a tunnelling mechanism that activates at this bias voltage. Several processes are known to produce structures in the I-V curve of SSET at bias voltages below the quasiparticle branch [57,71], but most of them are excluded in this case by the fact that they leave an excitation on the island. This is forbidden, since at about $V = 2\Delta_{\mathrm{Al}}/e$ the system cannot provide enough energy to break the Cooper pairs in Nb ($\Delta_{\mathrm{Al}} \ll \Delta_{\mathrm{Nb}}$). In fact, only two processes are left: the so-called Andreev-Andreev cycle [57] and the elastic cotunnelling of quasiparticles [20,21].

The first one can be described as follows: an electron, i.e., electron-like quasiparticle in fact, is *Andreev-reflected* as a hole-like quasiparticle through the left junction, with the creation of a Cooper pair propagating to the right on the island. Then the same Andreev-like process happens at the right junction, resulting in an electron-like excitation propagating on the right electrode. The energy threshold for each of these processes is Δ_{Al}/e, therefore, neglecting the effect of the charging energy, it follows that the whole AA cycle should become important at about twice the gap of aluminium.

If this were the case for measured SSETs, it would mean that the Andreev-like reflection should be visible also in a single junction. To check this, we fabricated and measured several Al/AlOx/Nb single junctions. For this structure, the theory of

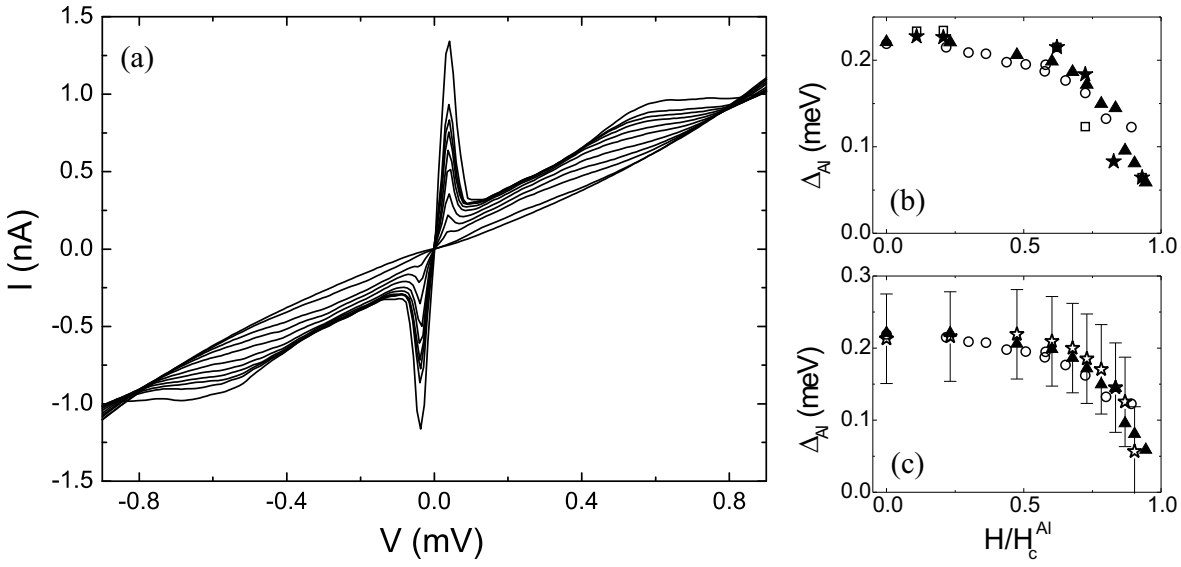

FIGURE 3.5 (a) Averaged over V_g I-V curves measured at several different magnetic fields ranging from $H = 0$ (highest absolute value of current) to $H \gtrsim H_c^{Al}$ (lowest absolute value of current). The baseline was obtained by simple averaging over the resonance peaks. (b) Comparison between the position of this baseline step in various samples and the gap of aluminium obtained by measuring the magnetic field dependence of a single Al/Al junction. Open circles are the data measured from single Al/Al junction and other symbols correspond to the data extracted from the I-V curves of three different samples. The I-V curves shown in (a) correspond to a sample marked as solid triangles. (c) The gap of the aluminium (circles) and step position (triangle) as in (b), as well as the height of the step (star) as a function of the magnetic field.

multiple Andreev reflection [32,84,103] and multiple-particle tunneling [75,114] predict a conductance peak (corresponding to a step in the current) at Δ_{Al}/e for a single Andreev reflection. In fact, the general structure predicted by these theories is much more complicated, with peaks at $2\Delta_{Al}/2ne$, $2\Delta_{Nb}/2ne$, and $(\Delta_{Nb} + \Delta_{Al})/(2n + 1)e$. None of these structures have been observed in our single-junctions. However, some leak currents at various voltages, probably due to other processes that one cannot yet characterize well, were seen. It was carefully checked that the activation voltage for these processes does not depend on the gap of Al (by sweeping the temperature up to the critical temperature for Al), therefore, even if they might contribute to the background current in the SSET, they cannot account completely for the variation of the current with the Al gap.

These measurements of the single junctions also rule out the possibility that the baseline feature would be due to the sequential tunnelling through the subgap quasiparticle states in Nb, which are the most probable reason for the smearing of the I-V characteristics as discussed before. If the observed baseline step would be due to these extra quasiparticle states it should be visible also at the single junction I-V curves [47] and it should show gate modulation with an amplitude comparable

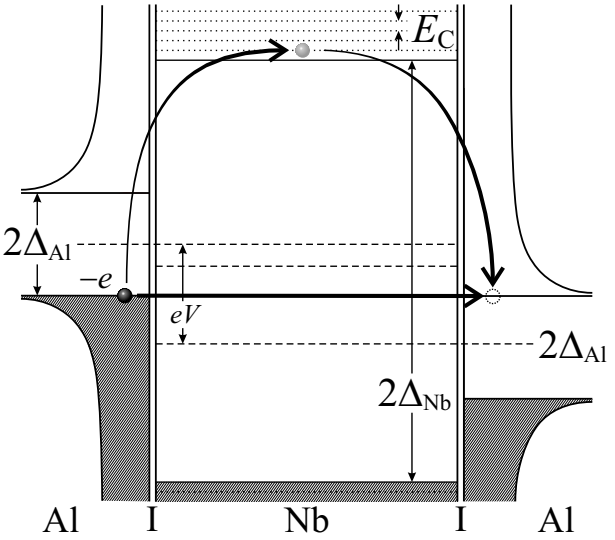

FIGURE 3.6 Schematic view of the elastic cotunnelling of an electron-like quasiparticle from the left electrode (below the gap of Al) to the right electrode (above the gap of Al), via a virtual excitation on the island with energy $E_{ex} > \Delta_{Nb}$. The effective and the virtual processes are shown by thick arrows. The vertical axis is the energy and the horizontal is the density of the electron states in the two Al electrodes. Dashed lines show the Fermi energy of the corresponding electrode or island and the dotted lines correspond to the Coulomb states in the island due to the charging energy E_C. It is clearly seen that the threshold voltage for the cotunnelling event to happen is $eV = 2\Delta_{Al}$. Since $E_C \ll \Delta_{Nb}$ the effect of the charging energy and thus the effect of the gate voltage is negligible.

to the modulation due to the resonant tunnelling of Cooper pairs. The lack of this feature in the single junction measurements and the lack of the gate modulation proves that this is not the case.

The second process (elastic cotunnelling) can explain the properties of the background feature as will be seen. Elastic cotunnelling means that an electron-like quasiparticle on the left electrode below the energy gap, i.e., with an energy $\epsilon < E_F - \Delta_{Al}$, tunnels onto the island as a virtual excitation. It stays on the island a time $\propto \hbar/\Delta_{Nb}$ (the charging energy in our case is negligible in comparison with the gap of Nb) then it tunnels into the right electrode above the energy gap as shown in Fig. 3.6. The whole process requires an energy $2\Delta_{Al}$ as the quasiparticle tunnelling in the regular Josephson tunnel junction. The theory of the elastic cotunnelling under a Coulomb barrier (that is, for normal-metal SET) has been developed in [20] and [67], and reviewed at [21].

Under the simplifying assumption that the tunnelling matrix elements are real and independent of the wave vector k the elastic contribution to the current at zero

temperature reads[1]:

$$I_{\rm el} = \frac{1}{eR_{\rm eff}} \int\limits_{\Delta_{\rm Al}}^{\infty} dE_{\rm L} \int\limits_{\Delta_{\rm Al}}^{\infty} dE_{\rm R} \frac{E_{\rm L}E_{\rm R}}{\sqrt{E_{\rm L}^2-\Delta_{\rm Al}^2}\sqrt{E_{\rm R}^2-\Delta_{\rm Al}^2}}\, T_{\rm eff}^2(E_{\rm L},E_{\rm R})\delta(eV-E_{\rm L}-E_{\rm R}), \quad (3.2)$$

where $R_{\rm eff} = R_{\rm T,1}R_{\rm T,2}/R_{\rm K}$, $R_{\rm T,1}$ and $R_{\rm T,2}$ are the resistances of the two junctions, and

$$T_{\rm eff}(E_{\rm L},E_{\rm R}) = 2\pi \int\limits_{\Delta_{\rm Nb}}^{\infty} dE \frac{E}{\sqrt{E^2-\Delta_{\rm Nb}^2}} \left[\frac{1}{E_1+E-E_{\rm L}} - \frac{1}{E_2-E+E_{\rm R}}\right] \quad (3.3)$$

where E_1 and E_2 are defined in [20].

One can readily see that the first formula is analog to the quasiparticle tunnelling current between two Al superconductors

$$I_{\rm qp} = \frac{1}{eR_{\rm T}} \int\limits_{\Delta_{\rm Al}}^{\infty} dE_{\rm L} \int\limits_{\Delta_{\rm Al}}^{\infty} dE_{\rm R} \frac{E_{\rm L}E_{\rm R}}{\sqrt{E_{\rm L}^2-\Delta_{\rm Al}^2}\sqrt{E_{\rm R}^2-\Delta_{\rm Al}^2}} \delta(eV-E_{\rm L}-E_{\rm R}), \quad (3.4)$$

with an effective junction resistance $R_{\rm T} \to R_{\rm eff}$ and with an energy-dependent normalised tunnelling matrix element $T_{\rm eff}$, describing the barrier formed by $\Delta_{\rm Nb}$. Usually it is assumed that $|T|^2$ is energy-independent and is included in the definition of $R_{\rm T}$. Also it shows that the elastic current starts at $2\Delta_{\rm Al}$ and the corresponding I-V feature will be step-like with the height proportional to the $\Delta_{\rm Al}$, as in the regular Josephson tunnel junction. In the limit of charging energy and bias voltages much smaller then the Nb gap, these equations indicate that $T_{\rm eff}$ is in fact independent of the energies E_1 and E_2. Therefore, one expects a gate voltage insensitivity of the background. All these predicted features agree with the measurements as seen in Fig. 3.5 for the $\Delta_{\rm Al}$ proportionality and in Fig. 3.4 for the gate insensitivity.

In a normal-metal SET the inelastic cotunnelling usually dominates over the elastic one, which is due to the fact $\epsilon \ll E_{\rm C}$, where ϵ is the spacing of the single electron states in the metal [18, 20]. Since any excitation with an excess electron in the island is now exponentially suppressed $I_{\rm inel} \propto e^{-D(T)/k_{\rm B}T}$ at low temperatures, the inelastic cotunnelling (which always leaves the excitation on the island) is significantly reduced. Here $D(T)$ is given by Eq. (2.7) with $\Delta_{\rm Nb}$. Also one might qualitatively interprete the lowest excitation energy of the island $\Delta_{\rm Nb} \gg E_{\rm C}$ as a spacing of the single electron states in the vicinity of the Fermi surface. This indicates the elastic cotunnelling being the dominant process.

[1] A better theory should be supplemented with a description of the diffusion of the electron inside the island as in [20, 21].

4 Decoherence in circuits of small Josephson junctions

4.1 Quantum computing

As mentioned already at the very beginning of this thesis, the rapid progress in the field of microelectronics during the past years and the strong effort to miniaturise any circuit have pushed the size of the electrical devices down steadily. This has, among other things, forced the information and computing science to reconsider its historical connection to classical physics, and expand the insight to include also quantum mechanics as a part of information theory. This has led to the emergence of a new field of *quantum computing* in 1980's and it has undergone a rapid development in 1990's.

Quantum computing connects the information theory very tightly to its physical realisation. From that point of view, it is no longer reasonable to talk about abstract information, but rather one has to always take into account the physical system the information is coded in. This means that information is part of the system and the amount of it affects the entropy of the whole system. Furthermore, this also yields that wasting of information costs energy, which was the key to the answer of the famous old thermodynamic paradox called *Maxwell's Demon*.

4.1.1 Qubit

Classical information is formed of bits, whereas quantum information is formed of quantum bits, so-called *qubits*. A classical bit can have a value 0 or 1, which is determined by a threshold property of a macroscopic system, e.g., voltage below or above 2.5 V. Thus, a register of n bits can have any of the 2^n values between $000\ldots0$ and $111\ldots1$. The qubit is usually presented and stored in a microscopic system, e.g., the electron or photon, where some definite and distinguished quantum mechanical states, $\{|\Psi\rangle\}_i$, represent the classical states 0 and 1 and form a basis. For example, the spin of an electron has the definite states $|\downarrow\rangle \equiv 0$ and $|\uparrow\rangle \equiv 1$ in magnetic field.

Unlike a classical bit, a qubit can also have any superposition of 0 and 1 as its value, e.g., $\sqrt{1/2}(|0\rangle \pm |1\rangle)$. Nevertheless, this does not mean the same as fuzzy logic, in which a classical bit is allowed to have any value between 0 and 1, but qubit contains also the quantum mechanical phase. For example, the state $\sqrt{1/2}(|0\rangle + i|1\rangle)$

is different from the states above. In general the state of the register with n qubits can be written in the form

$$|\Psi\rangle = \sum_{x=00\ldots0}^{11\ldots1} c_x|x\rangle, \tag{4.1}$$

where c_x are complex numbers satisfying the relation $\sum_x |c_x|^2 = 1$. Thus the register can simultaneously contain all the 2^n classical states in a superposition.

When measuring the state of the qubit it 'collapses', however, to either of the basis states so that the general state $|\Psi\rangle = \alpha|0\rangle + \beta|1\rangle$ gives an answer 0 with probability of $|\alpha|^2$ and 1 with probability $|\beta|^2$. Anyway, the basis of the qubit does not need to be fixed during the operations and we can perform measurement of the state as well using, e.g., the basis of $|\pm\rangle = \sqrt{1/2}(|0\rangle \pm |1\rangle)$. The same general state as above reads in this basis $|\Psi\rangle = \sqrt{1/2}[(\alpha+\beta)|+\rangle - (\alpha-\beta)|-\rangle]$, and the result is $|+\rangle$ with probability $|\alpha+\beta|^2/2$ and $|-\rangle$ with probability $|\alpha-\beta|^2/2$.

Another important difference between a qubit and a classical bit is that *an unknown state of a quantum bit cannot be fully copied*. This principle is a consequence of the nature of quantum mechanics and was proven by Wootters and Zurek, and by Dieks in 1982 [42, 132]. It prevents the use of regular classical error correction algorithms in qubits, since they always involve copying of the original bit, and it also prevents one to get around the principle of destructive measurement.

4.1.2 Entanglement

A general state of the register with n qubits (4.1) naturally contains all the combinations of the single qubit states, e.g., in the register of two qubits a state $\sqrt{1/2}(|00\rangle + |01\rangle) = |0\rangle \otimes \sqrt{1/2}(|0\rangle + |1\rangle)$, but it also contains the states like $\sqrt{1/2}(|00\rangle + |11\rangle)$, which cannot be expressed as a tensor product of the two single qubit states. It means that neither of the two qubits has a definite state of its own even if the system of these two qubits has a definite state [26]. This kind of states are called *entangled*. In the case of n qubits most of the states are entangled and the true power of quantum computing is based on the manipulation of the states like this.

The state $\sqrt{1/2}(|00\rangle+|11\rangle)$ mentioned above is the so-called EPR-state (Einstein-Podolsky-Rosen) and it has a maximal entanglement between the two qubits. This state can be used, e.g., to produce *superdense coding* [26] or *quantum teleportation* [24, 26]. In both of these phenomena the EPR-pair is split between the sender and the receiver so that the entanglement is not disturbed. For example quantum teleportation, in which an unknown quantum state is transferred far away, is achieved now by only sending two bits of classical data, e.g., by phone. Yet, this does not violate the rule of denied copying.

4.1.3 Gates and quantum parallelism

Classic computing is done using elementary logical gates. The output of a classic logical gate is usually one bit, whereas more than one input bit is often needed, e.g., in the AND-gate $\{(2\text{ bits}\mapsto 1\text{ bit}) : (11) \to 1; (01), (10), (00) \to 0\}$. The output can also include more than one bit, but almost all the time the number of input bits is larger than of output bits. Thus, this computing is *irreversible* and energy is lost during computation since every gate operation reduces the number of bits and so the total amount of information in the system is reduced. In quantum computing it is essential to preserve all the quantum mechanical properties of the state such as entanglement. Thus, the gates used in quantum computing are *unitary transformations*, which *reversibly* operate to the state vectors without losing any information. This also makes it possible to use tiny systems in computing, since there is almost no energy lost during the computation that would easily heat the small structures.

There are only three 'Basis' gates needed to form any gate in quantum computing. The usual choice for this basis consists of the *phase shift* gate:

$$\Phi(\varphi) = \begin{pmatrix} 1 & 0 \\ 0 & e^{i\varphi} \end{pmatrix}, \tag{4.2}$$

which can change the phase of the state, e.g., $\Phi(\varphi)(\alpha|0\rangle + \beta|1\rangle) = \alpha|0\rangle + \beta e^{i\varphi}|1\rangle$. Another gate needed is the *Hadamard* gate

$$\mathsf{H} = \frac{1}{\sqrt{2}} \begin{pmatrix} 1 & 1 \\ 1 & -1 \end{pmatrix}, \tag{4.3}$$

which can be used in creation of superposition states needed as an initial state in many computation algorithms, e.g., $2^{3/2}\mathsf{H}_1\mathsf{H}_2\mathsf{H}_3|000\rangle = |000\rangle + |001\rangle + |010\rangle + \cdots + |110\rangle + |111\rangle$. Both these gates are single qubit gates operating on one qubit. In addition, to form a full basis one needs a two gubit gate C-NOT (Controlled NOT)

$$\mathsf{C} = \begin{pmatrix} 1 & 0 & 0 & 0 \\ 0 & 1 & 0 & 0 \\ 0 & 0 & 0 & 1 \\ 0 & 0 & 1 & 0 \end{pmatrix} : \quad \mathsf{C}|y\rangle|x\rangle = |y \oplus x\rangle|x\rangle, \tag{4.4}$$

where $|x\rangle$ and $|y\rangle$ are any states of kind $\alpha|0\rangle + \beta|1\rangle$, and $y \oplus x$ means, in the case of classic logical states, that y is flipped if $x = 1$.

As mentioned above the register of qubits can simultaneously contain all the possible classical combinations as one superposition. Using this kind of a state as an initial state of the computation procedure one can simultaneously obtain the results corresponding to all the initial conditions by single computation. This is called a *massive quantum parallelism*. Nevertheless, making use of it is not as simple as it

sounds. Even the resulting state obtained by the parallel calculation contains all the answers corresponding to the different initial conditions, the measurement of this final state gives out only one result, which is chosen along the probability distribution determined by the multipliers in the superposition. Thus, to track out all the results and their probabilities one has to repeat the calculation at least as many times as there are different initial conditions and usually much more. This same amount of calculation would have been needed in solving the problem using classical computation and hence all the advantages of quantum parallelism have been lost. Therefore, it is essential to develop good computation algorithms, specially designed for the quantum computing, which can make use of all the advantages of quantum parallelism. The most famous quantum algorithms are encryption and cryptography algorithms [26, 120], the searching algorithm of Grover [70] and the Shor's factorisation algorithm that can be used to quickly decode the encryption methods used nowadays [118].

4.1.4 Realisation and decoherence

In principle, any quantum mechanical system, which can exist in any superposition of two basis states, can serve as a qubit. However, in realisation of such a device one has to take into account also the requirement that the system needs to be decoupled from the rest of the universe. That is the only way to preserve all the quantum mechanical information in the system. Any coupling, e.g., measurement, to the outside world would induce a growing entanglement between the system states and the states of the outside world. This process means that at the end the system does not have a state of its own, and the quantum *coherence* has been shared with the outside world, which makes the system behave as a classical statistical mixture instead of a pure quantum mechanical state with a definite phase.

This process is called *decoherence* and the stronger the coupling to the outside world is, the faster it is. This is why everyday physical systems behave classically [136]. In any macroscopic object the contact to the outside world is so strong that decoherence happens in a time scale too fast to perceive and we observe only classical behaviour of the system. We can also think that the outside world is constantly measuring the system and thus the wave vector of the (sub)system 'collapses'. The decoherence is one of the biggest problems in realisation of solid state qubits.

4.1.5 Squbit

The most obvious representation of a qubit would be any spin-1/2 particle, e.g., an electron, or a photon with two different polarisations. These options have been widely studied and in some experiments the qubit, which can be manipulated with lasers, has been successfully constructed using atoms or ions [25, 49, 50]. Also the

photon excitations in a microwave cavity have operated as a qubit and the entanglement between two qubits of this kind has been experimentally demonstrated [73,127].

The major disadvantage of the qubits above is that scalability is very questionable. It would be extremely difficult to increase the number of connected or interacting qubits in any of these systems. Thus, the suggestions to use superconducting nanostructures as a qubit, to be called *squbit* in what follows [14,30,31,95, 96,108,116,117], have gained lots of interest due to their relatively easy scalability and expandability to structures involving several squbits or even squbit networks. There have been several experiments in which the operation of a squbit has been successfully demonstrated in practice, with promisingly long decoherence times [4,15,28,35,36,52] potentially allowing quantum manipulations and application of specially developed error correction codes [35,59,102,128,131].

The principle of the squbit is based on the possible superposition of the charge states in the CPB [96] or in the arrays of Josephson junctions [14] (*charge squbit*), or on the superposition of supercurrents flowing in two different directions in SQUIDS (Superconducting quantum interference device) [108] (*flux squbit*). The simplest squbit is the CPB where the basis states can be chosen to be $|0\rangle$ and $|1\rangle$, with zero or one Cooper pairs on the island, respectively. As explained in Ch. 2.3, the Josephson coupling induces the new eigenstates of the system, which are superpositions of these charge states as shown in Fig. 2.5. The CPB can now be operated as a squbit by using only the ground state and the gate voltage to manipulate the multipliers in the superposition state.

4.2 Decoherence in superconducting nanostructures

4.2.1 'P(E)'-Theory

As described in the previous chapter decoherence is the most limiting phenomenon in realising a squbit, and it arises due to a coupling to the outside world. In case of Josephson junctions one of the major sources of decoherence is the electromagnetic environment in the vicinity of the sample. In most cases it is strongly coupled to the system under study and can have a significant effect on the behaviour of the circuit [1,53,77]. Fortunately, it is a controllable source of decoherence, unlike, e.g., random motion of background charges near the sample.

There exists a well developed theory of the electromagnetic environment and how it affects the tunnelling in small tunnel junctions [1,69,77,125]. Here only the results for a superconducting Josephson junction are presented. The environment is modelled as an infinite number of harmonic LC-oscillators, which can represent an arbitrary environment as explained in [34]. The dissipation in the system under study arises from the coupling of the degrees of freedom, i.e., Q and φ, to the degrees

of freedom of the environment. Here Q is the charge of the junction and φ is the Josephson phase across it. The Hamiltonian describing this coupling can be written in the form

$$H_{\rm env} = \frac{\tilde{Q}^2}{2C} + \sum_{n=1}^{\infty}\left[\frac{q_n^2}{2C_n} + \left(\frac{\hbar}{e}\right)^2 \frac{1}{2L_n}\left(\tilde{\varphi} - \varphi_n\right)^2\right], \tag{4.5}$$

where $\tilde{\varphi}(t) = \varphi(t) - (2e/\hbar)Vt$ and $\tilde{Q} = Q - CV$ are the fluctuations around the mean values determined by the bias voltage V (2.2). The symbols with subscript n correspond to the environmental LC-modes with frequencies $\omega_n = 1/\sqrt{L_n C_n}$. These modes are bilinearly coupled to the phase of the tunnel junction.

To calculate the supercurrent using (4.5) with environment taken into account, one has to treat the Josephson coupling (2.1) as a perturbation and use the *golden rule* to obtain probability rates for forward ($\vec{\Gamma}$) and backward ($\overleftarrow{\Gamma}$) tunnelling. These rates can then be written in the form [77]

$$\overrightleftarrows{\Gamma}(V) = \frac{\pi}{2\hbar} E_{\rm J}^2 P(\pm 2eV), \tag{4.6}$$

where the Gaussian like function $P(E)$ describes the probability of the system to emit (absorb) energy $E \geq 0$ ($E < 0$) to the environment during the tunnelling, thus making the tunnelling inelastic. The $P(E)$ function depends on the properties of the environment and can be calculated as a Fourier transformation

$$P(E) = \frac{1}{2\pi\hbar}\int_{-\infty}^{\infty} \exp\left[J(t) + \frac{i}{\hbar}Et\right] dt \tag{4.7}$$

of the so called *phase-phase correlation* function

$$J(t) = \langle[\tilde{\varphi}(t) - \tilde{\varphi}(0)]\,\tilde{\varphi}(0)\rangle, \tag{4.8}$$

which again can be calculated from the impedance of the electromagnetic environment $Z(\omega)$. The total impedance seen by the pure tunnelling element of the junction is the impedance of the environment parallel to the capacitance C of the junction:

$$Z_{\rm t}(\omega) = [i\omega C + Z^{-1}(\omega)]^{-1} \tag{4.9}$$

as illustrated in Fig. 4.1. The final form for the $J(t)$ can be obtained using the *fluctuation-dissipation* theorem [86]

$$J(t) = 2\int_0^{\infty} \frac{{\rm Re}Z_{\rm t}(\omega)}{\omega R_{\rm Q}}\left\{\coth\left(\frac{\hbar\omega}{2k_{\rm B}T}\right)[\cos(\omega t) - 1] - i\sin(\omega t)\right\} d\omega. \tag{4.10}$$

Since the sequential tunnelling events are uncorrelated the supercurrent can

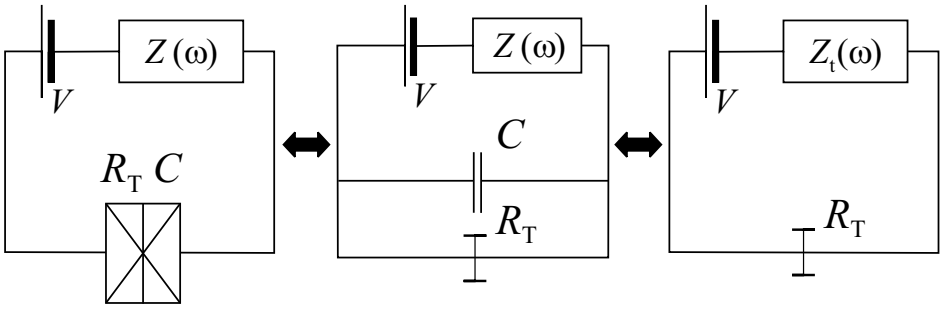

FIGURE 4.1 Description of the total external impedance seen by the pure tunnelling element of the Josephson junction. The total impedance is of the form $Z_{\rm t}(\omega) = [i\omega C + Z^{-1}(\omega)]^{-1}$

be calculated as a difference between the opposite tunnelling rates, which yields

$$I_{\rm S} = 2e\left[\vec{\Gamma}\,(V) - \overleftarrow{\Gamma}\,(V)\right] = \frac{\pi e E_{\rm J}^2}{\hbar}\left[P(2eV) - P(-2eV)\right]. \tag{4.11}$$

The $P(E)$ obeys the so-called *detailed balance relation* $P(-E) = P(E)\exp[-E/(k_{\rm B}T)]$, which indicates that at the low temperatures $P(E)$ is peaked around a positive E near zero. Thus, (4.11) represents the two antisymmetric peaks around the zero voltage, with the property $I(V=0)=0$. This is the usual shape of the supercurrent observed in experiments (see, e.g., Fig. 2.4). The smaller the environment impedance $Z(\omega)$ is, the sharper the peaks are, and more closer to zero bias they are located. On the limit of high environment $Z(\omega) \gg R_{\rm Q}$ the peaks are broad and centered around the bias corresponding to the charging energy $V = \pm E_{\rm C}/e$.

4.2.2 Decoherence due to electromagnetic environment

In small Josephson junctions the decoherence is closely related to *dephasing*, which means that the initially well defined Josephson phase φ across the junction becomes more and more arbitrary. This process is best characterised by the quantity $\langle[\varphi(t) - \varphi(0)]^2\rangle = \langle(\Delta\varphi)^2\rangle$, the deviation of the phase fluctuations from their value at $t = 0$. In charge squbits the phase needs to be fixed and thus the bias voltage has to be zero. Due to that, $\tilde{\varphi} = \varphi - (2e/\hbar)Vt = \varphi$ and the phase-phase correlation function $J(t)$ relates directly the Josephson phases at different times. This connection can now be used to relate the quantity $\langle(\Delta\varphi)^2\rangle$ to the electromagnetic environment [4]. Using $\langle\varphi(t)^2\rangle = \langle\varphi(0)^2\rangle$, which is a consequence of the stationarity of equilibrium correlation functions, one can write

$$\begin{aligned}\langle\Delta\varphi^2\rangle &= \langle\varphi(t)^2\rangle - \langle\varphi(0)\varphi(t)\rangle - \langle\varphi(t)\varphi(0)\rangle + \langle\varphi(0)^2\rangle \\ &= -\langle\varphi(0)[\varphi(t) - \varphi(0)]\rangle - \langle[\varphi(t) - \varphi(0)]\varphi(0)\rangle.\end{aligned} \tag{4.12}$$

Now using the fact that $\varphi(t)$ is hermitian one obtains

$$\langle(\Delta\varphi)^2\rangle = -2\mathrm{Re}J(t), \tag{4.13}$$

which directly relates the dephasing to the electromagnetic environment via phase-phase correlation function $J(t)$. One can also show that the decoherence rate is related to the same quantity [5]. To simplify the calculations, we do this only in the case of a CPB and with the basis of $\{|n\rangle\} = \{|0\rangle, |1\rangle\}$.

First, we have to split the Hamiltonian (4.5) to the energy of the pure environment $H_{\mathrm{env}} = \sum_j \hbar\omega_j(b_j^\dagger b_j + 1/2)$ and to the Hamiltonian, H_{int}, describing the interaction between the junction and its environment. Here $b_j^\dagger$ and b_j are the creation and annihilation operators of the bosonic environmental modes j with energy $\hbar\omega_j$, respectively. The total Hamiltonian reads now

$$H = H_{\mathrm{ch}} + H_{\mathrm{J}} + H_{\mathrm{env}} + H_{\mathrm{int}}, \tag{4.14}$$

and the total wavefunction Ψ is a tensor product of the charge state $|n\rangle$ and the state of the environment $|\vec{k}\rangle$: $\Psi = |n\rangle \otimes |\vec{k}\rangle$, where n is the number of Cooper pairs in the island and $\vec{k} = (k_1, k_2, \cdots)$ is the configuration of environmental modes with occupation numbers k_j. We can now write the *density matrix* $\rho^{\vec{k}}$ in the given basis as

$$\begin{aligned}\rho^{\vec{k}} =: \rho \otimes |\vec{k}\rangle = \Psi\Psi^\dagger \otimes |\vec{k}\rangle = \begin{pmatrix} a_1 \\ a_2 \end{pmatrix} (a_1^* a_2^*) \otimes |\vec{k}\rangle \\ = \begin{pmatrix} |a_1|^2 & a_1 a_2^* \\ a_2 a_1^* & |a_2|^2 \end{pmatrix} \otimes |\vec{k}\rangle := \begin{pmatrix} \rho_{11}^{\vec{k}} & \rho_{12}^{\vec{k}} \\ \rho_{21}^{\vec{k}} & \rho_{22}^{\vec{k}} \end{pmatrix}.\end{aligned} \tag{4.15}$$

In the density matrix the nondiagonal elements are directly related to the coherence of the state. If these so-called *coherence elements* are of the form $a_i a_j^*$ as shown in (4.15) the state is a pure quantum mechanical state. On the contrary if these elements vanish the density matrix has to be presented as a sum of different states and it represents a classical statistical mixture. Thus the effect of decoherence is to reduce these elements until they vanish.

Now the Hamiltonian describing the interaction between the CPB and the environment can be written in this basis as [34]

$$H_{\mathrm{int}} = -i\sqrt{\pi}\sum_j \hbar\omega_j \sqrt{\frac{Z_j}{R_{\mathrm{Q}}}} \begin{pmatrix} \left(b_j - b_j^\dagger\right) & 0 \\ 0 & -\left(b_j - b_j^\dagger\right) \end{pmatrix}, \tag{4.16}$$

where Z_j is the impedance of the mode j. In the interaction picture one can write: $H = H_0 + V$, where $H_0 = H_{\mathrm{Ch}} + H_{\mathrm{J}} + H_{\mathrm{env}}$ and $V = H_{\mathrm{int}}$ [37]. In this picture the state

vectors are given by $\Psi_{\rm I}(t) = e^{iH_0 t/\hbar}\Psi(t)$ and

$$
\begin{aligned}
V_{\rm I}(t) &= e^{iH_0 t/\hbar} V e^{-iH_0 t/\hbar} \\
&= -i\sqrt{\pi}\sum_j \hbar\omega_j \sqrt{\frac{Z_j}{R_{\rm Q}}}\left(e^{iH_0 t/\hbar} b_j e^{-iH_0 t/\hbar} - e^{iH_0 t/\hbar} b_j^\dagger e^{-iH_0 t/\hbar}\right)\begin{pmatrix}1 & 0\\ 0 & -1\end{pmatrix} \\
&= -i\sqrt{\pi}\sum_j \hbar\omega_j \sqrt{\frac{Z_j}{R_{\rm Q}}}\left(e^{i\sum\limits_k b_k^\dagger b_k\omega_k t} b_j e^{-i\sum\limits_k b_k^\dagger b_k\omega_k t} - e^{i\sum\limits_k b_k^\dagger b_k\omega_k t} b_j^\dagger e^{-i\sum\limits_k b_k^\dagger b_k\omega_k t}\right)\begin{pmatrix}1 & 0\\ 0 & -1\end{pmatrix} \\
&= -i\sqrt{\pi}\sum_j \hbar\omega_j \sqrt{\frac{Z_j}{R_{\rm Q}}}\begin{pmatrix}\left(b_j e^{-i\omega_j t} - b_j^\dagger e^{i\omega_j t}\right) & 0\\ 0 & -\left(b_j e^{-i\omega_j t} - b_j^\dagger e^{i\omega_j t}\right)\end{pmatrix}.
\end{aligned}
$$

In the last step the commutation rule $[b_i, b_j^\dagger] = \delta_{ij}$ was used. The equation of motion for $\rho_{\rm I}^{\vec{k}} := \rho^{\vec{k}}$ (for simplicity) is given by the *Liouville equation*:

$$
i\hbar\frac{d\rho^{\vec{k}}(t)}{dt} = \left[V_{\rm I}, \rho^{\vec{k}}(t)\right]. \tag{4.17}
$$

For the commutator $[V_{\rm I}(t), \rho^{\vec{k}}(t)]$ we obtain

$$
[V_{\rm I}(t), \rho^{\vec{k}}(t)] = -2i\sqrt{\pi}\sum_j \hbar\omega_j \sqrt{\frac{Z_j}{R_{\rm Q}}}\left(b_j e^{-i\omega_j t} - b_j^\dagger e^{i\omega_j t}\right)\begin{pmatrix}0 & \rho_{12}^{\vec{k}}\\ -\rho_{21}^{\vec{k}} & 0\end{pmatrix},
$$

which yields the differential equation for the coherence matrix elements $\rho_{12}^{\vec{k}}(t) = \rho_{21}^{\vec{k}*}(t)$

$$
i\hbar\frac{d\rho_{12}^{\vec{k}}(t)}{dt} = -2i\sqrt{\pi}\sum_j \hbar\omega_j \sqrt{\frac{Z_j}{R_{\rm Q}}}\left(b_j e^{-i\omega_j t} - b_j^\dagger e^{i\omega_j t}\right)\rho_{12}^{\vec{k}}(t).
$$

By integrating the differential equation from $t = 0$ to t we obtain

$$
\frac{\rho_{12}^{\vec{k}}(t)}{\rho_{12}^{\vec{k}}(0)} = \prod_j \exp\left\{-2i\sqrt{\pi}\sqrt{\frac{Z_j}{R_{\rm Q}}}\left[b_j\left(1 - e^{-i\omega_j t}\right) + b_j^\dagger\left(1 - e^{i\omega_j t}\right)\right]\right\}.
$$

Next we have to trace out the environmental configurations $\vec{k}$. This can be done using the relation $\sum_{\vec{k}} \rho_{ij}^{\vec{k}} = \rho_{ij}$ and applying the *Glauber formula* for non-zero temperature [66]:

$$
\left\langle \exp\left[\gamma\left(\nu b + \nu^* b^\dagger\right)\right]\right\rangle = \exp\left[-\frac{1}{2}|\nu|^2 \coth\left(\frac{\hbar\omega}{2k_{\rm B}T}\right)\gamma^2\right]. \tag{4.18}
$$

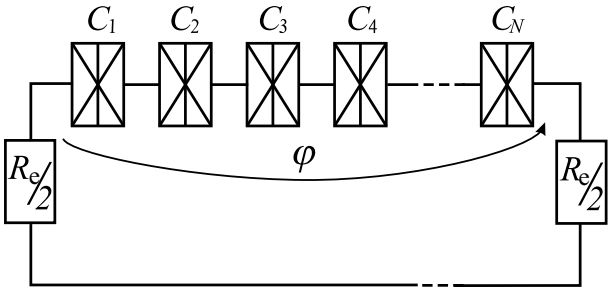

FIGURE 4.2 Schematic illustration of an N-junction array with purely resistive electromagnetic environment.

This yields

$$\frac{\rho_{12}(t)}{\rho_{12}(0)} = \prod_j \exp\left[\frac{2\pi Z_j}{R_{\rm Q}} \coth\left(\frac{\hbar\omega}{2k_{\rm B}T}\right)\left(1-e^{-i\omega_j t}\right)\left(1-e^{i\omega_j t}\right)\right].$$

As a last step we can get rid of the discreteness of the environmental modes ω_j using$\sum_j f(\omega_j)Z_j = \int_0^\infty \frac{d\omega}{\omega} f(\omega)\mathrm{Re}Z(\omega)$ [91]. Then

$$\frac{\rho_{12}(t)}{\rho_{12}(0)} = \exp\left\{-4\int_0^\infty \frac{d\omega}{\omega}\frac{\mathrm{Re}Z(\omega)}{R_{\rm Q}} \coth\left(\frac{\hbar\omega}{2k_{\rm B}T}\right)\left[\cos(\omega t)-1\right]\right\}, \tag{4.19}$$

whereby we finally arrive at

$$\frac{\rho_{12}(t)}{\rho_{12}(0)} = \exp\left[-2\mathrm{Re}J(t)\right]. \tag{4.20}$$

Thus as a consequence of coupling to the electromagnetic environment the coherence elements decay exactly at the same rate as in dephasing.

Using the method above the decoherence time can be calculated for any circuit with any kind of electromagnetic impedance. To keep the calculations more transparent only the case of an array of N superconducting tunnel junctions is considered here as an example, but it is straightforward to generalise the method also to other circuits with an arbitrary environment, $Z(\omega)$. The array is also assumed to be homogeneous, $C_1 = C_2 = \cdots = C_N \equiv C$, and the electromagnetic environment to be purely resistive $Z(\omega) = R_{\rm e}$ as shown in Fig. 4.2. With these assumptions we obtain using Eq. (4.9), for the total resistance seen by the array $Z_{\rm t}(\omega) = R_e/(1+i\omega\tau)$, where $\tau = R_{\rm e}C/N$. The real part of this can be written in a form

$$\mathrm{Re}Z_{\rm t}(\omega) = \frac{R_{\rm e}}{1+\omega^2\tau^2}. \tag{4.21}$$

Inserting this into Eq. (4.10) and using the result for $J(t)$ when $\mathrm{Re}Z_t(\omega)$ assumes the

Lorentzian form of Eq. (4.21) [39,68] we obtain an expression for $\langle(\Delta\varphi)^2\rangle$. In the limit of zero temperature ($T \to 0$) we immediately get for $t \gg \tau$ [4]

$$\left\langle(\Delta\varphi)^2\right\rangle = 4\frac{R_\mathrm{e}}{R_\mathrm{Q}}\left[\ln(t/\tau)+\gamma\right], \tag{4.22}$$

where $\gamma \simeq 0.57721$ is Euler's constant. In the case of non-zero temperature only the long time ($\pi k_\mathrm{B}Tt/\hbar \gg 1$) limit is relevant in most cases, except in the case of very large R_e. The long time expansion yields

$$\left\langle(\Delta\varphi)^2\right\rangle \simeq 4\frac{R_\mathrm{e}}{R_\mathrm{Q}}\left[\frac{\pi k_\mathrm{B}T}{\hbar}t - \ln\!\left(\frac{2\pi k_\mathrm{B}T\tau}{\hbar}\right)+\gamma\right], \tag{4.23}$$

which is valid only at non-zero temperatures and therefore Eq. (4.22) cannot be recovered from Eq. (4.23) in the limit of $T \to 0$. At a realistic measurement temperature, e.g. $T = 50$ mK, the result is valid in the range $t \gg 50$ ps, which is the region region of interest usually.

If we define the dephasing time τ_φ as the value of t for which $\langle(\Delta\varphi)^2\rangle = (\pi/2)^2$, we obtain

$$\tau_\varphi = \tau\exp\left(\frac{\pi^2}{16}\frac{R_\mathrm{Q}}{R_\mathrm{e}}-\gamma\right), \qquad (T=0) \tag{4.24}$$

and

$$\tau_\varphi \simeq \frac{\pi}{16}\frac{\hbar}{k_\mathrm{B}T}\frac{R_\mathrm{Q}}{R_\mathrm{e}}, \qquad (T>0). \tag{4.25}$$

For an array with $N = 3$ and $C = 10^{-15}$ F, and for the environment of the order of the free space impedance $R_\mathrm{e} = Z_0 \approx 377\ \Omega$ we obtain $\tau_\varphi \approx 2.7$ ns at zero temperature. A resistance of the environment of $R_\mathrm{e} = 100\ \Omega$, yields $\tau_\varphi \approx 1$ h. With the same parameters at $T = 50$ mK the decoherence is very fast: $\tau_\varphi \approx 0.51$ ns and $\tau_\varphi \approx 1.9$ ns for $R_\mathrm{e} = Z_0$ and $R_\mathrm{e} = 100\ \Omega$, respectively [4][1].

Figure 4.3 shows the dependence of τ_φ on the resistance of the environment, R_e, for a homogeneous three junction array at several different temperatures. Also the zero temperature limit (solid line) corresponding to Eq. (4.24), is shown. It forms an envelope curve for the finite temperature curves calculated from Eq. (4.23). It is also seen that only in the limit of low environmental resistance, $R_\mathrm{e} \leq 1\ \Omega$, one can obtain long enough decoherence times $\tau_\varphi > 1\ \mu$s at realistic measurement temperatures.

[1] **ERRATUM:** In [4] there is a minor quantitative error throughout the paper. In all equations there (especially in Eq. (1)) the resistance quantum $R_\mathrm{e} = h/e^2$ should be replaced by $R_\mathrm{Q} = h/(2e)^2$ corresponding to the charge of a Cooper pair and thus to the real Josephson phase. This yields an extra factor of four to the final results in there. Nevertheless, this does not affect the physical picture or the conclusions of the paper. This extra factor of four is taken into account in every result introduced here and also in the corrected Fig. 4.3.

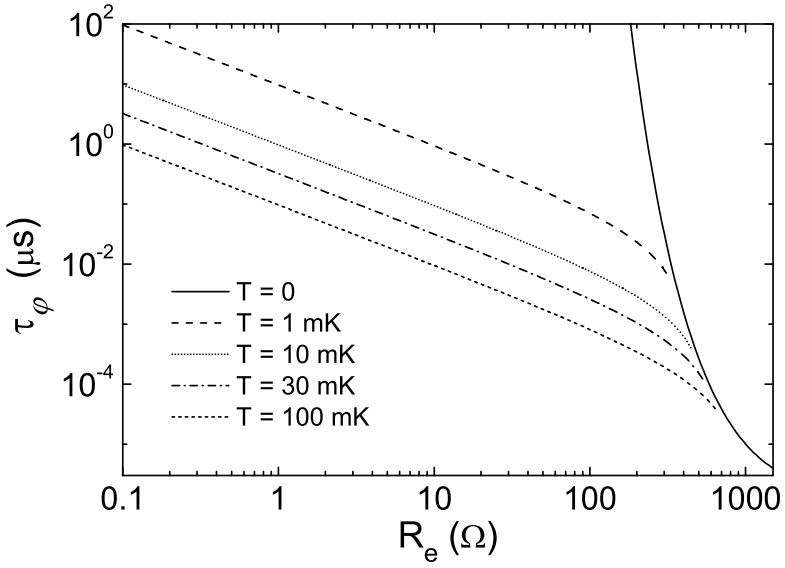

FIGURE 4.3 Dephasing time, τ_φ, for a three junction array as a function of the series resistance R_e of the electromagnetic environment. The array is assumed to be homogeneous with junction capacitances of 1.0 fF. The zero temperature curve forms an envelope of the curves corresponding to non-zero temperatures. The curves in the case of non-zero temperature are obtained using Eq. (4.23), and they are shown only over their range of validity.

This indicates that any normal metal part in the circuit would most probable induce extremely rapid decoherence. An efficient and maybe the only way to avoid rapid decoherence is to use all superconducting (closed) circuits as suggested, e.g., in [55].

5 Cooper pair pump

The Cooper pair pump (CPP) consists of three or more mesoscopic Josephson junctions in series with gate voltages capacitively coupled to each of the islands in between. It is in focus due to the many studies carried out concerning the parametric pumping of charge, an idea originally introduced by Thouless in 1982 [122]. This phenomenon is based on the ability of a propagating potential well to carry a charge q through a system. This again makes controlled pumping possible, by periodically changing the system parameters at a frequency f to induce propagation of charge during every cycle. This yields a DC-current $I = qf$ through the system.

The parametric pumping of charge can be obtained in many different kinds of devices, but most of the attention has been directed towards systems where the charge q passed through during each cycle is quantised at a certain number of electrons, $q = ne$, where n is an integer. This can be realised, e.g., by semiconductor quantum dots by varying the height of the tunnelling barriers [85] or by one-dimensional ballistic channels in a so-called SAW-pump, where the transport is induced by a surface acoustoelectric wave (SAW) [115, 121]. The most promising candidate so far is the so-called single electron pump consisting of an array of three or more mesoscopic metallic tunnel junctions in the Coulomb blockade regime [81, 82, 111]. Due to the Coulomb blockade the number of electrons in the islands of the array is very accurate and the pumping can be induced by phase-shifted gate voltages, yielding a current $I = nef$. Here f is the frequency of the RF-signal applied to the gates and the integer number n depends on the amplitude of the operating trajectory in the gate variables. These devices are more accurate than those based on semiconductors and they are able to provide high precision, even sufficient for metrological applications [81, 82]. Due to its high accuracy the single electron pump has been proposed to close the metrological triangle by providing the standard for electrical current [74, 81, 82, 92].

The only drawback in the single electron pump is the low operating frequency $f \lesssim 5$ MHz, which cannot provide high enough current for metrological applications. At higher frequencies the accuracy is lost due to coherent higher order charge transfer processes known as (in)elastic co-tunneling [18, 20, 63] and other sources of error discussed in [19], [58], [78] and [97]. The maximum operating frequency could possibly be pushed higher by using a Cooper pair pump (CPP). The pumping in the CPP is achieved similarly by the gate voltages and the charge is quantised at discrete numbers of Cooper pairs in the islands yielding a current $I = n2ef$. Due to the

coherent nature of Cooper pair tunnelling the operating frequency is now limited by the Landau-Zener (LZ) transitions [133], which yields several 100 MHz for the upper limit of the operation frequency, depending on the parameters of the device. For the same reason the CPP is also subject to intensive cotunnelling, which reduces the accuracy significantly in short arrays [2, 3]. To increase the accuracy one should use longer arrays or suppress the cotunnelling by other means [135, 104].

The CPP is of some interest also because it has been proposed that two capacitively coupled Josephson junction arrays similar to the CPP could form a squbit and also that the CPP could be used to transport information in a more complicated device [14]. When operated in a suitable electromagnetic environment the CPP could also provide a method to directly measure the decoherence time [5, 55] as will be explained later.

5.1 Model and Hamiltonian

The CPP is characterised by several energy scales. The ratio between the typical Josephson coupling energy and the charging energy, $E_{\mathrm{J}}/E_{\mathrm{C}}$, is a major parameter in determining the behaviour of the device. To be able to obtain pumping of single charges, we have to restrict ourselves to the limit $E_{\mathrm{J}} \ll E_{\mathrm{C}}$, where the dynamics are mainly determined by discrete tunnelling of charge carriers, i.e., Cooper pairs. In addition, the charging energy has to be larger than the thermal energy $k_{\mathrm{B}}T$ to prevent thermal excitations, but smaller than the superconducting gap Δ to prevent quasiparticle poisoning. This yields the usual chain of inequalities $k_{\mathrm{B}}T < E_{\mathrm{J}} \ll E_{\mathrm{C}} < \Delta$.

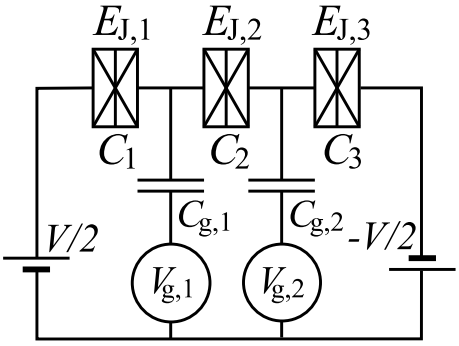

FIGURE 5.1 A superconducting array of three Josephson junctions (CPP). Here C_k and $E_{\mathrm{J},k}$ are the capacitance and the Josephson energy of the kth junction, respectively, and $C_{\mathrm{g},i}$ and $V_{\mathrm{g},i}$ are the gate capacitance and the externally controlled gate voltage of the ith island.

Including only Josephson and charging energies and neglecting quasiparticle tunnelling as well as other degrees of freedom the Hamiltonian of the system obtains the form of Eq. (2.8) as in the case of the SSET [2, 64]. The charging Hamiltonian H_{Ch}

can be calculated classically by treating all the junctions as capacitances as illustrated for the three junction CPP in Fig. 5.2 [64, 88, 111]. To include also the work done by the external voltage source due to the charge redistribution in the array, we have to include a load capacitance C_{L} in the calculations. The Lagrangian of the symmetric three junction CPP can now be easily written as the sum of the charging energies of all the capacitances (5.1). To clarify the congruity between the classical Lagrangian mechanics, the notation $V = \hbar/(2e)\dot{\varphi}$ (2.2) is used to represent the voltage drop across the junction.

$$\mathcal{L} = \frac{C}{2}\frac{\hbar^2}{(2e)^2}\left(\dot{\varphi}_{\mathrm{a}}^2 + \dot{\varphi}_{\mathrm{b}}^2 + \dot{\varphi}_{\mathrm{c}}^2\right) + \frac{C_{\mathrm{g}}}{2}\frac{\hbar^2}{(2e)^2}\left(\dot{\varphi}_{\mathrm{g},1}^2 + \dot{\varphi}_{\mathrm{g},2}^2\right) + \frac{C_{\mathrm{L}}}{2}\frac{\hbar^2}{(2e)^2}\dot{\varphi}^2, \tag{5.1}$$

where the indices are from Fig. 5.2 and the voltages are related by the *Kirchhoff's* rules:

$$\begin{aligned}
\dot{\varphi}_{\mathrm{a}} + \dot{\varphi}_{\mathrm{b}} + \dot{\varphi}_{\mathrm{c}} + \dot{\varphi} &= 0 \\
\dot{\varphi}_{\mathrm{g},1} + \dot{\varphi}_{\mathrm{a}} + (2e/\hbar)V_{\mathrm{g},1} &= 0 \\
\dot{\varphi}_{\mathrm{g},2} + \dot{\varphi}_{\mathrm{a}} + \dot{\varphi}_{\mathrm{b}} + (2e/\hbar)V_{\mathrm{g},2} &= 0
\end{aligned}$$

reducing the number of free parameters to three.

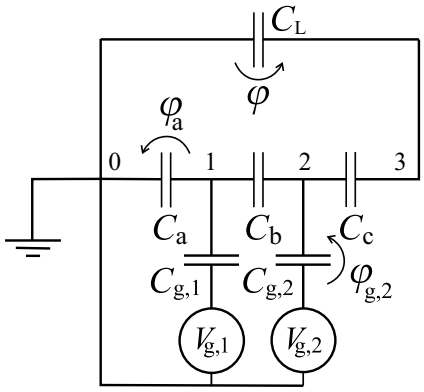

FIGURE 5.2 Classical schematics used in the calculation of the charging energy of the three junction Cooper pair pump. For clarity some of the most obvious variables are not shown in the figure.

The conjugate variable of φ_{x} is k_{x}, the number of Cooper pairs tunnelled through the junction (x is a,b or c), obeying the commutation relation $[\varphi, k] = i$. Since we are interested in the limit $E_{\mathrm{C}} \gg E_{\mathrm{J}}$ the phases of the single junctions φ_{x} are undetermined due to large quantum fluctuations. Due to the constantly flowing supercurrent k_{x} is not well defined either and thus it is not a good quantum number. Instead, the excess charges on the islands are good quantum numbers and their conjugate variables are *'phases of the islands'* φ_1 and φ_2. In addition, we must include the third free parameter which is the phase across the whole array $\varphi = \varphi_1 + \varphi_2 + \varphi_3$. Even

though the phases of the invidual junctions are undetermined, the total phase φ is constant of motion and thus fixed. We also determine the phases φ_3 and φ_0 (see Fig. 5.2) and the zero of the potential is chosen so that $\dot{\varphi}_0 \equiv 0$. The new variables can easily be expressed using the old ones through Kirchhoff's rules above:

$$\begin{aligned} \dot{\varphi}_\mathrm{a} &= -\dot{\varphi}_1 & \dot{\varphi} &= \dot{\varphi}_3 \\ \dot{\varphi}_\mathrm{b} &= \dot{\varphi}_1 - \dot{\varphi}_2 & \dot{\varphi}_{\mathrm{g},1} &= \dot{\varphi}_1 - (2e/\hbar)V_{\mathrm{g},1} \\ \dot{\varphi}_\mathrm{c} &= \dot{\varphi}_2 - \dot{\varphi} & \dot{\varphi}_{\mathrm{g},2} &= \dot{\varphi}_2 - (2e/\hbar)V_{\mathrm{g},2}. \end{aligned}$$

Inserting these new variables into Eq. (5.1) we can write the Lagrangian in the matrix form:

$$\mathcal{L} = \frac{1}{2}\frac{\hbar^2}{(2e)^2}\dot{\varphi}_i C_{ij}\dot{\varphi}_j - \frac{\hbar}{2e}J_i\dot{\varphi}_i, \qquad (i,j=1,2,3) \tag{5.2}$$

where we have, for clarity, not written the sums explicitly out but the existence of the same index twice means summing over it. Symbol C_{ij} is the capacitance matrix defined as

$$C_{ij} \equiv C\begin{pmatrix} \alpha_\mathrm{g} & -1 & 0 \\ -1 & \alpha_\mathrm{g} & -1 \\ 0 & -1 & \alpha_\mathrm{L} \end{pmatrix} \quad \text{and} \quad J_i \equiv \begin{pmatrix} Q_{\mathrm{g},1} \\ Q_{\mathrm{g},2} \\ 0 \end{pmatrix}. \tag{5.3}$$

Here $\alpha_\mathrm{g} := 2 + C_\mathrm{g}/C$, $\alpha_\mathrm{L} := 1 + C_\mathrm{L}/C$ and $Q_{\mathrm{g},i} := C_\mathrm{g}V_{\mathrm{g},i}$. Now the canonical momenta can be calculated using the definition

$$P_i = \frac{\partial\mathcal{L}}{\partial\frac{\hbar}{2e}\dot{\varphi}_i} = \frac{\hbar}{2e}C_{ij}\dot{\varphi}_i - J_i \quad \Rightarrow \quad \dot{\varphi}_i = \frac{2e}{\hbar}C^{-1}_{ij}(P_i + J_i), \tag{5.4}$$

which yields

$$\begin{aligned} P_1 &= -\frac{\hbar}{2e}C\dot{\varphi}_\mathrm{a} + \frac{\hbar}{2e}C\dot{\varphi}_\mathrm{b} + C_\mathrm{g}V_{\mathrm{g},1} = Q_1 \\ P_2 &= -\frac{\hbar}{2e}C\dot{\varphi}_\mathrm{b} + \frac{\hbar}{2e}C\dot{\varphi}_\mathrm{c} + C_\mathrm{g}V_{\mathrm{g},2} = Q_2 \\ P_3 &= -\frac{\hbar}{2e}C\dot{\varphi}_\mathrm{c} + \frac{\hbar}{2e}C_\mathrm{L}\dot{\varphi} = -Q_\mathrm{c} + Q_\mathrm{L} := Q \end{aligned} \tag{5.5}$$

The Hamiltonian describing the charging effects can now be calculated from the Lagrangian

$$\begin{aligned} H_\mathrm{Ch} &= \frac{\hbar}{2e}\dot{\varphi}_i P_i - \mathcal{L} \\ &= \frac{\hbar}{2e}\dot{\varphi}_i P_i - \frac{1}{2}\frac{\hbar^2}{(2e)^2}\dot{\varphi}_i C_{ij}\dot{\varphi}_j + \frac{\hbar}{2e}J_i\dot{\varphi}_i \\ &= \tfrac{1}{2}P_i C^{-1}_{ij}P_j + J_i C^{-1}_{ij}P_j, \end{aligned} \tag{5.6}$$

where we have used the right hand side of Eq. (5.4). Since usually $C_\mathrm{g} \ll C$ one can approximate $\alpha_\mathrm{g} \approx 2$. Now, by inserting all the variables into Eq. (5.6) and keeping track only of the terms depending on Q_1 or Q_2, we obtain the charging part of the Hamiltonian

$$H_\mathrm{Ch} = \frac{E_\mathrm{C}}{3 - 2/\alpha_\mathrm{L}} \left[\left(2 - \frac{1}{\alpha_\mathrm{L}} \right) u_1^2 + 2u_2^2 + 2u_1 u_2 - 2u_1 \frac{q}{\alpha_\mathrm{L}} - 4u_2 \frac{q}{\alpha_\mathrm{L}} \right], \tag{5.7}$$

where $u_i = n_i - q_i$, $n_i = Q_i/(2e)$, $q_i = -Q_{\mathrm{g},i}/(2e)$, $q = Q/(2e)$ and $E_\mathrm{C} = (2e)^2/(2C)$ is the unit of charging energy. The integer n_i is the number of Cooper pairs on the ith island. As mentioned before some constant terms are omitted or added for clarity.

To get rid of the load capacitance C_L and to describe the Cooper pair pump with a bias voltage V supplied, one has to consider the limit: $C_\mathrm{L} \to \infty$. This yields immediately $Q_\mathrm{L} \to \infty$ and $\alpha_\mathrm{L} \to \infty$. Nevertheless, the last two terms in Eq. (5.7) obtain a finite form:

$$\frac{Q}{\alpha_\mathrm{L} C} = \frac{Q_\mathrm{L} - Q_3}{C + C_\mathrm{L}} \xrightarrow[Q_\mathrm{L} \to \infty]{C_\mathrm{L} \to \infty} \frac{Q_\mathrm{L}}{C_\mathrm{L}} = V.$$

Thus, in this limit we may write

$$H_\mathrm{Ch} = E_\mathrm{C} \frac{8}{3} \left[u_1^2 + u_2^2 + u_1 u_2 - \frac{CV}{2e} (u_1 + 2u_2) \right] - p2eV. \tag{5.8}$$

Here we have added the necessary term $-p2eV$, which takes into account the fact that a Cooper pair can eventually tunnel through the whole array and the voltage source has to carry it back to the initial side of the array to retain the equilibrium. Integer p is the number of Cooper pairs tunnelled through the system as mentioned already in Ch. 1. At zero bias, $V = 0$, Eq. (5.8) yields a honeycomb like stability diagram shown in Fig. 5.3(a) [2, 6, 64]. Inside each hexagon the system is stable and there is one charge state $|n_1 n_2\rangle$, i.e., the eigenstate of the charging Hamiltonian, H_Ch, as a ground state. At the edges of the hexagons and at the triple nodes, two or three charge states are degenerate, respectively.

The other part of the total Hamiltonian (2.8) the Josephson (tunnelling) Hamiltonian is given by

$$\begin{aligned} H_\mathrm{J} &= -\sum_{k=1}^{3} E_{\mathrm{J},k} \cos(\varphi_k) \\ &= -\sum_{\vec{n},k=1}^{3} \frac{E_{\mathrm{J},k}}{2} (|\vec{n} + \vec{\delta}_k\rangle\langle\vec{n}| e^{i\varphi/3} + \text{ H.c. }), \end{aligned} \tag{5.9}$$

where $E_{\mathrm{J},k}$ and φ_k are the Josephson coupling energy and the phase difference across the kth junction, respectively. The tunnelling vector $\vec{\delta}_k$ describes the change

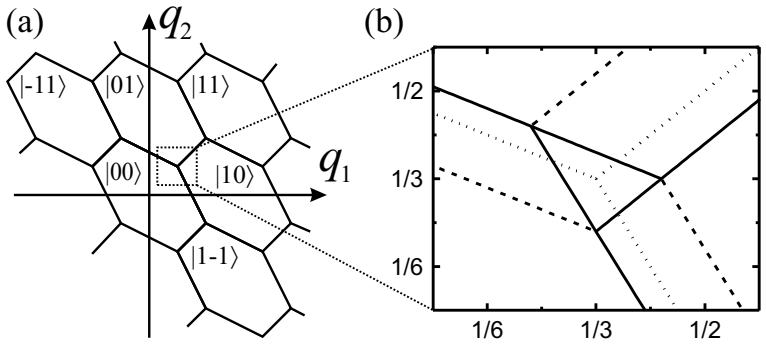

FIGURE 5.3 (a) Stability diagram of the CPP at zero bias $V = 0$ on the plane determined by the normalised gate charges $q_i = V_{\mathrm{g},i}C_{\mathrm{g},i}/2e$. The stable configuration inside each of the hexagons is shown by the kets $|n_1 n_2\rangle$. (b) Zoomed view of one of the triple nodes. The dotted lines correspond to $V = 0$. Solid and dashed lines show the resonance condition for Cooper pair tunnelling and cotunnelling in the presence of bias voltage $CV/2e = 0.1$.

of $\vec{n} = (n_1, n_2)$ due to tunnelling of one Cooper pair through the kth junction. Each tunnelling in the 'forward' direction is thus associated with a phase factor $e^{i\varphi/3}$. The Josephson coupling induces new eigenstates and an energy gap will open as explained in the case of the SSET in Ch. 2.3.1 [2, 94]. This model Hamiltonian is described in detail in [3], [12] and [13].

Tunnelling events in CPP take place as a coherent tunnelling of a Cooper pair, in which the system travels adiabatically from the initial charge state to the final charge state along the eigenstate of the full Hamiltonian of Eq. (2.8) (see Ch. 2.3.1). Thus a Cooper pair is tunnelled when the resonance in (q_1, q_2) plane is passed [17, 33]. Here the resonance means that the initial and the final charge state have the same energy. These resonances for the coherent Cooper pair tunnelling are shown as dotted and solid lines in Fig. 5.3(b) at $V = 0$ and $V > 0$, respectively. Similar resonances for the second order process, cotunnelling of a Cooper pair, are shown by dashed lines at $V > 0$. With zero bias these resonances and the first order resonances (Coherent tunnelling) overlap. Cotunneling of Cooper pairs (see, e.g., [93]) means the coherent tunnelling through two junctions simultaneously which is qualitatively similar to cotunnelling in normal state [18, 20, 63] or cotunnelling of quasiparticles in SSET explained in Ch. 3.2.3. This means that when passing the resonance at $V = 0$, e.g., between the states $|00\rangle$ and $|10\rangle$ the Cooper pair has some probability to tunnel in from the 'right' via the virtual state $|01\rangle$ involving two tunnelling events, instead of tunnelling through the 'left' junction. These cotunnelling events lead to the quantum inaccuracy of Cooper pair pumping, as will be shown in the next section.

5.2 Pumped current

Pumping of Cooper pairs at $V = 0$ is achieved by adiabatically varying the gate voltages along the path encircling one of the triple nodes. This is achieved, e.g., in the case of three junction pump by the sinusoidal signals fed to the gates with 90° phase difference producing a circular path around the node as shown in Fig. 5.4(a), or by the pulses shown in Fig. 5.4(b) which produce a triangular path.

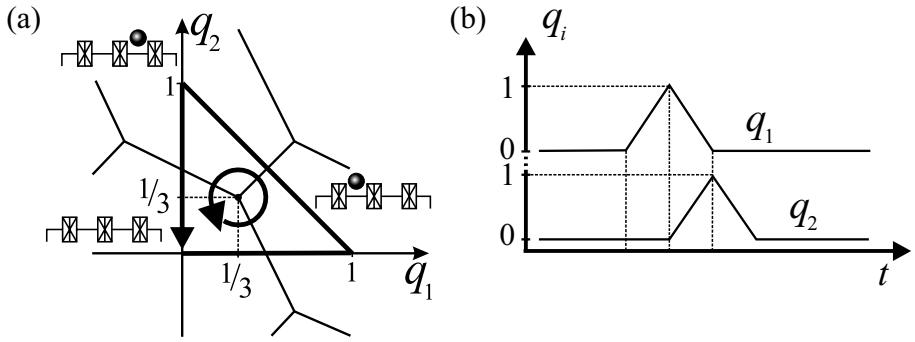

FIGURE 5.4 (a) The states with minimum charging energy of the uniform $N = 3$ pump on the (q_1, q_2) plane. The small schematic figures illustrate the stable charge configuration inside each hexagon. Two different pumping paths are shown by thick arrows. A circular path is produced by two sinusoidal gate voltages with 90 degree phase difference, and the triangular path by the gating sequence shown in (b).

The current pumped through an array of N junctions when circling around the pumping path can be calculated using the *adiabatic approximation* of quantum mechanics. The basis of instantaneous eigenstates $\{|m(t)\rangle\}$ with eigenenergies $\{E_m(t)\}$ of the full Hamiltonian (2.8) for a given $\vec{q}(t) = (q_1, q_2, \ldots)$, is introduced for each instant of time t. If the state of the system is $|m(t_0)\rangle$ at time t_0 we can calculate the state at $t_0 + \delta t$ using the time-dependent Schrödinger equation with the initial condition $|\psi(t_0)\rangle = |m(t_0)\rangle$. Assuming slowly varying gate voltages we may solve the equation and obtain

$$\begin{aligned}|\psi(t_0+\delta t)\rangle &= e^{-iE_m(t_0)\delta t/\hbar}|m(t_0)\rangle \\ &\quad + \sum_{l\neq m} \frac{e^{-iE_l(t_0)\delta t/\hbar} - e^{-iE_m(t_0)\delta t/\hbar}}{i(E_l(t_0) - E_m(t_0))/\hbar} \langle l(t_0)|\vec{\nabla}_{\vec{q}} m(t_0)\rangle \cdot (\partial\vec{q}/\partial t)|l(t_0)\rangle \\ &:= |m(t_0+\delta t)\rangle + |\delta m(\delta t)\rangle, \end{aligned} \tag{5.10}$$

where the term $|\vec{\nabla}_{\vec{q}} m(t_0)\rangle \cdot (\partial\vec{q}/\partial t)$ is the directional derivative of the state $|m(t_0)\rangle$ with respect to the change in gate charges $\vec{q}$. The amount of charge passed through the kth junction, δQ_k, during a short time interval δt, can now be calculated by inte-

grating the expectation value of the supercurrent operator

$$I_{\mathrm{S},k} = -\frac{eE_{\mathrm{J},k}}{\hbar}\sum_{\vec{n}}\left(-i|\vec{n}+\vec{\delta}_k\rangle\langle\vec{n}|e^{i\varphi/N} + \mathrm{H.c.}\right) \tag{5.11}$$

over time δt, which yields

$$\begin{aligned}\delta Q_k &= \int_{t_0}^{t_0+\delta t}\langle\psi(t)|I_{\mathrm{S},k}|\psi(t)\rangle dt \\ &= \delta t\langle I_{\mathrm{S},k}\rangle_{|m(t_0)\rangle} + 2\mathrm{Re}\left[\int_{t_0}^{t_0+\delta t}\langle m(t)|I_{\mathrm{S},k}|\delta m(t-t_0)\rangle dt\right] \\ &= \delta t\langle I_{\mathrm{S},k}\rangle_{|m(t_0)\rangle} - 2\hbar\sum_{l\neq m}\mathrm{Im}\left[\frac{\langle m|I_{\mathrm{S},k}|l\rangle\langle l|\delta m\rangle}{E_l-E_m}\right]\end{aligned} \tag{5.12}$$

where $|\delta m\rangle$ is the change in the instantaneous eigenstate induced by the change $\vec{q}(t_0) \rightarrow \vec{q}(t_0+\delta t)$. We have neglected the term quadratic in $|\delta m\rangle$ and oscillatory terms by assuming small variation $\delta\vec{q}$ and that $\delta t \gg \hbar/(E_l - E_m)$ holds for all l.

For a closed paths the total transferred charge must be equal for all the junctions due to the conservation of charge. Thus it is convenient to define also the (average) supercurrent operator I_{S} by

$$I_{\mathrm{S}} = \frac{1}{N}\sum_{j=1}^{N} I_{\mathrm{S},j} = \frac{(-2e)}{\hbar}\frac{\partial H}{\partial\varphi}. \tag{5.13}$$

The second equality follows from the φ-independence of H_{Ch} and the relation $\sum_k \varphi_k = \varphi$. The common expectation value of I_{S} and $I_{\mathrm{S},k}$ in a stationary state $|m\rangle$ is given by $(-2e/\hbar)\partial E_m/\partial\varphi$ where E_m is the corresponding eigenenergy. Using I_{S} we can express the total charge transferred through the array during one cycle along the closed path

$$\frac{Q}{-2e} = \frac{Q_{\mathrm{s}}}{-2e} + \frac{Q_{\mathrm{P}}}{-2e} = \frac{1}{\hbar}\int_0^\tau \frac{\partial E_m(t)}{\partial\phi}dt - \frac{2\hbar}{-2e}\oint\sum_{l\neq m}\mathrm{Im}\left[\frac{\langle m|I_{\mathrm{S}}|l\rangle\langle l|dm\rangle}{E_l-E_m}\right], \tag{5.14}$$

where τ is the duration of the cycle.

The obtained adiabatic evolution of the eigenstates splits the transferred charge into two parts: the pumped charge Q_{P} and the charge Q_{S} carried by the constantly flowing supercurrent I_{S}. The latter one of these can be calculated as the φ-derivative of the dynamical phase $\eta_m = -\int_0^t (E_m(\tau)/\hbar)d\tau$ in the state $|m\rangle$, $Q_{\mathrm{S}}/2e = -\partial\eta_m/\partial\varphi$, while the pumped charge is related to the φ-derivative of Berry's phase [27] as will be shown later.

For the three junction pump the pumped charge along the circular path shown in Fig. 5.4(a), can be calculated analytically in the lowest order in $E_{\mathrm{J}}/E_{\mathrm{C}}$ considering

the six charge states $|00\rangle, |10\rangle, |01\rangle, |11\rangle, |1\,\text{-}1\rangle$ and $|\,\text{-}11\rangle$ using Eq. (5.14). This yields

$$\frac{Q_{\rm P}}{2e} = 1 - 6\left(\frac{1}{3\sqrt{2}\,\delta} + \frac{1}{2-3\sqrt{2}\,\delta} + \frac{1}{\frac{3}{\sqrt{5}}\,\delta} + \frac{1}{1-\frac{3}{\sqrt{5}}\,\delta}\right)\frac{E_{\rm J}}{E_{\rm C}}\,, \tag{5.15}$$

where $\delta \equiv [(q_1 - 1/3)^2 + (q_2 - 1/3)^2]^{1/2}$ is the radius of the trajectory. This result of small $E_{\rm J}/E_{\rm C}$ and the numerical calculations with several values of $E_{\rm J}/E_{\rm C}$ are shown in Fig. 5.5.

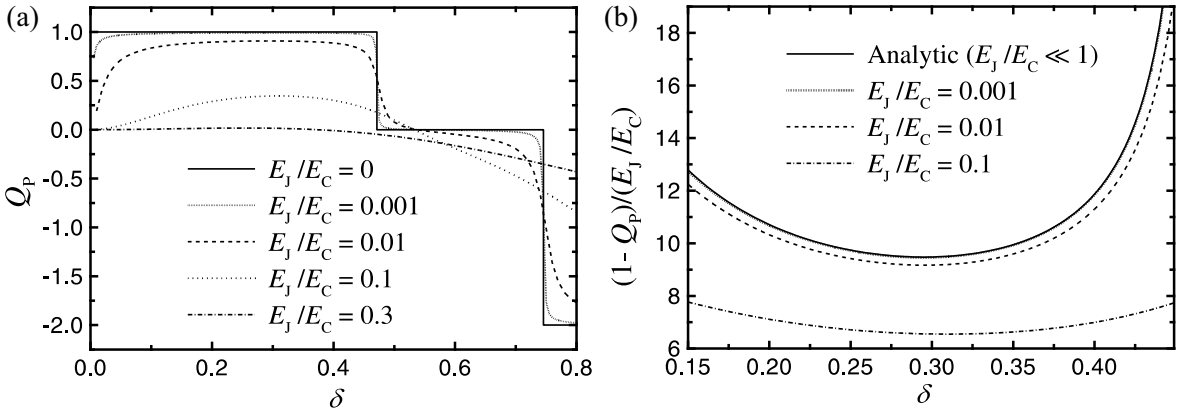

FIGURE 5.5 Numerical results of quantum inaccuracy of a uniform 3-pump for different values of $E_{\rm J}/E_{\rm C}$. The sudden drops in (a) are due to the increasing number of nodes caught inside the trajectory as it widens. The analytical result of Eq. (5.15), exact in the limit of small $E_{\rm J}/E_{\rm C}$, is shown by a solid line in (b) and it overlaps with the curve of $E_{\rm J}/E_{\rm C} = 0.001$.

In case of longer arrays the harmonic gate signals are not applicable and one has to use pulses similar to the triangular gating shown in Fig. 5.4(b). By using this gate trajectory and perturbation theory in $E_{\rm J}$ a general result for N junction pump in the limit of small $E_{\rm J}/E_{\rm C}$ can be calculated yielding

$$\frac{Q_{\rm P}}{2e} = 1 - \frac{N^{N-1}(N-1)}{(N-2)!}\left(\frac{E_{\rm J}}{8E_{\rm C}}\right)^{N-2}\cos\varphi\,. \tag{5.16}$$

The results of Eqs. (5.15) and (5.16) for $N = 3$ almost coincide for the optimum radius of $\delta \simeq 0.3$.

From the results above it is clear that the *quantum inaccuracy* in pumping is very significant: For three junction pump it is more than 20 % at $E_{\rm J}/E_{\rm C} = 0.03$, (see Eq. (5.15)) which value of $E_{\rm J}/E_{\rm C}$ is already very small. The accurate coherent pumping is thus practically impossible in the $N = 3$ pumps. Increasing the number of the junctions helps according to Eq. (5.16). It is physically clear that this conclusion should remain qualitatively valid also for non-uniform arrays, which are analysed in detail in [3]. Also the effects arising from other non-idealities are discussed in there.

5.3 Measurement of the decoherence time

Although the quantum inaccuracy in Cooper pair pumping prevents or at least limits the precise pumping of Cooper pairs, it can be used as a way to measure the decoherence time in the CPP. This is a very timely motivated topic since the obtained results should be valid also for other circuits, e.g., squbits.

Because the quantity we want to measure is the inaccuracy of the pumping, it is reasonable to use the three junction CPP, since it has the largest deviation in the pumped current. The principle of using the CPP to measure the decoherence time is simple and explained in following. To produce a measurable current one has to repeat the pumping cycle fast enough with frequency f. Ideally this yields the DC-current of $I = 2ef$, but as explained the pumped charge per cycle $Q_{\rm P} < 2e$ and thus the current does not yield the accurate result. From Eq. (5.16) we obtain for the pumped current in the three junction CPP

$$\frac{I}{2ef} \simeq 1 - 9\frac{E_J}{E_C}\cos(\varphi). \tag{5.17}$$

Yet, if the gates are operated slowly enough $1/f \gg \tau_\varphi$ or the integration time of the measurement τ_m is too long, $\tau_m \gg \tau_\varphi$, the $\cos(\varphi)$ term tends to average to $\langle\cos(\varphi)\rangle \cong 0$ during one cycle or during the measurement, and the pumping becomes accurate. However, to be able to measure a current and not to destroy the coherent superposition one has to measure the expectation value of the pumped current which means averaging over a large number of pumping cycles, $\tau_m \gg 1/f$. Thus the result of Eq. (5.17) can be realised only if the following inequalities hold: $1/f \ll \tau_m < \tau_\varphi$. Another fundamental limit comes from the Landau-Zener band crossing, which sets an upper limit for the operation frequency $f_{\rm LZ}$, which is typically around 100 MHz (2.10).

Based on these limitations we expect the following dependence of the pump performance at different frequencies (Fig. 5.6). Here we have chosen the product $\tau_m f \gg 1$ to be fixed.

1. $\tau_m > \tau_\varphi$:
$I/2ef \simeq 1$ because pumping is adiabatic but the phase is undetermined during each cycle ($\langle\cos(\varphi)\rangle = 0$).

2. $\tau_\varphi^{-1} < \tau_m^{-1} \ll f \leq f_{LZ}$:
$I/2ef \simeq 1 - 9E_J/E_C\cos(\varphi)$, pumping is adiabatic and coherent. The phase φ will still drift on a time scale longer than τ_φ. (Shaded area in Fig. 5.6)

3. $f \gg \tau_m^{-1} > f_{LZ}$:
$I/2ef$ decays because the condition for no band crossing is lost and charge transport does not follow the gating sequence adiabatically.

Since τ_φ is presently expected to fall in the range $\tau_\varphi \gtrsim 0.1\ \mu$s [35,128], in a carefully designed experiment, we would have $\tau_\varphi^{-1} < 50$ MHz, yielding a clear separation of the three pumping regimes. In particular, if the decoherence time of a squbit

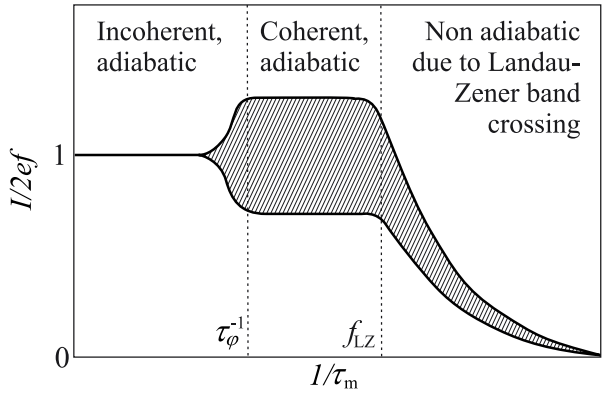

FIGURE 5.6 A schematic presentation of the expected behaviour of the pumped current in the three junction Cooper pair pump as a function of inverse of the measuring time $1/\tau_m$. The product of the pumping frequency f and the measuring time is supposed to be fixed $\tau_m f \gg 1$. The shaded area covers the different values of the phase difference φ across the array.

and thus also τ_φ turns out to be of the order of 1 μs [4], which would allow quantum computation by Josephson qubits in this respect, τ_φ^{-1} would give an experimentally convenient crossover frequency in the MHz range.

5.4 Berry's phase and its relation to pumped current

In 1984 Berry pointed out that if the system undergoes an adiabatic change, i.e., the system parameters $\vec{p} = \{p_i\}_i$ in its Hamiltonian $H(\vec{p}_i)$ are adiabatically altered, the eigenstate $|\psi\rangle$ attains a geometrical phase factor $\exp[i\gamma(\Gamma)]$, in addition to the regular dynamic phase [27]. This phase, γ, is called Berry's phase and it depends on the path Γ in the parameter space along which the system has traversed. Particularly, if the parameters are returned to their original values the eigenstate will return to its original form apart from the phase factor. This phase cannot be directly measured except via interference between another state, e.g., a similar state which has been stationary from the beginning of the process. The dynamical phase obtained along the adiabatic change depends on the path and the duration of the process whereas Berry's phase depends only on the path chosen. It has also been proposed that a squbit could be constructed using Berry's phase instead of charge or flux [52].

To derive a general formula for the Berry's phase attained during traversing the path Γ, the basis consisting of the eigenvectors $|m(\vec{p})\rangle$ with energies $E_m(\vec{p})$ is introduced so that $H(\vec{p})|m(\vec{p})\rangle = E_m(\vec{p})|m(\vec{p})\rangle$. Now we make an ansatz for the eigenstate at the time t

$$|\psi(t)\rangle = e^{i\gamma_m(t) - \frac{i}{\hbar}\int_0^t E_m(\vec{p}(t'))dt'} |m\left(\vec{p}(t)\right)\rangle \tag{5.18}$$

and insert that into the time dependent Schrödinger equation, which immediately yields

$$\frac{d\gamma_m(t)}{dt} = i\left\langle m(\vec{p}(t))\left|\frac{d}{dt}\right|m(\vec{p}(t))\right\rangle, \tag{5.19}$$

whereby

$$\begin{aligned}\gamma_m(t) &= i\int_0^t \left\langle m(\vec{p}(t'))\left|\frac{d}{dt'}\right|m(\vec{p}(t'))\right\rangle dt' \\ &= i\int_{\vec{p}(0)}^{\vec{p}(t)} \left\langle m(\vec{p})\left|\vec{\nabla}_{\vec{p}}\right|m(\vec{p})\right\rangle d\vec{p} \\ &=: i\int_{\vec{p}(0)}^{\vec{p}(t)} \langle m|dm\rangle,\end{aligned} \tag{5.20}$$

where $|dm\rangle$ is given by Eq. (5.10). This equation is naturally a general form of Berry's phase in any system with eigenvectors $|m\rangle$. The notation we use is similar to the one used in derivation of the pumped current to clarify the relation between them. In the case of the CPP $\{p_i\}_{i=1,\ldots,N} = \{q_i, \varphi\}_{i=1,\ldots,N-1}$. For a closed path $\Gamma : t \mapsto \vec{p}(t)$ with $t \in [0,\tau]$ and $\vec{p}(0) = \vec{p}(\tau)$, the last integral and thus Berry's phase seem to vanish. However, the integrand is not necessarily a total derivative, especially if the path encircles a node in the parameter space, e.g., the triple node in the stability diagram of the CPP, which yields

$$\gamma_m(\Gamma) = i\oint_\Gamma \langle m|dm\rangle \neq 0. \tag{5.21}$$

Using *Stokes theorem* and the methods of differential geometry it can be shown that Berry's phase for a closed path Γ can be calculated by integrating *Berry's curvature* over a two-surface [5, 100, 119]

$$\gamma_m(\Gamma) = i\sum_{k=1}^{N}\sum_{l=1}^{N}\iint_{S_\Gamma}\frac{\partial\langle m|}{\partial q_k}\frac{\partial|m\rangle}{\partial q_l}dq_k\wedge dq_l, \tag{5.22}$$

where the boundary of S_Γ is the path Γ. [1] To show how the pumped current in the CPP is related to Berry's phase we construct an extended path for which Berry's phase is proportional to the charge pumped along the path Γ. To do that a class of closed paths $\{\Gamma_\phi\}$ has to be defined as $\Gamma_\phi : t \mapsto \vec{p}(t) = (\vec{q}(t), \varphi(t)+\phi)$, where $t \in [0,\tau]$, so that $\Gamma_0 = \Gamma$, and also another class of paths $\{\phi_{\vec{p}}\}$ is defined according to $\phi_{\vec{p}} : t \mapsto (\vec{q}, \varphi + t\phi)$, where $t \in [0,1]$. The inverse of a path $\phi_{\vec{p}}^{-1}$ is the same path traversed in the opposite direction. The extended path

$$\Gamma_{\text{ext}}^{\phi} := \Gamma_0 \circ \phi_{\vec{p}(0)} \circ \Gamma_\phi^{-1} \circ \phi_{\vec{p}(0)}^{-1} \tag{5.23}$$

[1] It suffices to state that $dx\wedge dy = -dy\wedge dx$ is a generalisation of two-dimensional integral onto curved manifolds and that for a flat surface it reduces to the conventional $dxdy$.

is also closed and spans a two-dimensional integration surface whose width in φ-direction is ϕ as shown in Fig. 5.7(b). By traversing the boundary the contributions from $\phi_{\vec{p}(0)}$ and $\phi^{-1}_{\vec{p}(0)}$ naturally cancel, and we find

$$\gamma(\Gamma^{\phi}_{\rm ext}) = \gamma(\Gamma) - \gamma(\Gamma_{\phi}). \tag{5.24}$$

The pumped charge along the path Γ is given by Eq. (5.14) and can also be written as [13]

$$\begin{aligned}\frac{Q_{\rm P}}{-2e} &= 2\oint_{\Gamma} {\rm Re}\left[\langle m|\hat{M}|dm\rangle\right], \\ &= i\sum_{k=1}^{N}\oint_{\Gamma}\left[\frac{\partial\langle m|}{\partial\varphi}\frac{\partial|m\rangle}{\partial q_k} - \frac{\partial\langle m|}{\partial q_k}\frac{\partial|m\rangle}{\partial\varphi}\right]dq_k,\end{aligned} \tag{5.25}$$

where $\hat{M} = -i\partial/\partial\varphi$ is the operator for the average number of tunnelled Cooper pairs. This closely reminds the formulas (5.22) and (5.21) on Berry's phase.

Considering the extended path $\Gamma^{\phi}_{\rm ext}$ in the limit $\phi \to 0$, i.e., in the case of a strip of infinitesimal width $d\varphi$ between $\Gamma_{d\varphi}$ and Γ_0, one can express Berry's phase attained, $\gamma_m(\Gamma^{d\varphi}_{\rm ext})$, using Eq. (5.22). Now in Eq. (5.22) either $dq_k = d\varphi$ or $dq_l = d\varphi$ as the full length of integration. Thus $d\varphi$ can be factored out from the expression yielding the result of Eq. (5.25) multiplied by $-d\varphi$. The same result can be written using Eq. (5.24) and by taking the limit $\lim_{\phi\to 0}[\gamma(\Gamma) - \gamma(\Gamma_{\phi})]/\phi$, one obtains [5]

$$Q_{\rm P}/2e = \partial\gamma_m/\partial\varphi \tag{5.26}$$

similarly to

$$Q_{\rm S}/2e = \partial\eta_m/\partial\varphi\,. \tag{5.27}$$

Let us consider a closed path Γ corresponding to a fixed value of φ_0 as in Ref. [2]. Under ideal operation of gate and bias voltages one can change φ slightly between each cycle to evenly cover a strip in the parameter space $\{p_i\}_{i=1,\ldots,N} = \{q_i, \varphi\}_{i=1,\ldots,N-1}$ bounded by the planes $\varphi = \varphi_0$ and $\varphi = \varphi_0 + \phi$ as shown in Fig. 5.7(d). On the other hand by integrating Eq. (5.26) with respect to φ over the set $\{\Gamma_{\phi}\}$, the average pumped charge $Q_{\rm P,ave}$ can be defined as

$$Q_{\rm P,ave} = \frac{1}{\phi}\int_0^{\phi} Q_{\rm P}(\Gamma_{\varphi})d\varphi = \frac{\gamma(\Gamma_0) - \gamma(\Gamma_{\phi})}{\phi}. \tag{5.28}$$

Combining these two results one obtains an important result for an ideal CPP: the measured pumped charge per cycle (i.e. $Q_{\rm P,ave}$) yields direct information about differences of Berry's phases.

In a real experiment neither the phase difference, φ, nor the gate voltages are ideally controlled. Yet, it has to be assumed that the gate voltages are operated ac-

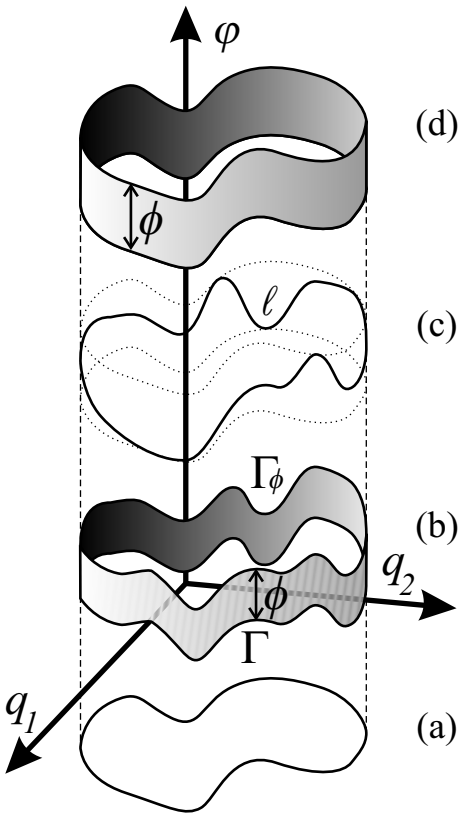

FIGURE 5.7 (a) A projection of path Γ in the (q_1, q_2)-plane. (b) A strip of finite width ϕ based on the path Γ. (c) The fluctuations of φ on a single pumping cycle, ℓ. (d) Ideal operation of gate voltages produces a strip bounded by the planes $\varphi = \varphi_0$ and $\varphi = \varphi_0 + \phi$. The same result is obtained approximately after many cycles ℓ shown in (c) with restricted, stochastic fluctuations of φ.

curately enough, so that the projections onto (q_1, q_2) plane (see Fig. 5.7(a)) nearly coincide during every cycle. Instead, the stochastic fluctuations of φ can be taken approximately into account, since they are effectively restricted to a finite range $[\varphi_1, \varphi_2] \ni \varphi_0$ during time intervals shorter than the decoherence time, τ_φ [4]. For times larger than τ_φ the fluctuations mount up too large and the phase coherence of the system is lost. If sufficiently many (identical) cycles of gate voltages are performed during this time, the fluctuations of φ yield a relatively thick mesh of trajectories within the strip. Although the 'weights' of different values of φ are uneven, the mesh can be approximated by a uniform distribution within a subset of the range $[\varphi_1, \varphi_2]$. This corresponds to a well-defined strip of the ideal case presented in Fig. 5.7(d). A cycle ℓ, with exaggerated fluctuations in φ, is shown in Fig. 5.7(c).

5.5 Turnstile kind of behaviour

As everything in the last section was derived at zero bias, in this section the effects due to non-zero bias voltage applied to the system are considered. Since the resonances of coherent tunnelling and cotunnelling separate at non-zero bias voltage V as explained in Ch. 5.1, each degeneracy node in stability diagram is split into a triangle determined by the first order tunnelling resonances, as shown by solid lines in Fig. 5.3(b) [29, 64]. Inside the triangles the state of the CPP depends on the path along which the system has reached the point, thus opening the possibility for hysteretic behavior leading to a turnstile kind of operation.

The operation of the three junction pump as a turnstile is achieved by traversing back and forth along a path in (q_1, q_2) plane with the constraint $q_1 = q_2 + k2e$, exiting the triangle at both extremes as pictured in Fig. 5.8(a). Here k is any integer number. The simplest way to describe the behaviour is to assume that at every resonance, the system is driven to the state with lower energy. This simple reasoning alone is enough to explain the turnstile kind of behaviour: within every traversal of the path one Cooper pair is transferred through the array in the direction of the bias voltage.

To explain this principle of operation in more detail one has to take into account the dissipation in the system. The adiabatic passing through the degeneracy line of charging energy H_{Ch} will induce the coherent tunnelling of a Cooper pair as explained in Ch. 2.3.1 and the limit for the adiabaticity is determined by Eq. (2.10) with $q = \sqrt{q_1^2 + q_2^2}$. In the absence of dissipation the probability for band crossing is equal in both directions, i.e., to excite or relax the system, but with dissipation the symmetry breaks. The probability to excite the system retains the same amplitude, P_{LZ}, but the probability for relaxation $P_{\mathrm{Rel}} = 1 - P_{\mathrm{LZ}} + P_{\mathrm{LZ}}^2$ is significantly increased, and reaches almost unity in the case of strong coupling to a dissipative element [10, 94]. Thus, to really obtain the hysteretic behavior one needs dissipation in the system. This can be provided, e.g., by the electromagnetic environment or quasiparticles, which both can absorb any amount of energy dissipated from the system.

The energy diagram of the CPP along the path, $[t \mapsto (q_1, q_2) : q_1(t) = q_2(t) + k2e]$ crossing the triangle as shown in Fig. 5.8(a) is plotted in Fig. 5.8(b). To be able to properly explain the behaviour we have to include in our notation the number of Cooper pairs tunnelled through the array: instead of $|n_1 n_2\rangle$ we write $|n_1 n_2, p\rangle$. If the system is initially in the state $|00, 0\rangle$ and we start to increase both gates, i.e., to move from left to right along the x-axis in Fig. 5.8(b), we come to the point of resonance for tunnelling through two junctions simultaneously, i.e., cotunnelling, to the state $|01, 0\rangle$. In the case of cotunnelling the total coupling for one Cooper pair to tunnel through two junctions, $E_{\mathrm{J}}^{\mathrm{co}}$, depends on the E_{J} of the junctions and the energy of the intermediate virtual state. This resonance condition is indicated by a dashed line in Fig. 5.8(a) and the cotunnelling is now assumed to take place. When

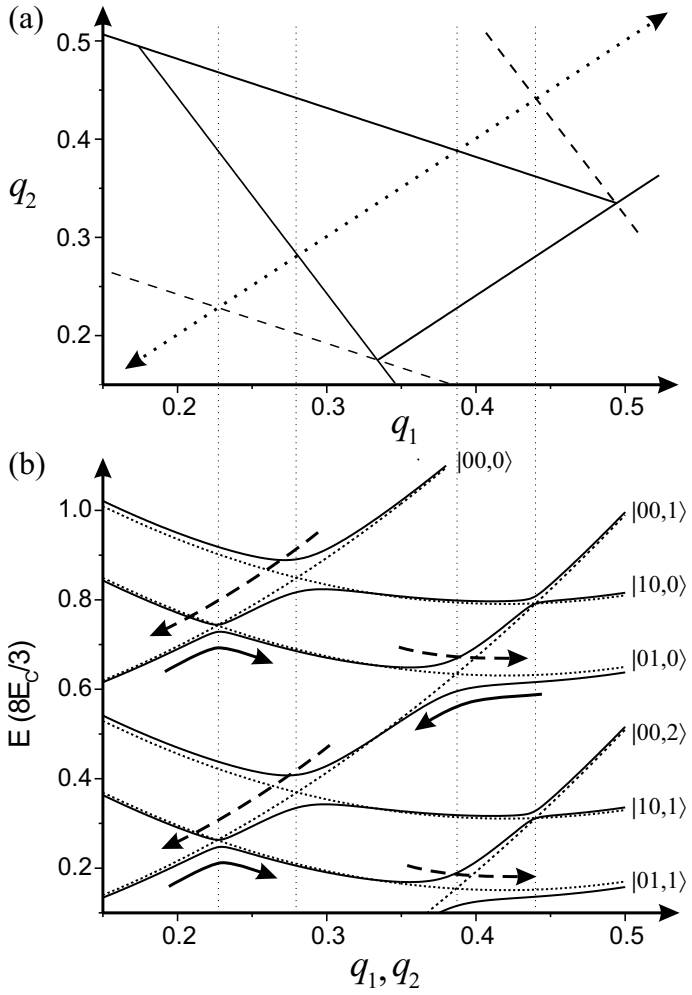

FIGURE 5.8 (a) The path $[t \mapsto (q_1, q_2) : q_1(t) = q_2(t) + k2e]$, where k is an integer, used in the turnstile measurements (dotted line). It is centered at $(1/3, 1/3)$ the degeneracy node of $V = 0$ and exits the triangle around this node at both extremes. (b) Energy diagram of the CPP plotted along the path in (a). The solid lines represent the eigenstates of the system and the dashed lines are energies of the pure charge states of H_{Ch}, which are indicated at right by kets. The arrows show the method of transferring one Cooper pair per cycle through the CPP in the direction of the bias voltage as in a turnstile. The dashed arrows correspond to the relaxation into the lower energy eigenstate at around resonances while the solid arrays indicate coherent tunnelling or cotunnelling. The thin vertical dotted lines are there to clarify corresponding locations between (a) and (b). The diagram has been calculated using parameters $E_{\mathrm{J}}/E_{\mathrm{C}} = 0.2$ and $CV/2e = 0.16$.

continuing along the path, the system is retained in state $|01,0\rangle$ due to relaxation at the resonances crossed. When coming back along the same path the system is driven to the state $|00,1\rangle$ due to a first order resonance, shown by a solid line in Fig. 5.8(a), yielding coherent tunnelling and kept there by relaxation (see Fig. 5.8(b)). Then the cycle starts over again with $|00,1\rangle$ as an initial state. Since the situation is fully asymmetric with respect to bias, the operation carries one Cooper pair per cycle through the array in the direction of the applied bias voltage V.

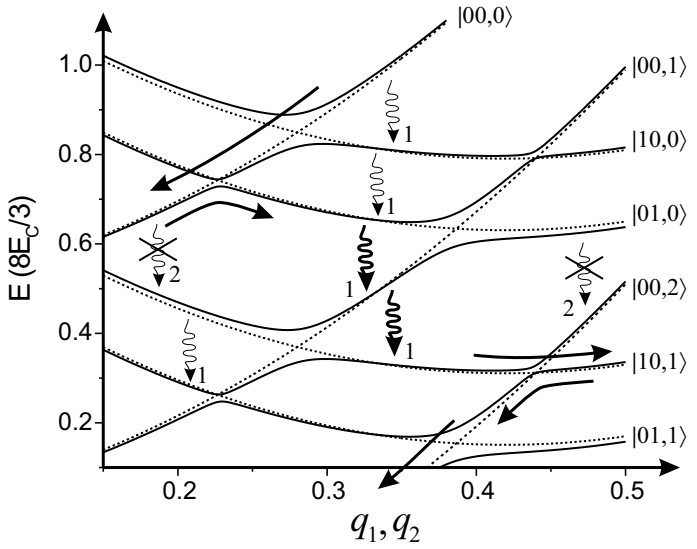

FIGURE 5.9 Evolution of the CPP along the gate path of Fig. 5.8(a). The wavy arrows numbered as 1 show a couple of examples of possible undesirable inelastic tunnellings of a Cooper pair (or of two quasiparticles), which is the most significant source of errors in the cycle of Fig. 5.8(b). However, these are not affecting the final outcome of the gate cycle unless there happens several of them during one cycle. The thick solid (straight and wavy) arrows show an example of a cycle with several inelastic tunnellings happening. The charge transferred in that particular cycle is two Cooper pairs, i.e., $4e$. Striked out wavy arrows numbered as 2 indicate similar inelastic relaxations which would instantly induce errors in pumping. These are luckily suppressed due to the large number of intermediate tunnelling events needed.

The most significant source of errors in the cycle described above is the inelastic tunnelling of Cooper pairs, which is also induced by coupling to a dissipative environment as described in Ch. 4.2.1 [77]. Examples of possible undesirable inelastic tunnelling events are shown in Fig. 5.9 by wavy arrows numbered as 1. As one can figure out from the energy diagram, these are not affecting the final outcome of the gate cycle unless there happens at least two of them during one cycle. This would induce transfer of two or more Cooper pairs during that particular cycle as in the example shown by thick solid arrows in Fig. 5.9. Also similar inelastic relaxation events which would instantly destroy the outcome of the excursion, are indicated. Fortunately though, these relaxation processes are likely to be largely suppressed due to the many virtual tunnelling events, i.e., higher order of cotunnelling, needed

in them. These processes are shown by thin wavy arrows striked out and numbered as 2. Thus, the system is fairly rigidly 'locked' to transfer only one Cooper pair per cycle.

6 Experiments with the Cooper pair pump

In this chapter experiments on a Cooper pair pump are presented. As all the measurements are explained in detail in Ref. [7], only the major results are reviewed here. The Cooper pair pump was measured to test the preceding theoretical models of the pumping and turnstile kind of behaviour. The measured sample was fabricated along the recipe presented in Ch. 2.2.1 and the experimental setup used was explained already in Ch. 2.2.2. All the measurements were carried out at the base temperature ∼20 mK. Since room temperature equipment was used in the biasing circuit, the decoherence rate obtained was supposed to be extremely fast preventing any possibility to observe coherence induced inaccuracy in the pumping. Nevertheless, even the incoherent pumping resulting in the current $I = 2ef$ has not been reliably observed in a CPP [64,135].

6.1 Sample characterisation

In Fig. 6.1 I-V characteristics of the sample, taken with different combinations of gate voltages $V_{\mathrm{g},1}$ and $V_{\mathrm{g},2}$ are presented. It shows sharp jumps at the beginning of the quasiparticle tunnelling branches at bias voltage $V \simeq \pm 6\Delta_{\mathrm{Al}}/e \approx \pm 1.2$ mV. Also all four major peaks in subgap regime corresponding to different possibilities of JQP -cycles are clearly visible [16,33,61,101]. In the large scale figure (a) the current around zero bias is not visible but it is seen in the blow up (b). The supercurrent, i.e., the feature around zero bias, is not present at $V = 0$ but it is peaked around it, having the maximum at $|V| \ll E_{\mathrm{C}}/e$ (see Fig. 6.1(b)). The shape of the supercurrent feature indicates electromagnetic environment $Z(\omega)$, with very low impedance of $0 < \mathrm{Re}[Z(\omega)] \ll R_{\mathrm{Q}}$ (see Ch. 4.2.1). This agrees well with the impedance of the biasing lines, which is of the order of the vacuum impedance $\sqrt{\mu_0/\epsilon_0} \simeq 377\ \Omega$. Resonance peaks symmetrically around zero bias at $V \approx \pm 80\ \mu$V, are also visible in this figure, and they are due to the effect of the bias voltage on the stability diagram [7]. The gate modulation is most pronounced at the gap edge as well as in the region of JQP-peaks and the supercurrent. The obtained sample parameters are presented in Table 6.1.

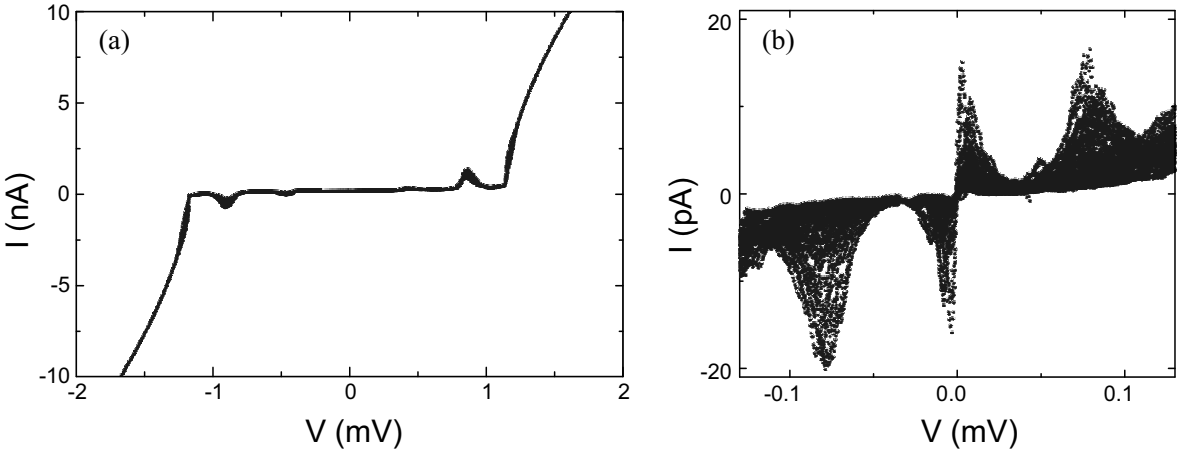

FIGURE 6.1 (a) I-V characteristics of the measured sample, taken with different combinations of gate voltages $V_{\mathrm{g},1}$ and $V_{\mathrm{g},2}$. (b) The blow up of the I-V curves near zero bias.

R_{T}	$\simeq$	34 kΩ	Normal state resistance per junction
E_{J}	$\approx$	19 μeV	Josephson coupling energy
E_{C}	$\approx$	129 μeV	Charging energy $e^2/2C$
Δ_{Al}	$\sim$	200 μeV	Energy gap
C_{T}	$\approx$	0.62 fF	Capacitance per junction
C_{g}	$\approx$	70 aF	Gate capacitances
$C_{1\leftrightarrow 2}$	$\sim$	0.16 C_{g}	Crosscoupling

TABLE 6.1 Sample parameters obtained from the measurements [7].

6.2 Gate modulation

To find the correct working point for the pumping and the turnstile operation the gate dependence of the supercurrent $I_{\mathrm{S}}(V_{\mathrm{g},1}, V_{\mathrm{g},2})$ was mapped. This was done by applying a small bias voltage to maximize I_{S} and measuring the current while passing systematically all combinations of gate voltages. Since $I_{\mathrm{S}} = -(2e/\hbar)(\partial H/\partial\varphi)$ it is clear that it should follow the honeycomb like stability diagram of the CPP (see Fig. 5.3(a)), increasing at every degeneracy line and obtaining maximum value at the triple nodes. The modulation curve obtained experimentally is presented as a contour plot in Fig. 6.2. It does not show the expected pure honeycomb like structure and its period in $C_{\mathrm{g}}V_{\mathrm{g},i}$ is e instead of $2e$. This indicates the existence of non-equilibrium quasiparticles in our system. Nevertheless, the observed pattern cannot be explained by the pure stability diagram of the quasiparticles, i.e., e-periodic honeycomb, either.

The effect of extra quasiparticles tunnelling into and out from the islands is to change the gate charge by one electron and thus to shift the $2e$-periodic stability diagram half a period (i.e., e-period) in the corresponding direction. Since the shift due to quasiparticle tunnelling is exactly half of the period of the stability diagram,

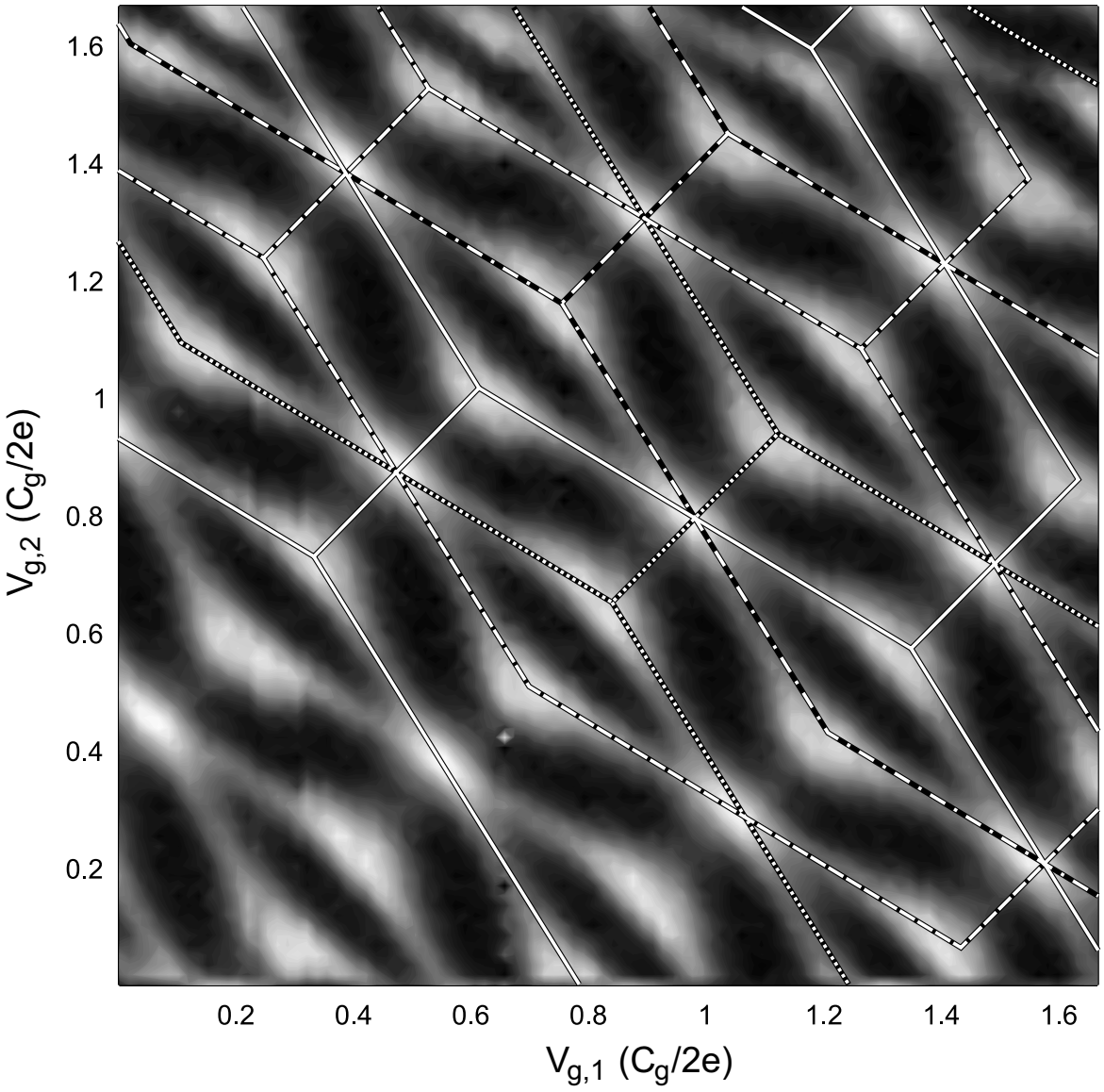

FIGURE 6.2 Supercurrent I_{S} as a function of two gate voltages $V_{\mathrm{g},1}$ and $V_{\mathrm{g},2}$. The lighter the color is, the higher is the current. The structure is composed of four different $2e$-periodic honeycombs each corresponding to the expected stability diagram of the CPP. These honeycombs are separated by half a period due to different configurations of quasiparticles, which act like discrete variations in the gate charge. Lines drawn in the figure present each one of these different honeycombs in the case of a symmetric array and they fit the data exactly, with the gate capacitances $C_{\mathrm{g},i}$ and the crosscouplings, C_{12} and C_{21}, as fitting parameters. A small bias voltage of $V \sim 15$ μV was applied during the measurement to sit approximately at the maximum of the supercurrent.

two shifts in one direction restores the original honeycomb pattern. This feature can be seen in the charging Hamiltonian, $H_{\rm Ch}$, i.e., tunnelling of two quasiparticles through the same junction has the same effect on the charging energy as the tunnelling of a Cooper pair. Thus, any quasiparticle configuration $(n_{\rm qp,1}, n_{\rm qp,2})$ can be reduced to $\{\tilde{n}_{{\rm qp},i} = n_{{\rm qp},i} \mod 2\}_{i=1,2}$ and it is enough to consider only four different honeycombs corresponding to, e.g., quasiparticle distributions $(0,0)$, $(1,0)$, $(0,1)$ and $(1,1)$.

Resulting current modulation in (q_1, q_2) plane when quasiparticles are taken into account, can be constructed by using the fully stochastic model for quasiparticles where quasiparticle tunnelling is assumed to happen randomly in both time and direction with certain average time constant. This is the usual assumption in mesoscopic superconducting devices consisting of Josephson junctions [124]. If the rate of these tunnelling events is higher than inverse of the measuring time τ_m (≥ 100 μs in our case), the current obtained is an average over the four $2e$-periodic honeycombs corresponding to the basic distributions of quasiparticles, and separated by half a period from each other as explained above.

The measured pattern of Fig. 6.2 indeed composes of four shifted $2e$-periodic honeycombs each corresponding to the stability diagram of the CPP in the absence of quasiparticles. These four honeycombs separated by half of the $2e$-period are illustrated as lines. The lines are fitted to the data with the gate capacitances and crosscouplings as fitting parameters and they correspond to the symmetric array.

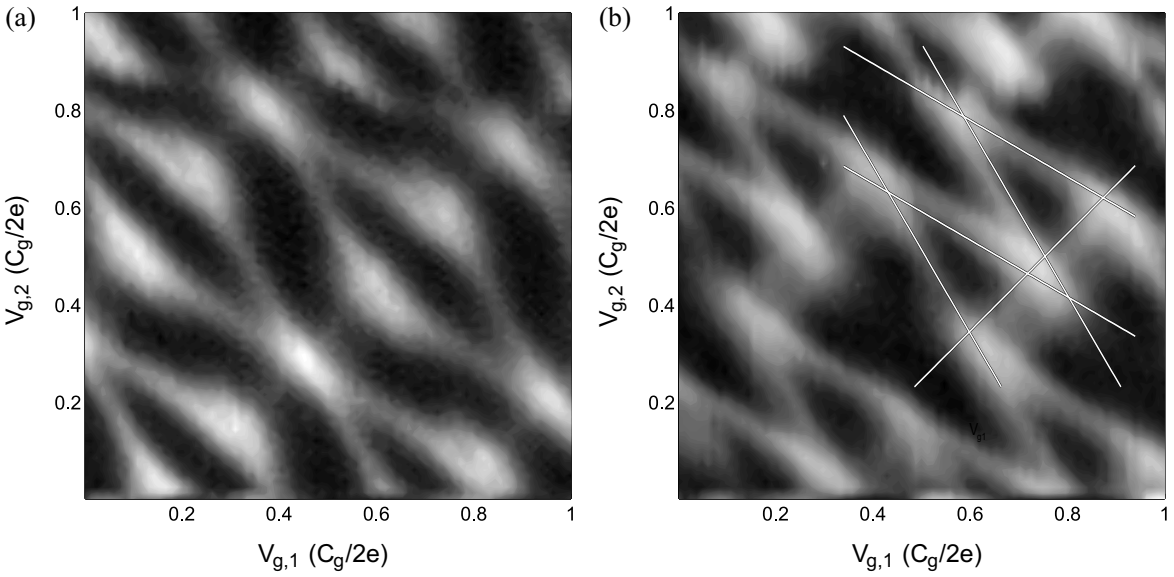

FIGURE 6.3 Supercurrent $I_{\rm S}$ as a function of two gate voltages $V_{{\rm g},1}$ and $V_{{\rm g},2}$ with two different bias voltages applied: (a) $V \simeq 0$ (Adjusted to the maximum of the supercurrent) and (b) $V \simeq 64$ μV. The lighter the color is, the higher is the current. In (b) the theoretically calculated resonance conditions for coherent tunnelling of Cooper pairs are presented as lines. These lines coincide with the pattern of enhanced current in the experimental data.

As explained in Ch. 5.1 applying the bias voltage V changes the stability diagram so that each degeneracy node is split into a triangle as shown in Fig. 5.3(b). These triangles are clearly visible at the modulation plane measured at $V = 64$ μV and shown in Fig. 6.3(b). Also theoretically calculated degeneracy lines giving the first order resonance condition for Cooper pair tunnelling, are drawn in the figure. These lines are calculated using the parameters in Table 6.1. Figure 6.3(a) shows the same modulation plane but at $V = 0$. It is clearly visible that the triangles are formed around the nodes of the structure presented in Figs. 6.3(a) and 5.3(a).

Good agreement between theoretical resonance lines and the experimental data and also the reduction of the current inside the triangles proves the measured current to be mainly carried by the supercurrent, I_{S}. Thus, quasiparticles present in the system are not acting as major carriers of current and the inelastic tunnelling of Cooper pairs (see Ch. 4.2.1), is also not important, since both these phenomena should increase the current inside the whole triangle [29]. Using parameters obtained for the sample we can calculate that the triangles around the neighbouring zero bias nodes start to overlap, forming a new triple node with as high current as the supercurrent, at $V = 83$ μV, which is exactly the voltage where the highest resonance peaks are located in the experimental I-V curve (see Fig. 6.1(b)).

6.3 In-phase experiments

6.3.1 Measurements with a small RF amplitude

To test whether the former line of reasoning for turnstile kind of behaviour holds the DC gate voltages were frozen to the values corresponding to one of the degeneracy nodes and the RF-signal with the frequency of f and the amplitude of $1/6$ times the $2e$-period was fed to the two gates in-phase, as in Fig. 5.8(a). The full I-V dependence was measured at different frequencies to find the correct bias voltage, $0 < V < 83$ μV, where the applied gate path would be optimum for turnstile kind of behavior. Some of these measured I-V curves are shown in Fig. 6.4(a).

From the I-V curves we can recognize the resonance point at $V \simeq 80$ μV and the optimum operation point is the minimum between that and zero voltage, i.e., around $V \simeq \pm 50$ μV. If we extract the current at $V = 50$ μV and plot it against f we obtain the dependence shown in Fig. 6.4(b). The dashed line shows the ideal $I = 2ef$ dependence which should be obtained if the CPP operates as a turnstile as explained in Ch. 5.5.

At low f the current increases as $I \simeq 2ef$ but starts to lack behind at around 25 MHz. This saturation effect is due to the Landau-Zener crossing (2.10) but in addition, there is also a leak current which depends linearly on f. The existence of this leak current can be physically justified as the result of the undesirable inelastic tunnelling events of Cooper pairs explained in Ch 5.5. If we assume the probability for

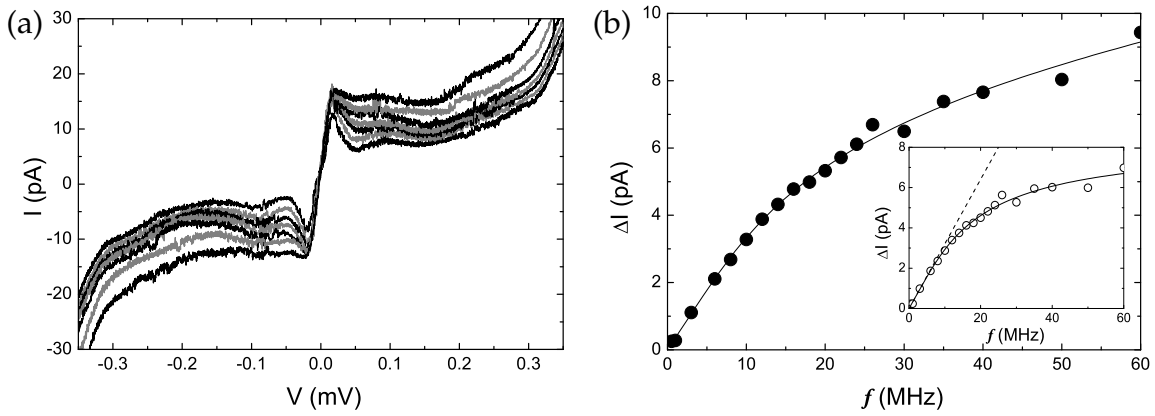

FIGURE 6.4 (a) The I-V curves measured with DC gate voltages tuned to one of the degeneracy nodes and in-phase sinusoidal RF signals added to the two gates corresponding to the path shown in Fig. 5.8(a). Amplitude used was $1/6 \times 2e$-period and frequencies corresponding to I-V curves from lowest to highest absolute current level are 0.5, 6, 12, 18, 26, 40 and 60 MHz. (b) Current $\Delta I \equiv I - I_0$ extracted from the I-V curves in (a) at $V = 50$ μV as a function of the frequency of the RF signals applied in-phase to the two gates. The solid line is the fit by Eq. (6.1) and values for the fit parameters are shown in the first line of Table 6.2 with the exception of I_0. The inset shows the same current with the leak current subtracted and the dashed line shows the ideal $2ef$ dependence predicted by the theory.

inelastic tunnelling $P_{\rm IT}$ to be independent of frequency, we obtain an approximate expression for the leak current, $I_{\rm leak} = [2eP_{\rm IT}^2 + \mathcal{O}(P_{\rm IT}^4)]f$, which depends linearly on f. The function which was used to fit the data and is shown in Fig. 6.4(b), is of the form

$$I = 2efQ_{\rm P}\left(1 - e^{-f_{\rm LZ}/f}\right) + 2efQ_{\rm L} + I_0, \tag{6.1}$$

where the fit parameters are $f_{\rm LZ}$, I_0 the offset in current, $Q_{\rm P}$ and $Q_{\rm L}$, which are the charges transferred and leaked during one cycle in units of $2e$, respectively. The analysis of the data was done both at negative and positive bias voltages. We also repeated the measurement in another node with slightly larger amplitude ($1/4 \times 2e$-period) of RF signal and these results are also shown in Table 6.2.

As seen from Table 6.2, the obtained frequency dependence agrees with the theoretical prediction of $2ef$ at low frequencies, i.e., $Q_{\rm P} \approx 1$. However, the Landau-Zener frequency obtained, $f_{\rm LZ} \sim 30$ MHz, is lower than that estimated ~ 65 MHz for cotunnelling. This discrepancy can be explained with the small inhomogeneity of the sample [6]. For the leaked charge we obtained $Q_{\rm L} \sim 0.17$, which corresponds to a 17 % probability for an extra Cooper pair to leak via inelastic tunnelling events shown in Fig. 5.9, during one cycle.

Amplitude, bias	Q_{P} (2e)	f_{LZ} (MHz)	Q_{L} (2e)
$A = 2e/6, V > 0$	0.985 ± 0.068	26.2 ± 4.4	0.127 ± 0.046
$A = 2e/6, V < 0$	0.956 ± 0.080	29.1 ± 6.5	0.142 ± 0.068
$A = 2e/4, V > 0$	0.996 ± 0.049	35.1 ± 4.4	0.132 ± 0.031
$A = 2e/4, V < 0$	0.976 ± 0.100	24.7 ± 5.0	0.229 ± 0.030
$A = 2e/3, V > 0$	4.0 ± 2.3	3.5 ± 1.8	0.546 ± 0.029
$A = 2e/3, V < 0$	3.8 ± 1.3	4.4 ± 1.4	0.481 ± 0.027

TABLE 6.2 Fit parameters using Eq. (6.1) under various experimental conditions. The current scale was shifted to set I_0 to zero.

6.3.2 Energy-minimisation model for quasiparticle tunnelling

The obtained accurate operation in the in-phase measurements is contradicting the general assumption that quasiparticles are tunnelling fully stochastically, which should prevent the correct operation of the measurement as long as quasiparticle tunnelling is happening at the rate faster than the inverse measuring time $\tau_m^{-1} \leq (100\ \mu\mathrm{s})^{-1}$, which indeed was assumed to explain the result of the DC-modulation measurement in Ch. 6.2.

However, we can also explain these four honeycombs by means of quasiparticle tunnelling and that *the system with degrees of freedom evolves via states of the lowest energy.* In case of a biased array, the system can always lower its energy by increasing the number p of Cooper pairs tunneled through it in Eq. (5.8). Thus, it will try to maximize the current. If we consider the system as a whole including quasiparticles and assume them to have freedom to move, they will organize themselves to the configuration providing the highest Cooper pair current. This means that the quasiparticles do not carry the current themselves, which can be the case due to Coulomb blockade and the energy gap Δ. The tunnelling of quasiparticles can be justified by the same means as in the fully stochastic model [124] except now the direction of the tunnelling events is not stochastic. According to this *energy-minimisation model*, the system always changes the quasiparticle configuration to the one corresponding to the maximum of the supercurrent, while varying the voltages $V_{\mathrm{g},i}$ in the measurement of the gate modulation thus yielding the same combination of four honeycombs for the measured current, as we would obtain if the quasiparticles tunnel fully stochastically.

In addition, the relatively accurate behaviour in the in-phase measurements agrees with the energy-minimisation model: as long as the amplitude of the RF-signal is small enough that the system stays near one degeneracy node and thus at the largest possible current given by the different choices of quasiparticle configurations, as is the case in the previous measurements, no quasiparticle tunnelling happens and the system is locked to a certain configuration yielding accurate operation. But, as soon as we increase the amplitude too much the quasiparticle configuration starts to change and thus prevents accurate pumping.

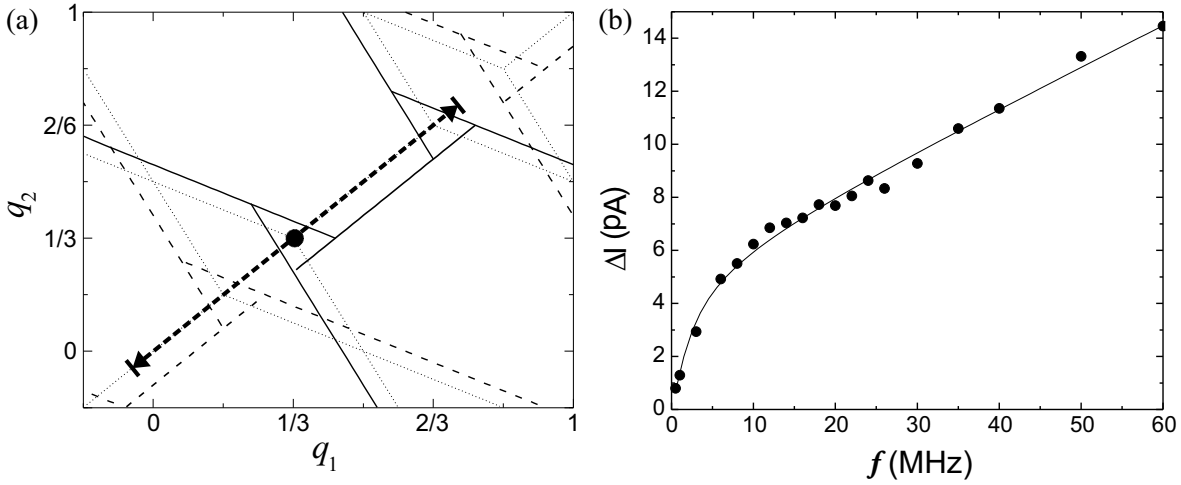

FIGURE 6.5 (a) Trajectory of the gates, shown by the thick dashed arrow, in the in-phase measurement using the largest amplitude $\sim 1/3 \times 2e$-period. Thin dotted lines show the two honeycomb patterns at $V = 0$ corresponding to quasiparticle configurations $(0, 0)$ and $(1, 1)$. Black circle is the operating point tuned by DC gate voltages. Solid and dashed lines show the $2e$-periodic stability diagrams at $V = 50$ μV corresponding to quasiparticle configurations $(0, 0)$ and $(1, 1)$. (b) Current at the degeneracy node as a function of the frequency of the applied in-phase RF signal of $\sim 1/3 \times 2e$-period amplitude. The data is taken at the optimum bias voltage $V \approx -50$ μV and the solid line is the fit by Eq. (6.1) with parameters shown on the last row of Table 6.2.

To further test this model the in-phase measurement was carried out using two times larger amplitude ($\sim 1/3 \times 2e$-period) of the in-phase RF signal corresponding to the trajectory shown in Fig. 6.5(a). The results obtained at $V = -50$ μV are shown in the last two lines of Table 6.2 and plotted in Fig. 6.5(b) with a fit by Eq. (6.1). In the absence of quasiparticle tunnelling and thus with a stable $2e$-periodic stability diagram, one would expect a twice larger $Q_{\rm P}$ ($Q_{\rm P} = 2$) than in the data presented, e.g., in Fig. 6.4(b), since the trajectory of gates crosses two triangles during one cycle. As expected, the measurements did not yield such a slope, but $Q_{\rm P} \approx 4$ instead, which can be explained with the energy-minimisation model. As seen in Fig. 6.5(b) the trajectory already moves over the neighbouring triangle corresponding to a different quasiparticle configuration. Thus the configuration is changed from (0,0) to (1,1) and back during every cycle. These extra quasiparticles responsible for changing the configuration are naturally always driven in the direction of the bias voltage thus yielding extra charge of $2e$ carried during every cycle. If one takes into account these two quasiparticles transferred and the three triangles crossed during the cycle, one corresponding to quasiparticle configuration (1,1) and two to (0,0), as shown in Fig. 6.5(a), we obtain $8e$ for the total charge carried per cycle. This explains the peculiar result of effectively four Cooper pairs transferred per cycle in the measurement.

6.4 Out-of-phase experiments

To complement the turnstile-type of in-phase measurements described in the previous chapter, the same sample was also measured with 90 degree phase-shifted RF signals applied to the two gates providing a circular path around the chosen degeneracy node. At non-zero bias voltage one should traverse around the whole triangle to achieve proper pumping. The pumped current was measured at several different nodes and with different amplitudes of the out-of-phase RF-signals: $1/9$, $1/6$, $1/4$ and $1/3$ times the $2e$-period. In Fig. 6.6 some of the I-V curves measured using the largest of these amplitudes are shown. They exhibit clear frequency dependence which, in turn, varies with the bias voltage.

The most surprising detail in these I-V curves is that they reproduce the feature observed in the in-phase measurement, so that the pumped current is always in the direction of the bias voltage. Thus out-of-phase RF signal increases the bias driven current no matter what direction we wind around the node, i.e., the current does not make a distinction whether the phase difference is $+90^\circ$ or -90°. This behaviour could be approximately explained by the similar energy minimisation argument as was done to interpret the in-phase measurements: system will always choose the state corresponding to a lower energy when the resonance is passed adiabatically. This does not fully explain the observed magnitude of current $|I| = 2ef$ when pumping in the direction against the bias voltage [6]. But, it agrees with a strong cotunnelling in the experiment, which is due to the large ratio of $E_\mathrm{J}/E_\mathrm{C} \approx 0.15$.

Ampl. (2e)	V (μV)	Q_P(2e)	f_0 (MHz)
$1/9$	-83	0.65 ± 0.12	48 ± 16
$1/9$	83	0.99 ± 0.20	31.5 ± 7.0
$1/5$	-83	0.97 ± 0.18	26.4 ± 4.6
$1/5$	83	0.97 ± 0.34	26.2 ± 9.0
$1/4$	$250 \rightarrow 350$	1.00 ± 0.26	24.0 ± 7.0
$1/4$	$-350 \rightarrow -70$	0.886 ± 0.060	29.0 ± 2.4
$1/4$	365	1.000 ± 0.074	22.1 ± 1.6
$1/4$	-320	0.934 ± 0.086	23.1 ± 2.3
$1/4$	310	1.05 ± 0.15	22.9 ± 3.4
$1/3$	75	1.91 ± 0.10	25.1 ± 1.7
$1/3$	55	1.986 ± 0.062	28.2 ± 1.2
$1/3$	35	2.130 ± 0.060	32.4 ± 1.4
$1/3$	-75	1.529 ± 0.094	24.1 ± 1.9
$1/3$	305	1.53 ± 0.10	16.6 ± 1.1

TABLE 6.3 Results of the data fits of the out-of-phase measurements. Parameters as in Eq. (6.2).

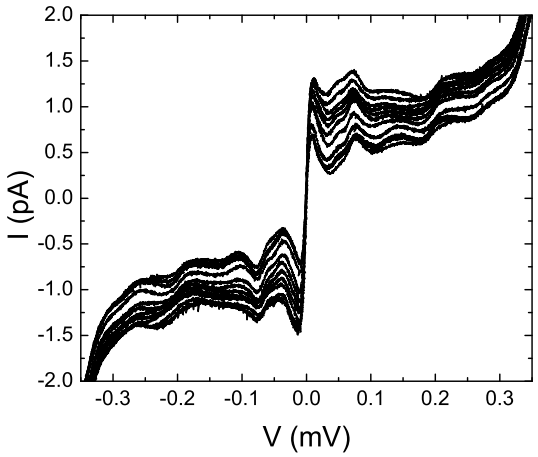

FIGURE 6.6 I-V curves measured at one of the degeneracy nodes with sinusoidal RF signal added to the two gates with 90 degree phase difference. The amplitude of the RF signal was $1/3 \times 2e$-period and the frequencies were 0.1, 0.5, 1, 3, 6, 8, 10, 12, 14, 18, and 22 MHz from the smallest to the highest absolute level of the current.

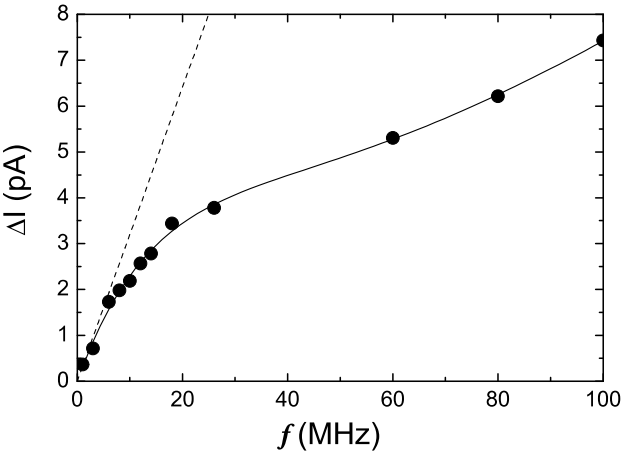

FIGURE 6.7 Current as a function of the pumping frequency. The radius of the circular trajectory of gates was $1/4 \times 2e$-period. The data have been taken at $V = 365\ \mu$V and the dashed line corresponds to $\Delta I = 2ef$. Solid lines are fits by Eq. (6.2), with parameters given in Table 6.3.

As in the in-phase measurements the current was examined at fixed voltages against the frequency. One example of these plots is shown in Fig. 6.7. The general behaviour of the current is somewhat similar to that observed in the in-phase measurements. The current increases first approximately linearly but the slope decreases at around 30 MHz. After that the out-of-phase results differ from the in-phase ones, since now the behaviour has no general tendency. The only common feature is that the slope tends to increase again. That is why the fitting of the formula similar to Eq. (6.1) does not give a satisfactory result. To find the initial slope and an approximate value of the critical frequency $f_0 \sim f_{\rm LZ}$ for LZ-crossover, we used an empirical function

$$I(f) \equiv 2efQ_{\rm P} - 2eQ_2\left(1 - e^{-f/f_0}\right) f + I_0, \tag{6.2}$$

which represents an exponential crossover from the initial slope $2eQ_{\rm P}$ to another, $2e(Q_{\rm P} - Q_2)$, with the transit frequency f_0. Obtained slopes and critical frequencies from the fits using Eq. (6.2) are shown in Table 6.3.

6.5 Parity effect revisited

The failure to observe pure $2e$-periodicity in the DC modulation in Al/Nb/Al SSET (see Ch. 3) and in the three junction CPP measurement indicates an active presence of non-equilibrium quasiparticles in the system, as in many other earlier experi-

ments [62, 64, 90, 135]. In the case of Al/Al/Al SSET and the CPB the quasiparticle traps included in the biasing lines improved the situation and pure $2e$-periodicity was observed in many samples (see Ch. 2.3.1). Nevertheless, these traps had no effect in the measurements of the CPP, which could be the case due to the extra middle junction not connected to any trap directly. Pure $2e$-periodicity has been observed in the similar structure, but with the middle junction much more transparent compared to outer ones, thus turning the configuration towards the SSET [28].

In the experiments with Al/Nb/Al SSET the quasiparticle traps were not included since all the extra fabrication steps were removed not to intrude the sensitive fabrication process of niobium, and since the layout of the device clearly fulfilled the demand for the robust $2e$-periodicity stated in [11]. Obviously these requirements were not enough and it is not clear that the use of Nb would improve the parity effect in any device. The reason for the lack of the parity effect in Nb based structures could be the subgap quasiparticle states, which are, e.g., due to depairing effect or the granularity of the Nb-film inducing variations in Δ_{Nb}.

If one assumes that there is always some extra undesirable subgap quasiparticle states in the samples, then the tunnelling rate of the quasiparticles, Γ would be essentially determined by the charging energy and the general golden rule expression in the limit $E_{\mathrm{C}} \gg k_{\mathrm{B}}T$: $\Gamma \approx E_{\mathrm{C}}/(e^2 R_{\mathrm{T}}^*)\exp(-E_{\mathrm{C}}/k_{\mathrm{B}}T)$, where $R_{\mathrm{T}}^* = R_{\mathrm{T}}/\eta^2$ and $\eta \simeq 10^{-4}$ is the relative density of quasiparticle states inside the gap [47, 110]. With parameters corresponding to the sample used in the measurement of the CPP and with temperature of 30 mK, this yields $\sim 10^{55}$ hours for the average time between the quasiparticle tunnelling, which is infinite in the time scale of the measurements. Yet, this time depends strongly on the temperature and if the electronic temperature of the sample would be higher, e.g., 300 mK, which could be the case due to inadequate filtering or thermalisation of the measurement lines, the time between the quasiparticle tunnelling events would be $\sim$500 ms resulting in e-periodicity in the measurement. This argument yields the same threshold temperature of $\sim$250 mK for $2e$-periodicity as the earlier measurements in [80], [89] and [126], and could explain why the $2e$-periodicity is sometimes seen and sometimes not, even if the sample parameters would suggest clear parity effect.

7 Conclusion

In this thesis a quantitative theory of adiabatic Cooper pair transport in one-dimensional arrays of Josephson junctions in an environment with vanishing impedance, has been developed. The theory predicts, among other things, that the quantum inaccuracy of the Cooper pair pumping in arrays with a small number of junctions is very large. The effects due to inhomogeneous arrays or nonideal gating sequences are also quantitatively treated. The theoretical predictions have been verified by numerical calculations, but whether the model is realistic enough to give quantitatively, or at least qualitatively, correct results will be ultimately tested in experiments.

A method to quantitatively estimate the decoherence time, τ_φ, due to dissipative electromagnetic environment in circuits consisting of small Josephson junctions has been presented. This method allows discussion about the suitability of the system in consideration as a quantum bit. Also a direct measurement of τ_φ as a crossover between coherent and incoherent pumping in the single Cooper pair pump is suggested. It is also shown explicitly how the pumped charge in the Cooper pair pump can be understood as a partial derivative of Berry's phase with respect to the phase difference φ across the array. This makes it possible to obtain information about Berry's phase by measuring the pumped current in the CPP.

The experiments with Nb/AlOx/Al SSETs show that Nb based junctions with high critical temperature ($T_\mathrm{c} \approx 8.5$ K) and Josephson coupling, can be fabricated using the regular self-alignment technique. The measured Al/Nb/Al SSETs show the clear signature of the resonant tunnelling of Cooper pairs combined with the elastic cotunnelling of quasiparticles, q-MQT, through the barrier of Δ_Nb. Also a qualitative explanation is given for the smeared I-V characteristics of the Nb junctions.

In experiments with Cooper pair pump the current in both the in-phase and out-of-phase gate cycles follows the relation $\Delta I = 2ef$ in data measured with amplitudes crossing only one triangle on the gate plane. No effect due to coherence induced inaccuracy could be determined due to the fast decoherence induced by room temperature equipment in the biasing circuit. These experiments demonstrate, however, in practise how a Cooper pair pump could be used as a turnstile with help of dissipation. A model was developed to explain the process and experiments clearly demonstrated this behaviour also quantitatively.

The accuracy of the turnstile-kind of behaviour in the in-phase measurement of the CPP is contradicting the e-periodicity observed in the DC-modulation measure-

ment induced by the stochastic tunnelling of quasiparticles. To explain this twofold behavior of the system, a very general principle of a system to always strive for minimum energy was used. The model also agrees with the earlier measurements of the Cooper pair pump [64,135] and similar devices [94].

According to experiments we state that it is very unlikely for a Cooper pair pump as such to be able to provide a current standard or otherwise work with high accuracy. The strong cotunnelling and relaxation among other uncontrollable processes tend to degrade the pumping cycles. Also the use of the CPP to measure, e.g., decoherence time would need a much more controlled electromagnetic environment to be successful [4, 55]. However, there may be ways such as highly resistive environment [135] or the use of combined flux and charge control [104,112], to overcome these difficulties.

Bibliography

[1] This thesis article **A.I**.

[2] This thesis article **A.II**.

[3] This thesis article **A.III**.

[4] This thesis article **A.IV**.

[5] This thesis article **A.V**.

[6] This thesis article **A.VI**.

[7] This thesis article **A.VII**.

[8] AMBEGAOKAR, V. AND BARATOFF, A., *Tunneling Between Superconductors*. Phys. Rev. Lett. **10** (1963) 486. ; erratum, **11** (1963) 104.

[9] ANDERSSON, K., DELSING, P., AND HAVILAND, D., *Synchronous Cooper pair tunneling in a 1D array of Josephson junctions*. Phys. B **248-288** (2000) 1816.

[10] AO, P. AND RAMMER, J., *Quantum Dynamics of a two-state system in a dissipative environment*. Phys. Rev. B **43** (1991) 5397.

[11] AUMENTADO, J., KELLER, M. W., AND MARTINIS, J. M., *Requirements for robust 2e periodicity in single-Cooper-pair transistors* (2002). Submitted to J. Phys. Soc. Jpn. (cond-mat/0308253).

[12] AUNOLA, M., *Analysis of the tunnelling-charging Hamiltonian of a Cooper pair pump*, Ph.D. thesis, Department of Physics, University of Jyväskylä (2001).

[13] AUNOLA, M., *Tunneling-charging Hamiltonian of a Cooper-pair pump*. Phys. Rev. B **63** (2001) 132508.

[14] AVERIN, D. V., *Adiabatic quantum computation with Cooper pairs*. Solid State Commun. **105** (1998) 659.

[15] AVERIN, D. V., *Continuous weak measurement of the macroscopic quantum coherent oscillations*, in *Exploring the quantum-classical frontier*, edited by J. R. Friedman and S. Han (Nova science publishers, Commack, NY, 2000). Cond-mat/0004364.

[16] AVERIN, D. V. AND ALESHKIN, V. YA., Pis'ma Zh. Éksp. Teor. Fiz. **50** (1989) 331. [JETP Lett. **50**, 367 (1989)].

[17] AVERIN, D. V. AND LIKHAREV, K. K., *Modern problems in condensed matter sciences*, in *Mesoscopic phenomena in solids*, edited by B. L. Altschuler, P. A. Lee, and R. A. Webb (North-Holland, Amsterdam, 1991), p. 213.

[18] AVERIN, D. V. AND ODINTSOV, A. A., *Macroscopic quantum tunneling of the electric charge in small tunnel junctions*. Phys. Lett. A **140** (1989) 251.

[19] AVERIN, D. V., ODINTSOV, A. A., AND VYSHENSKII, S. V., *Ultimate accuracy of single-electron dc current standards*. J. Appl. Phys. **73** (1993) 1297.

[20] AVERIN, D. V. AND NAZAROV, YU. V., *Virtual electron diffusion during quantum tunneling of the electric charge*. Phys. Rev. Lett. **65** (1990) 2446.

[21] AVERIN, D. V. AND NAZAROV, YU. V., *Macroscopic Quantum Tunneling of Charge and Co-Tunneling*, in *Single charge tunnelling, Coulomb blockade phenomena in nanostructures*, edited by H. Grabert and M. H. Devoret (Plenum, New York, 1992), p. 217.

[22] AVERIN, D. V. AND NAZAROV, YU. V., *Single-Electron Charging of a superconducting Island*. Phys. Rev. Lett. **69** (1992) 1993.

[23] BARDEEN, J., COOPER, L. N., AND SCHRIEFFER, J. R., *Theory of Superconductivity*. Phys. Rev. **108** (1957) 1175.

[24] BENNETT, C. H., BRASSARD, G., CRÉPEAU, C., JOZSA, R., PERES, A., AND WOOTTERS, W. K., *Teleporting an unknown quantum state via dual classical and Einstein-Podolsky-Rosen channels*. Phys. Rev. Lett. **70** (1993) 1895.

[25] BENNETT, C. H. AND DIVINCENZO, D. P., *Towards an engineering era?* Nature **377** (1995) 389.

[26] BENNETT, C. H. AND DIVINCENZO, D. P., *Quantum information and Computation*. Nature **404** (2000) 247.

[27] BERRY, M. V., *Quantal phase factors accompanying adiabatic changes*. Proc. R. Soc. London, Ser. A **392** (1984) 45.

[28] BIBOW, E., LAFARGE, P., AND LÉVY, L. P., *Resonant Cooper Pair Tunneling through a Double-Island Qubit*. Phys. Rev. Lett. **88** (2002) 017003.

[29] BIBOW, E. N., *Spectroscopie tunnel d'un circuit à deux îlots*, Ph.D. thesis, de l'Université Joseph Fourier - Grenoble I en Physique (2001).

[30] BOUCHIAT, V., VION, D., JOYEZ, P., ESTEVE, D., AND DEVORET, M. H., *Quantum Coherence with a Single Cooper Pair*. Physica Scripta T **76** (1998) 165.

[31] BOUCHIAT, V., VION, D., JOYEZ, P., ESTEVE, D., AND DEVORET, M. H., *Quantum Coherence of Charge States in the Single Electron Box*. J. Supercond. **12** (1999) 789.

[32] BRATUS, E. N., SHUMEIKO, V. S., AND WENDIN, G., *Theory of Subharmonic Gap Structure in Superconducting Mesoscopic Tunnel Contacts*. Phys. Rev. Lett. **74** (1995) 2110.

[33] VAN DEN BRINK, A. M., ODINTSOV, A. A., BOBBERT, P. A., AND SCHÖN, G., *Coherent Cooper pair tunneling in systems of Josephson junctions: effects of quasiparticle tunneling and of the electromagnetic environment*. Z. Phys. B **85** (1991) 459.

[34] CALDEIRA, A. O. AND LEGGETT, A. J., *Quantum tunnelling in a dissipative system*. Ann. Phys. **149** (1983) 374.

[35] CHIORESCU, I., NAKAMURA, Y., HARMANS, C. J. P. M., AND MOOIJ, J. E., *Coherent Quantum Dynamics of a Superconducting Flux Qubit*. Science **299** (2003) 1869.

[36] CHOI, M. S., FAZIO, R., SIEWERT, J., AND BRUDER, C., *Coherent oscillations in a Cooper pair box*. Europhys. Lett. **53** (2001) 251.

[37] COTTET, A. Private communication.

[38] DELAHAYE, J., HASSEL, J., LINDELL, R., SILLANPÄÄ, M., PAALANEN, M., SEPPÄ, H., AND HAKONEN, P., *Low-Noise Current Amplifier Based on Mesoscopic Josephson Junction*. Science **299** (2003) 1045.

[39] DEVORET, M. H., ESTEVE, D., GRABERT, H., INGOLD, G.-L., POTHIER, H., AND URBINA, C., *Effect of the electromagnetic environment on the Coulomb blockade in ultrasmall tunnel junctions*. Phys. Rev. Lett. **64** (1990) 1824.

[40] DEVORET, M. H., ESTEVE, D., AND URBINA, C., *Single-electron Transfer in Metallic Nanostructures*. Nature **360** (1992) 547.

[41] DEVORET, M. H. AND SCHOELKOPF, R. J., *Amplifying Quantum Signals with the Single-Electron Transistor*. Nature **406** (2000) 1039.

[42] DIEKS, D., *Communication by EPR devices*. Phys. Lett. A **92** (1982) 271.

[43] DOLAN, G. J., *Offset masks for lift-off photoprocessing*. Appl. Phys. Lett. **31** (1977) 337.

[44] DOLATA, R., SCHRERER, H., ZORIN, A. B., AND NIEMEYER, J., *Single electron transistors with high-quality superconducting niobium island*. Appl. Phys. Lett. **80** (2002) 2776.

[45] DUBOS, P., CHARLAT, P., CROZES, T., PANIEZ, P., AND PANNETIER, B., *Thermostable trilayer resist for niobium lift-off*. J. Vac. Sci. Technol. B **18** (2000) 122.

[46] DYNES, R. C., *Direct Measurement of Quasiparticle-Lifetime Broadening in a Strong-Coupled Superconductor*. Phys. Rev. Lett. **41** (1978) 1509.

[47] DYNES, R. C. AND GARNO, J. P., *Tunneling Study of Superconductivity near the Metal-insulator Transition*. Phys. Rev. Lett. **53** (1984) 2437.

[48] EILES, T. M., MARTINIS, J. M., AND DEVORET, M. H., *Even-Odd Asymmetry of a Superconductor Revealed by Coulomb Blockade of Andreev Reflection*. Phys. Rev. Lett. **70** (1993) 1862.

[49] VAN ENK, S. J., CIRAC, J. I., AND ZOLLER, P., *Ideal Quantum Communication over Noisy Channels: A Quantum Optical Implementation*. Phys. Rev. Lett. **78** (1997) 4293.

[50] VAN ENK, S. J., KIMBLE, H. J., CIRAC, J. I., AND ZOLLER, P., *Quantum communication with dark photons*. Phys. Rev. A **59** (1999) 2659.

[51] ESTEVE, D., *Transferring Electrons One by One*, in *Single charge tunnelling, Coulomb blockade phenomena in nanostructures*, edited by H. Grabert and M. H. Devoret (Plenum, New York, 1992), p. 109.

[52] FALCI, G., FAZIO, R., PALMA, G. H., SIEWERT, J., AND VEDRAL, V., *Detection of geometric phases in superconducting nanocircuits*. Nature **407** (2000) 355.

[53] FARHANGFAR, SH., MANNINEN, A. J., AND PEKOLA, J. P., *Effect of the electromagnetic environment on arrays of small normal metal tunnel junctions: Numerical and experimental investigation*. Europhys. Lett. **49** (2000) 237.

[54] FARHANGFAR, SH., HIRVI, K. P., KAUPPINEN, J. P., PEKOLA, J. P., TOPPARI, J. J., AVERIN, D. V., AND KOROTKOV, A. N., *One Dimensional Arrays and Solitary Tunnel Junctions in the Weak Coulomb Blockade Regime: CBT Thermometry*. J. Low Temp. Phys. **108** (1997) 191.

[55] FAZIO, R., HEKKING, F. W. J., AND PEKOLA, J. P., *Measurement of coherent transfer in an adiabatic Cooper pair pump*. Phys. Rev. B **68** (2003) 054510.

[56] FILE, J. AND MILLS, R. G., *Observation of Persistent Current in a Superconducting Solenoid*. Phys. Rev. Lett. **10** (1963) 93.

[57] FITZGERALD, R. J., POHLEN, S. L., AND TINKHAM, M., *Observation of Andreev reflection in all-superconducting single-electron transistor*. Phys. Rev. B **57** (1998) R11073.

[58] FONSECA, L. R. C., KOROTKOV, A. N., AND LIKHAREV, K. K., *Accuracy of the single-electron pump using an optimized step-like rf drive waveform*. Appl. Phys. Lett. **69** (1996) 1858.

[59] FRIEDMAN, J. R., PATEL, V., CHEN, W., TOLPYGO, S. K., AND LUKENS, J. E., *Quantum superposition of distinct macroscopic states*. Nature **406** (2000) 43.

[60] FULTON, T. A. AND DOLAN, G. J., *Observation of single-electron charging effects in small tunnel junctions*. Phys. Rev. Lett. **59** (1987) 109.

[61] FULTON, T. A., GAMMEL, P. L., BISHOP, D. J., DUNKLEBERGER, L. N., AND DOLAN, G. J., *Observation of combined Josephson and charging effects in small tunnel junction circuits*. Phys. Rev. Lett. **63** (1989) 1307.

[62] GEERLIGS, L. J., ANDEREGG, V. F., ROMIJN, J., AND MOOIJ, J. E., *Single Cooper pair tunneling in small-capacitance junctions*. Phys. Rev. Lett. **65** (1990) 377.

[63] GEERLIGS, L. J., AVERIN, D. V., AND MOOIJ, J. E., *Observation of macroscopic quantum tunneling through the Coulomb energy barrier*. Phys. Rev. Lett. **65** (1990) 3037.

[64] GEERLIGS, L. J., VERBRUGH, S. M., HADLEY, P., MOOIJ, J. E., POTHIER, H., LAFARGE, P., URBINA, C., ESTEVE, D., AND DEVORET, M. H., *Single Cooper pair pump*. Z. Phys. B **85** (1991) 349.

[65] GINZBURG, V. L. AND LANDAU, L. D., *Teorii sverchhprovodimosti*. Zh. Eks. Teor. Fiz. **20** (1950) 1064.

[66] GLAUBER, R., in *Lectures in Theoretical Physics*, edited by A. O. Barut and W. E. Brittin (Interscience, New York, 1956).

[67] GLAZMAN, L. I. AND MATVEEV, K. A., *Residual quantum conductivity under Coulomb-blockade conditions*. Pis'ma Zh. Eksp. Teor. Phys. **51** (1990) 425. [JETP Lett. **51** (1990) 484].

[68] GOLUBEV, D. S. AND ZAIKIN, A. D., *Quantum Physics at Mesoscopic Scale* (Frontieres, 1999).

[69] GRABERT, H., INGOLD, G.-L., DEVORET, M. H., ESTEVE, D., POTHIER, H., AND URBINA, C., *Single electron tunnelin rates in multijunction circuits*. Z. Phys. B: Condens. Matter **84** (1991) 143.

[70] GROVER, L. K., *Quantum Mechanics Helps in Searching for a Needle in a Haystack*. Phys. Rev. Lett. **79** (1997) 325.

[71] HADLEY, P., DELVIGNE, E., VISSCHER, E. H., LäHTEENMäKI, S., AND MOOIJ, J. E., *3e tunneling processes in a superconducting single-electron tunneling transistor*. Phys. Rev. B **58** (1998) 15317.

[72] HARADA, Y., HAVILAND, D. B., DELSING, P., CHEN, C. D., AND CLAESSON, T., *Fabrication and measurement of a Nb based superconducting single electron transistor*. Appl. Phys. Lett. **65** (1994) 636.

[73] HAROCHE, S., BRUNE, M., AND RAIMOND, J. M., *Experiments with single atoms in a cavity: entanglement, Schrödinger's cats and decoherence*. Phil. Trans. (R. Soc. Lond.) A **355** (1997) 2367.

[74] HASSEL, J., SEPPÄ, H., AND KIVIRANTA, M., *A new way to realize a programmable Josephson voltage standard*. Phys. B **284-288** (2000) 2073.

[75] HASSELBERG, L.-E., LEVINSEN, M. T., AND SAMUELSEN, M. R., *Theories of subharmonic gap structures in superconducting junctions*. Phys. Rev. B **9** (1974) 3757.

[76] HAVILAND, D. B., HARADA, Y., DELSING, P., CHEN, C. D., AND CLAESON, T., *Observation of Resonant Tunneling of Cooper pairs*. Phys. Rev. Lett. **73** (1993) 1541.

[77] INGOLD, G.-L. AND NAZAROV, YU. V., *Charge Tunneling Rates in Ultrasmall Junctions*, in *Single charge tunnelling, Coulomb blockade phenomena in nanostructures*, edited by H. Grabert and M. H. Devoret (Plenum, New York, 1992), p. 21.

[78] JENSEN, H. D. AND MARTINIS, J. M., *Accuracy of the electron pump*. Phys. Rev. B **46** (1992) 13407.

[79] JOSEPHSON, B. D., *Possible new effects in superconductive tunnelling*. Phys. Lett. **1** (1962) 251.

[80] JOYEZ, P., LAFARGE, P., FILIPE, A., ESTEVE, D., AND DEVORET, M. H., *Observation of parity-induced suppression of Josephson tunneling in the superconducting single electron transistor*. Phys. Rev. Lett. **72** (1994) 2458.

[81] KELLER, M. W., MARTINIS, J. M., AND KAUTZ, R. L., *Rare Errors in a Well-Characterized Electron Pump: Comparison of Experiment and Theory*. Phys. Rev. Lett. (1998) 4530.

[82] KELLER, M. W., MARTINIS, J. M., ZIMMERMAN, N. N., AND STEINBACH, A. H., *Accuracy of electron counting using a 7-junction electron pump*. Appl. Phys. Lett. **69** (1996) 1804.

[83] KIM, N., HANSEN, K., TOPPARI, J. J., SUPPULA, T., AND PEKOLA, J. P., *Fabrication of mesoscopic superconducting Nb wires using conventional electron-beam lithographic techniques*. J. Vac. Sci. Technol. B **20** (2002) 386.

[84] KLEINSASSER, A. W., MILLER, R. E., MALLISON, W. H., AND ARNOLD, G. B., *Observation of Multiple Andreev Reflections in Superconducting Tunnel Junctions*. Phys. Rev. Lett. **72** (1994) 1738.

[85] KOUWENHOVEN, L. P., JOHNSON, A. T., VAN DER VAART, N. C., HARMANS, C. J. P. M., AND FOXON, C. T., *Quantized current in a quantum-dot turnstile using oscillating tunnel barriers*. Phys. Rev. Lett. **67** (1991) 1626.

[86] KUBO, R., *The fluctuation-dissipation theorem*. Rep. Prog. Phys. **29** (1966) 255.

[87] KUZMIN, L. S., DELSING, P., CLAESON, T., AND LIKHAREV, K. K., *Single-electron charging effects in one-dimensional arrays of ultrasmall tunnel junctions*. Phys. Rev. Lett. **62** (1989) 2539.

[88] LAFARGE, P., *Macroscopic Charge Quantization in Metallic Nanostructures*, Ph.D. thesis, Université Paris 6 (1993).

[89] LAFARGE, P., JOYEZ, P., ESTEVE, D., URBINA, C., AND DEVORET, M. H., *2e-Quantization of the Charge on a Superconductor*. Nature **365** (1993) 422.

[90] LAFARGE, P., POTHIER, H., WILLIAMS, E. R., ESTEVE, D., URBINA, C., AND DEVORET, M. H., *Direct observation of macroscopic charge quantization*. Z. Phys. B **85** (1991) 327.

[91] LEGGETT, A. J., *Change and Matter* (North-Holland, Amsterdam, 1987).

[92] LIKHAREV, K. K. AND ZORIN, A. B., *Theory of the Bloch-Wave Oscillations in Small Josephson Junctions*. J. Low Temp. Phys. **59** (1985) 347.

[93] LOTKHOV, S. V., BOGOSLOVSKY, S. A., ZORIN, A. B., AND NIEMEYER, J., *Cooper pair cotunneling in single charge transistors with dissipative electromagnetic environment*. Cond-mat/0305113 (unpublished).

[94] LOTKHOV, S. V., BOGOSLOVSKY, S. A., ZORIN, A. B., AND NIEMEYER, J., *Frequency-Locked Current of Cooper pairs in Superconducting Single Electron Transistor with Ohmic Resistor*, in *International Workshop on Superconducting Nano-Electronics Devices*, edited by J. P. Pekola, B. Ruggiero, and P. Silvestrini, SNED (Plenum, Naples, Italy, 2001), p. 105.

[95] MAKHLIN, Y., SCHÖN, G., AND SHNIRMAN, A., *Josehpson junction qubits with controlled couplings*. Nature **386** (1999) 305.

[96] MAKHLIN, Y., SCHÖN, G., AND SHNIRMAN, A., *Quantum-state engineering with Josephson junction devices*. Rev. Mod. Phys. **73** (2001) 357.

[97] MARTINIS, J. M., NAHUM, M., AND JENSEN, H. D., *Metrological accuracy of the electron pump*. Phys. Rev. Lett. **72** (1994) 904.

[98] MEISSNER, W. AND OCHSENFELD, R., *Ein neuer Effekt bei Eintritt der Supraleitfähigkeit*. Naturwissenschaften **21** (1933) 787.

[99] MINEEV, V. P. AND SAMOKHIN, K. V., *Introduction to Unconventional Superconductors* (Gordon and Breach, 1999).

[100] NAKAHARA, M., *Geometry, topology, and physics* (IOP Publishing, Bristol, New York, 1990), pp. 29–30, 364–372.

[101] NAKAMURA, Y., CHEN, C. D., AND TSAI, J. S., *Quantitative analysis of Josephson-quasiparticle current in superconducting single-electron transistors*. Phys. Rev. B **53** (1996) 8234.

[102] NAKAMURA, Y., PASHKIN, Y. A., AND TSAI, J. S., *Coherent control of macroscopic quantum states in a single-Cooper pair box*. Nature **398** (1999) 786.

[103] NAVEH, Y., PATEL, V., AVERIN, D. V., KIKHAREV, K. K., AND LUKENS, J. E., *Universal Distribution of Transparencies in Highly Conductive Nb/AlOx/Nb Junctions*. Phys. Rev. Lett. **85** (2000) 5404.

[104] NISKANEN, A. O., PEKOLA, J. P., AND SEPPä, H., *Fast and Accurate Single-Island Charge Pump: Implementation of a Cooper Pair Pump*. Phys. Rev. Lett. **91** (2003) 177003.

[105] ONNES, H. K., *The resistance of pure mercury at helium temperatures*. Leiden Comm. **120b** (1911).

[106] ONNES, H. K., *The disappearance of the resistivity of mercury*. Leiden Comm. **122b** (1911).

[107] ONNES, H. K., *On the sudden change in the rate at which the resistance of mercury disappears*. Leiden Comm. **124c** (1911).

[108] ORLANDO, T. P., MOOIJ, J. E., TIAN, L., VAN DER VAL, C. H., LEVITOV, L., AND LLOYD, S., *Superconducting persistent-current qubit*. Phys. Rev. B. **60** (1999) 15398.

[109] PAVOLOTSKY, A. B., WEIMANN, T., SCHERER, H., KRUPENIN, V. A., NIEMEYER, J., AND ZORIN, A. B., *Multilayer technique developed for fabricating Nb-based single-electron devices*. J. Vac. Sci. Technol. B **17** (1999) 230.

[110] PEKOLA, J. P., HEIKKILÄ, T. T., SAVIN, A. M., FLYKTMAN, J. T., GIAZOTTO, F., AND HEKKING, F. W. J., *Limitations in electron cooling* (2003). Submitted.

[111] POTHIER, H., LAFARGE, P., ORFILA, P. F., URBINA, C., ESTEVE, D., AND DEVORET, M. H., *Single electron pump fabricated with ultrasmall normal tunnel junctions*. Physica B **169** (1991) 573. [Europhys. Lett. **17**, 249 (1992)].

[112] ROMITO, A., PLASTINA, F., AND FAZIO, R., *Decoherence in a Cooper pair shuttle* (2002). Cond-mat/0212414.

[113] SCHOELKOPF, R. J., WAHLGREN, P., KOZHEVNIKOV, A. A., DELSING, P., AND PROBER, D. E., *The Radio-Frequency Single-Electron Transistor (RF-SET): A Fast and Ultrasensitive Electrometer*. Science **280** (1998) 1238.

[114] SCHRIEFFER, J. R. AND WILKINS, J. W., *Two-particle tunneling processes between superconductors*. Phys. Rev. Lett. **10** (1963) 17.

[115] SHILTON, J. M., TALYANSKII, V. I., PEPPER, M., RITCHIE, D. A., FROST, J. E. F., FORD, C. J. B., SMITH, C. G., AND JONES, G. A. C., *High-frequency single-electron transport in a quasi-one-dimensional GaAs channel induced by surface acoustic waves*. J. Phys. Cond. Matter **8** (1996) L531.

[116] SHNIRMAN, A. AND SCHÖN, G., *Quantum measurement Performed with Single-Electron Transistor*. Phys. Rev. B **57** (1998) 15400.

[117] SHNIRMAN, A., SCHÖN, G., AND HERMON, Z., *Quantum Manipulations of Small Josephson Junctions*. Phys. Rev. Lett. **79** (1997) 2371.

[118] SHOR, P. W., *Polynomial-time algorithms for prime factorization and discrete logarithms on a quantum computer*, in *Proc. of the 35th Annual Symp. on the Foundations of Computer Science* (IEEE Computer Society Press, Los Alamitos, California, 1994), p. 124. (revised version 1995a Preprint quant-ph/9508027).

[119] SIMON, B., *Holonomy, the Quantum adiabatic theorem, and Berry's phase*. Phys. Rev. Lett. **51** (1983) 2167.

[120] STEANE, A., *Quantum Computing*. Rep. Prog. Phys. **61** (1998) 117.

[121] TALYANSKII, V. I., SHILTON, J. M., PEPPER, M., SMITH, C. G., FORD, C. J. B., LINFIELD, E. H., RITCHIE, D. A., AND JONES, G. A. C., *Single-electron transport in a one-dimensional channel by high-frequency surface acoustic waves*. Phys. Rev. B **56** (1997) 15180.

[122] THOULESS, D. J., *Quantization of particle transport*. Phys. Rev. B **27** (1983) 6083.

[123] TINKHAM, M., *Introduction to superconductivity, 2nd ed.* (McGraw-Hill, New York, 1996), pp. 257–277.

[124] TINKHAM, M., HERGENROTHER, J. M., AND LU, J. G., *Temperature dependence of even-odd electron-number effects in the single-electron transistor with a superconducting island*. Phys. Rev. B **51** (1995) 12649.

[125] TOPPARI, J. J., *Sähkömagneettisen ympäristön vaikutus tunnelointiin metallisissa nanorakenteissa*, Master's thesis, Department of Physics, University of Jyväskylä (1997).

[126] TUOMINEN, M. T., HERGENROTHER, J. M., TIGHE, T. S., AND TINKHAM, M., *Experimental Evidence for Parity-Based 2e Periodicity in a Superconducting Single-Electron Transistor*. Phys. Rev. Lett. **69** (1992) 1997.

[127] TURCHETTE, Q. A., WOOD, C. S., KING, B. E., MYATT, C. J., LEIBFRIED, D., ITANO, W. M., MONROE, C., AND WINELAND, D. J., *Deterministic Entanglement of Two Trapped Ions*. Phys. Rev. Lett. **81** (1998) 3631.

[128] VION, D., AASSIME, A., COTTET, A., JOYEZ, P., POTHIER, H., URBINA, C., ESTEVE, D., AND DEVORET, M. H., *Manipulating the Quantum State of an Electrical Circuit*. Science **296** (2002) 886.

[129] VION, D., ORFILA, P. F., JOYEZ, P., ESTEVE, D., AND DEVORET, M. H., *Miniature electrical filters for single electron devices*. J. Appl. Phys. **77** (1995) 2519.

[130] VOLLHARDT, D. AND WÖLFLE, P., *The Superfluid Phases of ^3He* (Taylor and Francis, 1990).

[131] VAN DER WAL, C. H., TER HAAR, A. C. J., WILHELM, F. K., SCHOUTEN, R. N., HARMANS, C. J. P. M., AND MOOIJ, J. E., *Quantum Superposition of Macroscopic Persistent-Current States*. Science **290** (2000) 773.

[132] WOOTTERS, W. K. AND ZUREK, W. H., *A single Quantum Cannot be Clone*. Nature **299** (1982) 802.

[133] ZIMAN, J. M., *Principles of the Theory of Solids* (Cambridge University Press, Cambridge, England, 1964).

[134] ZORIN, A. B., *The Thermocoax cable as the microwave frequency filter for single electron circuits*. Rev. Sci. Instrum. **66** (1995) 4296.

[135] ZORIN, A. B., BOGOSLOVSKY, S. A., LOTKHOV, S. V., AND NIEMEYER, J., *Cooper pair tunneling in circuits with substantial dissipation: the three-junction R-pump for single Cooper pairs*, in *Macroscopic Quantum Coherence and Quantum*

Computing, edited by D. V. Averin, B. Ruggiero, and P. Silverstrini, MQC^2 Instituto Italiano per gli Studi Filosofici (Kluwer Academic / Plenum, New York, 2001), p. 147.

[136] ZUREK, W. H., *Decoherence and the transition from quantum to classical*. Physics Today **44** (1991) 36.